Fall 2016

Electrodeposition and characterization of metals and metal oxides for energy conversion and storage

Ying-Chau Liu

Department: Chemistry

ELECTRODEPOSITION AND CHARACTERIZATION OF METALS AND METAL OXIDES FOR ENERGY CONVERSION AND STORAGE

by

YING-CHAU LIU

A DISSERTATION

Presented to the Faculty of the Graduate School of the

MISSOURI UNIVERSITY OF SCIENCE AND TECHNOLOGY

In Partial Fulfillment of the Requirements for the Degree

DOCTOR OF PHILOSOPHY

in

CHEMISTRY

2016

Approved by

Jay A. Switzer, Advisor
Nicholas Leventis
Jeffrey G. Winiarz
Manashi Nath
F. Scott Miller

PUBLICATION DISSERTATION OPTION

This dissertation consists of the following three articles that are published in peer reviewed journals:

Paper I, found on pages 50-63, is published in *Chemistry of Materials* 2013, vol. 25(9), pp. 1922-1926.

Paper II, found on pages 64-84, is published in *Electrochimica Acta* 2014, vol. 140, pp. 359-365.

Paper III, found on pages 85-116, and its Supporting Information, found on pages 117-126, are published in *ACS Applied Materials & Interfaces* 2016, vol. 8(24), pp. 15828-15837.

ABSTRACT

This dissertation investigates the electrodeposition of metal and metal oxide thin films applicable to solar water splitting cells. Paper I describes the synthesis of cobalt hydroxide, β-$Co(OH)_2$, by electrochemically reducing tris(ethylenediamine)cobalt(III) in alkaline solution. Paper II presents a scheme to convert the electrodeposited β-$Co(OH)_2$ to CoOOH and Co_3O_4 and compares their catalytic activity for the oxygen evolution reaction. Co_3O_4 appears to be a more active catalyst than CoOOH based on Tafel analysis. However, when the observed current densities are corrected for the measured electrochemically active surface area, the linear region of the two Tafel plots fell on the same line—suggesting the active species, likely Co(IV), for the oxygen evolution reaction is the same on both materials. Paper III introduces the fabrication of nanometer-thick gold on silicon as an inexpensive and convenient alternative to single crystal gold substrates. In addition to protecting the Si from corrosion, the Au buffer layer forms a Schottky junction with n-Si and exhibits electronic properties useful for photoelectrochemical cells.

ACKNOWLEDGMENTS

I would like to thank my advisor Prof. Jay A. Switzer for the opportunity to work on the exciting projects and the continuous guidance throughout the research. I would also like to thank my committee members Prof. Nicholas Leventis, Prof. Jeffrey G. Winiarz, Prof. Manashi Nath, and Prof. F. Scott Miller for their insightful suggestions during the study. My lab mates Dr. Jakub A. Koza, Dr. James C. Hill, Dr. Gojun Mu, Dr. Zhen He, Dr. Sanaz Y. Parast, Niharika Burla, Naveen K. Mahenderkar, Qingzhi Chen, Caleb M. Hull and Meagan V. Kelso have all been supportive in the lab. Dr. Eric W. Bohannan offered exceptional assistance in XRD measurements. Dr. Clarissa A. Wisner and Dr. Jessica R. Terbush provided superb technical support in SEM and TEM imaging. I would like to thank my parents for financial and mental support throughout the years. Perhaps, the most crucial factor of my academic achievement and life advancement came from my lovely girlfriend Jingyi Liao. I thank all people who have helped me through my Ph.D. journey. Finally, the funding for this work has been provided by the U.S. Department of Energy, Office of Basic Science under Grant No. DE-FG02-08ER46518.

TABLE OF CONTENTS

Page

LIST OF ILLUSTRATIONS

PAPER II

PAPER III

LIST OF SCHEMES

SECTION Page

PAPER II

LIST OF TABLES

PAPER II Page

SECTION

1. INTRODUCTION

The development of a long-term, sustainable energy economy is one of the most important technical challenges facing humanity in the 21st century.[1] At the current rate of population growth, global energy consumption is projected to increase at least 2-fold by midcentury.[2] This demand could be met, in principle, from fossil energy resources. In fact, the total fossil energy reserves, including coal, oil and gas can support up to 30-TW energy consumption rate globally for at least several centuries.[2] However, consumption of fossil fuel at that rate will cause significant global issues including the emission of CO_2. There are no natural destruction mechanisms of CO_2 in the atmosphere and the equilibration between the atmospheric CO_2 and the top layer of the ocean takes ~10-30 years.[2] CO_2 emission is essentially cumulative on the century-level time scale. Reducing the CO_2 emission requires the use of renewable or carbon-neutral fuel sources. Of the various renewable energy sources, solar energy is by far the largest exploitable resource, providing more energy in 1 hour to the earth than the total energy consumed by humans in an entire year. Due to solar intermittency, if solar energy is to be the major energy source, it must be conveniently stored and dispatched on demand to the end user. One attractive approach, inspired by nature, is to store solar-converted energy in the form of chemical bonds, similar to a photosynthesis process. To form a useful fuel, O_2 must be evolved, so it can be released into the oxygen-containing atmosphere and serves as the oxidation reagent upon fuel consumption. The reduced fuel can be hydrogen from water splitting, or it could be an organic species, such as methane, methanol or other

hydrocarbons, that is derived from the fixation of atmospheric CO_2. Recombination of the released O_2 with the reduced fuel would restore the original species, thus closing the cycle in a carbon-neutral fashion.

Photoelectrochemical (PEC) cells with semiconductor photoelectrodes can directly convert sunlight into stored chemical potential.[3] In the simplest case of PEC water splitting, where solar energy is captured and stored in the bond rearrangement of water to H_2 and O_2, there must be a charge separation mechanism. A junction formed between a semiconductor and a contact layer is the key to charge separation that drives photoconversion processes. Equilibration of chemical potential at the junction creates an internal electric field (referred to as the built-in voltage) and establishes a region known as the depletion region where mobile charges are separated. Absorption of light within the depletion region results in charge separation driven by the built-in field. As a result, for n-type semiconductor electrodes, photogenerated holes transfer across the interface to participate in an oxidation reaction (at the photoanode) and electrons are transported to the counter electrode via the external circuit for the reduction reaction. However, the photogenerated electrons and holes can also recombine across the same interface, and such recombination reduces the energy conversion efficiency. Hence, the carrier dynamics and charge separation and recombination across junctions represent important factors determining the PEC performance.

A PEC device is usually composed of multiple layers and materials. An efficient photoelectrode requires optimization in several aspects, from the layer construction to the choice of materials. Section 1.1 of this dissertation introduces electrochemical methods to synthesize the materials. It covers the electrodeposition mechanisms of some metals and

more complex materials such as metal oxides and (oxy-)hydroxides. When the crystallographic orientation of the deposited material is controlled by that of the substrate, the deposited material is said to be epitaxially related to the substrate. On polycrystalline substrates, the deposited films are most likely polycrystalline as well. On single crystalline substrates, it is possible to deposit single crystalline films and the epitaxial relationship can be determined. Epitaxial films generally have lower trap densities[4] and therefore better PEC performance.

PEC devices functionalization requires coherent operation of different components. The structure and properties of the materials and their interfaces determine the device performance. Section 1.2 of this dissertation touches on the interfacial energetics with a focus on the analysis of the metal-semiconductor junction. The section also describes the effect of the surface attached catalyst for the kinetically sluggish oxygen evolution reaction (OER). The main examples used in that topic are the oxide and (oxy-)hydroxide of cobalt. Finally, the section ends with a discussion on the measurements of electrochemically active surface area, which is important in determining the activity of catalysts.

Characterization of products is essential to materials chemistry research. In Section 1.3, one of the most powerful and versatile characterization technique—X-ray diffraction (XRD)—will be introduced. XRD is most commonly used for phase identification and quantitative analysis. It is based on the unique diffraction pattern associated with each crystalline structure. XRD can also be used to probe the crystalline size and stress by evaluating the broadening and shifting of the diffracted signal (peaks). For thin film samples, XRD can be used to determine texture and thickness of the films.

1.1. ELECTRODEPOSITION

In electrochemical studies and applications, the behavior of the electrode depends largely on the properties of the electrode surface, which typically requires only a thin ($< 1\ \mu m$) film. Traditional thin film synthesis methods involves high temperature or low pressure conditions as in chemical vapor deposition (CVD),[5-7] physical vapor deposition (PVD, or sputtering),[7-9] laser ablation (or pulsed laser deposition, PLD),[10,11] molecular beam epitaxy (MBE),[12] and hydrothermal methods,[13] all of which are energy intensive processing techniques.

Electrodeposition on the other hand offers a convenient alternative at lower requirements as it can be accomplished under ambient pressure and temperature. It is a versatile technique for depositing metals,[14,15] metal alloys,[16,17] metal oxides,[18] ceramics,[19] semiconductors,[20] catalysts,[21] magnetic materials,[22] hybrid materials,[23] and biominerals.[24] By adjusting the deposition potential,[25] current density,[26] electrolyte composition,[27,28] concentration,[29] pH,[25,30,31] temperature[32] or the additives,[21] many characteristics of the film can be tuned, such as morphology,[25,33] crystallographic orientation,[30] dopant density[20] and chirality.[21] Even from the same electrolyte, different (stoichiometrical) compounds and metal alloys can be deposited at different applied potentials because the departure from the equilibrium potential can be precisely controlled.[34,35] Thus, the deposition of superlattices is possible by pulsing the potential[36] or current density[37] during the electrodeposition. Through varying the deposition time and applied current density, the film thickness and deposition rate can also be controlled. Finally, electrodeposition allows conformal films to be grown on complex shapes and areas not accessible by other line-of-sight methods.

Electrodeposition relies on the precise control of the electrode potential and/or the applied current. Therefore the disadvantage of electrodeposition includes the requirement for conductive substrates, and likewise conductive material of the deposit. If the deposited material has high resistivity, the deposition efficiency and film thickness can be adversely limited. Common substrates for electrodeposition include metals (e.g., Au, Pt, Ti, Ni, and Cu), oxides (e.g., ITO, FTO, and $SrTiO_3$), alloys (e.g., stainless steel) and other conductive substrates (e.g., glassy carbon).

Semiconductor substrates can also be used for electrodeposition, but special preparation must be exercised. Because of its tendency to form insulating native oxides on the surface, silicon wafers should be hydrogen-terminated prior to experiments.[38,39] The hydrogen-terminated silicon surface (H-Si) is prepared by a standard procedure[14] consisting of *i*) a piranha etch in 2:1 volume ratio of (98% H_2SO_4)/(30% H_2O_2) to clean off organic residues and to oxidize the Si surface, and *ii*) an ammonia fluoride etch in 40% NH_4F solution with 50 mM $(NH_4)_2SO_3$ for 20 minutes. After a quick rinse with deionized (DI) water, the H-Si is stable at ambient conditions. For Si wafers with low doping densities, an ohmic contact is needed to ensure that the metal-semiconductor contact has a negligible contact resistance relative to the bulk resistance of the semiconductor.[40] Ohmic contact is created on the back of the n-Si by Al sputtering or by applying Ga-In eutectic with a diamond scribe and heating with a soldering iron to facilitate the diffusion of Ga-In into the Si substrate. To make an electrical contact with the working electrode and to insulate the rest of the substrate from the deposition solution, a Ag wire is attached to the back of the Si by Ag paste, and the substrate is painted with nail polish or silicone leaving only the front surface exposed.

1.1.1. Electrodeposition of Metals. Electrodeposition of metals involves reduction reactions at the cathode surface where metal or metal-complex ions receive electrons from the electrode and are reduced to form the desired metal film. Scheme 1.1 shows a few examples of metal electrodeposition methods.[14,15,41] Note that the number of electrons required to reduce a metal cation is simply equal to the oxidation state of the metal. There is a rich knowledge base of electrodeposition of metals, and the industry uses several other recipes, which have been optimized for deposition efficiency or for specific appearances. The methods shown in Scheme 1.1 are not optimized for efficiency, but are more environmentally friendly and tend to yield smooth and highly oriented metal thin films.

In Scheme 1.1c, the method for Au electrodeposition onto Si substrate is adapted from Allongue and co-workers who developed the method to grow ultra-thin and ultra-smooth Au films on a specific Si substrate.[14] Note that the reaction equation is simplified from the originally proposed reaction to present only the net change in Au oxidation states. A large negative potential (beyond the thermodynamically required reduction potential of $Au^{3+} + 3e^- \rightleftharpoons Au$) is used during the deposition to *i*) prevent oxidation of Si and *ii*) promote hydrogen evolution which causes Au atom rearrangement on the Si surface to form a smooth film.[14] The substrate was pre-polarized at the said potential before submerging into the deposition solution also to prevent the SiO_2 formation on the Si surface.[14] The Si substrate is n-type with a (111) out-of-plane orientation, but the surface was miscut 0.2° precisely oriented toward $<11\bar{2}>$ to create a long-range staircase structure. This staircase structure is believed to facilitate the 2D growth of the Au film.

(a) Electrodeposition of Co:

0.1 M $CoCl_2$, -1.2 $V_{Ag/AgCl}$

$Co^{2+}(aq) + 2e^- \rightarrow Co(s)$

(b) Electrodeposition of Ni:

0.1 M $NiSO_4$ + 0.5 M $(NH_4)_2SO_4$, pH 9 with NH_4OH, -1 $V_{Ag/AgCl}$

$Ni^{2+}(aq) + 2e^- \rightarrow Ni(s)$

(c) Electrodeposition of Au:

0.1 mM $HAuCl_4$ + 0.1 M K_2SO_4 + 1 mM KCl + 1 mM H_2SO_4

-1.9 $V_{Ag/AgCl}$ prepolarized miscut n-Si(111), 200 rpm stir

$AuCl_4^-(aq) + 3e^- \rightarrow Au(s) + 4Cl^-$

Scheme 1.1. Electrodeposition of metals

Using this method, Allongue and co-workers produced nanometer-thick Au films that were atomically smooth. In Paper III, a slightly modified method was used to fabricate the Au on Si (Au/Si) samples in which -1.9 $V_{Ag/AgCl}$ was applied to the miscut n-Si(111) substrate, and 30 min deposition time was carried out under 200 rpm stirring with a magnetic stir bar. The Au on Si deposition is attractive because the inert Au layer could protect the Si substrate from corrosion during PEC studies. The Au/Si (metal-semiconductor) junction exhibits interesting interfacial energetics that are desirable in PEC applications (explained in Section 1.2.1). Moreover, the Au film grown on the miscut n-Si(111) is epitaxial, thus opening up the possibility for fabricating Au(111)

surfaces as a proxy for single crystal Au(111) substrates.[42] This Au/Si example will be used in discussions throughout the introduction section of the dissertation.

1.1.2. Electrodeposition of Metal Oxides. Although the electrodeposition of metal films is a mature field, much study has been done on the more interesting electrodeposition of metal oxides.[43,44] Unlike the electrodeposition of metals, where the cations acquire exactly the same number of electrons as their oxidation state to be reduced to neutral atoms, electrodeposition of metal oxides generally follows electrochemical-chemical (EC) mechanisms as described in the following. The first step, the electrochemical step, involves the electron transfer between the electrode and the electrochemically active species (or reactants, for simplicity) in the electrolyte, driven by the applied potential or current. The reactants can be either reduced by receiving electrons from the cathode, or they can be oxidized by losing electrons to the anode. The reactants can be the precursor of the final metal oxide of interest (or they can be other species in the electrolyte as explained in the next paragraph), in which case the metal ion or the coordination complex ion changes its oxidation state as a result of the electrochemical reduction or oxidation reaction. The intermediates then undergo chemical reactions such as hydrolysis and condensation to form the final metal oxide. Scheme 1.2 below shows the examples of cathodic electrodeposition of cobalt hydroxide, $Co(OH)_2$,[45] and anodic electrodeposition of Co_3O_4;[46] both of which involve electrochemical redox of the metal ion precursors followed by the hydrolysis of the intermediates. In Scheme 1.2(a), Co^{3+} is complexed with ethylenediamine (en) ligand and is electrochemically reduced to the Co(II)-(en) complex. $[Co(en)_3]^{2+}$ then undergoes hydrolysis to form $Co(OH)_2$. Similarly, in Scheme 1.2(b), a tartrate (tar) complex of Co^{2+} is

electrochemically oxidized to Co^{3+}, which then reacts with the unreacted Co(II)-(tar) and OH^- from the bulk electrolyte to form Co_3O_4.

(a) Cathodic electrodeposition of $Co(OH)_2$:

$$[Co(en)_3]^{3+} + e^- \rightleftharpoons [Co(en)_3]^{2+}$$

$$[Co(en)_3]^{2+} + 2OH^- \rightarrow Co(OH)_2\downarrow + 3en$$

(b) Anodic electrodeposition of Co_3O_4:

$$2Co(II)\text{-}(tar) \rightleftharpoons 2Co^{3+} + 2(tar) + 2e^-$$

$$2Co^{3+} + Co(II)\text{-}(tar) + 8OH^- \rightarrow Co_3O_4 + 4H_2O + (tar)$$

Scheme 1.2. Electrodeposition of cobalt hydroxide and oxide

The electrochemical redox reaction can also act on other solution species and cause a local pH change. Electrochemists can take advantage of this phenomenon to locally precipitate solution species that are stable under the pH of the bulk electrolyte.[47] Amphoteric metal oxides such as ZnO, Al_2O_3, SnO_2, SnO, PbO_2, PbO and Cr_2O_3 can act as acids or bases, meaning that they can dissolve in either acidic or basic solutions.[48] In Scheme 1.3 below, ZnO is used as an example to show the strategies of depositing amphoteric materials by electrochemically changing the local pH.[27,28] At 70℃, ZnO has the lowest solubility at pH ~9.4.[49] In Scheme 1.3(a), the O_2 saturated electrodeposition solution was applied a negative potential through the working electrode. The electrons

are transferred to O_2 species in the solution to form OH^- and raise the local pH.[27] Zn^{2+} is not stable at high pH, thus precipitates out as ZnO. In contrast, Scheme 1.3(b) shows the local generation of acid from the basic deposition solution. Although the pH could be lowered by oxidizing OH^- to O_2, Limmer et al. chose to reduce the local pH by oxidizing ascorbate ions because the reaction occurs at much lower potential, which minimize the oxidation of the Au substrate and promote epitaxial growth of ZnO.[28]

(a) Electrodeposition of ZnO by locally generating base:

$$O_2 + 2H_2O + e^- \rightarrow 4OH^-$$

$$Zn^{2+} + 2OH^- \rightarrow ZnO + H_2O$$

(b) Electrodeposition of ZnO by locally generating acid:

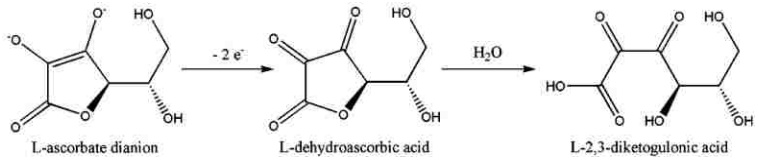

$$Zn(OH)_3^- + H^+ \rightarrow ZnO + 2H_2O$$

$$Zn(OH)_4^{2-} + 2H^+ \rightarrow ZnO + 3H_2O$$

Scheme 1.3. Electrodeposition of ZnO by increasing or decreasing the local pH

Because of multiple steps and species involved in the electrochemical-chemical reactions, mass transport has to be taken into consideration when optimizing the

deposition conditions. Since the electron transfer with the electrochemically active species only takes place at the electrode surface, the unreacted species away from the electrode will move toward the electrode through diffusion, migration and convection.[50] Diffusion is caused by a gradient in chemical potential (i.e., concentration gradient). Migration refers to the movement of charged particles due to attractive or repulsive forces within a gradient of electrical potential (i.e., electric field). Convection is the hydrodynamic fluid flow created by natural (e.g., density gradient) or forced (e.g., stirring) means. Electrochemical experiments can be designed to minimize one or more modes of mass transfer. Although diffusion cannot be eliminated from electrolysis, convection can be avoided by preventing vibration of the solution. In many electrodeposition experiments, however, convection is desired and stirring of the solution is often implemented. The effect of migration can be minimized by the addition of a supporting electrolyte. An excess of inactive supporting electrolytes is usually added to the deposition solution to ensure sufficient conductivity. This addition also reduces the resistance between the working electrode and the counter electrode to help maintain a uniform current and potential distribution across the working electrode. Furthermore, it reduces the ohmic drop between the working electrode and the reference electrode to increase the accuracy of the applied and measured potential (with respect to the reference electrode). When the concentration of the supporting electrolyte is ~100 times greater than that of the electrochemically active species, the majority of the current is carried by the supporting electrolyte. Thus, the migration rate of the active species towards the electrode of opposite charge is not dependent on the applied potential. Effective control of mass transport is important in optimizing electrodeposition conditions.

1.1.3. Epitaxial Electrodeposition. Epitaxy refers to the determination of the film's crystallographic orientation on that of the substrate. On polycrystalline substrates, the electrodeposited films exhibit randomly oriented grains. XRD 2θ analysis (explained in Section 1.3.1) of such films would show a pattern that resembles a powder sample. If the substrate is textured (e.g., Au sputtered glass), the deposited film may also be textured and would show a "ring" pattern on the X-ray pole figure (explained in Supporting Information of Paper III). Typically, single crystal substrates are used for epitaxial deposition of films. The properly treated surface of a single crystal substrate presents a highly ordered plane of atoms with a well-defined crystallographic orientation. The growth of crystalline films is controlled by thermodynamics and kinetics. It tends to minimize the lattice mismatch and maximize the binding energy between the film and the substrate. Therefore, in principle, homoepitaxy is more easily achieved than heteroepitaxy. Homoepitaxy refers to the material of the deposited film being the same as that of the substrate, for example, growing a Au film on a single crystal Au substrate. Heteroepitaxy refers to the deposited material being different from the substrate material. Recall the Au/Si sample introduced in Section 1.1.1, the Au film is heteroepitaxial to the single crystalline Si(111) substrate. The interface model in Figure 1.1 shows the relationship between the planes of surface atoms on the two materials. Looking down on the Au/Si sample in the $[\bar{1}\bar{1}\bar{1}]$ direction, at an atomic scale, one would see the Au atoms (colored gold) on top of the Si atoms (colored blue). At this viewing direction, both Au and Si crystals are oriented with [111] coming out of the plane, $[10\bar{1}]$ pointing to the top, and $[1\bar{2}1]$ pointing to the right. In the very center of the interface model, the Si atom is directly underneath the Au atom and is not visible due to its smaller size. The next Si

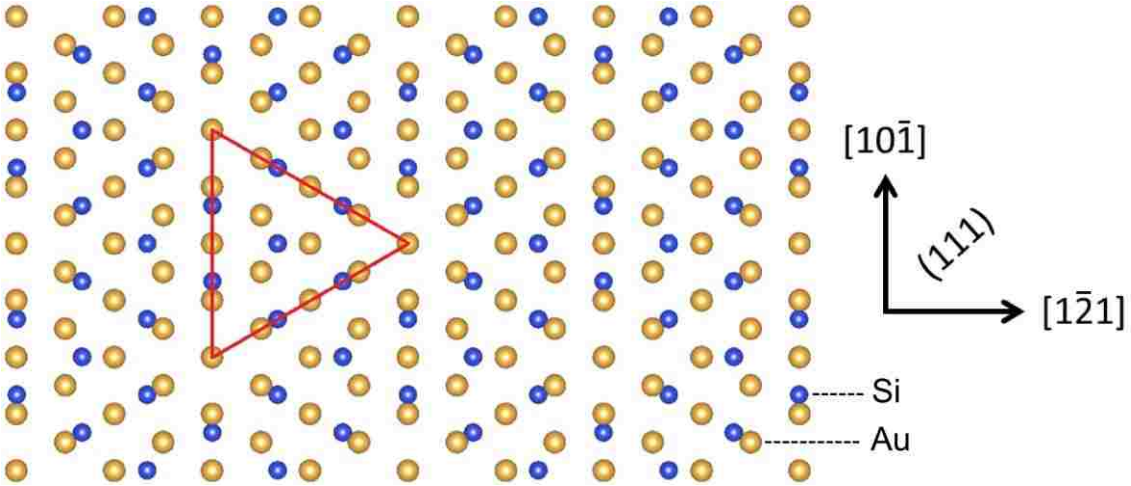

Figure 1.1. Interface model of Au(111) atoms on Si(111) surface

atom closest to the center Si atom is 3.8402 Å apart, which is the d-spacing of Si(110). On the other hand, Au(110) are separated by its d-spacing 2.8840 Å. The lattice mismatch is calculated by taking the difference between the two substances' lattice parameters and dividing by the substrate's lattice parameter, which is equivalent to using their d-spacing values, as shown below in Equation. 1.

$$\frac{a_{film} - a_{substrate}}{a_{substrate}} \times 100\% \equiv \frac{d(110)_{film} - d(110)_{substrate}}{d(110)_{substrate}} \times 100\% = \frac{2.8840\text{Å} - 3.8402\text{Å}}{3.8402\text{Å}} \times 100\% = -25\% \quad (1)$$

The −25% mismatch is too large for a simple 1×1 epitaxial system, but can otherwise be explained by the formation of coincident site lattices (CSLs). One coincident site lattice is indicated by the red triangle (in Figure 1.1) whose edges are made up of 5 Au atoms or 4 Si atoms on each side. Now, the lattice mismatch becomes the difference between the two coincidence site lattices' edge lengths divided by the

substrate coincidence site lattice edge length as shown below in Equation 2. In the Au/Si case, the Au coincidence site lattice length is 4 times the d-spacing of Au(110). The Si coincidence site lattice length is 3 times the d-spacing of Si(110). By forming coincident site lattices, the Au/Si lattice mismatch is reduced from −25% to +0.13%, thus supporting the epitaxial growth of Au.[51]

$$\frac{4 \times 2.8840\text{Å} - 3 \times 3.8402\text{Å}}{3 \times 3.8402\text{Å}} \times 100\% = +0.13\% \quad (2)$$

Epitaxial films are usually produced under ultrahigh vacuum conditions as in molecular beam epitaxy (MBE). MBE was the first demonstrated technique to produce atomic scale heterostructures.[52] In MBE, ultra-pure elements are individually heated in quasi-Knudsen effusion cells to their sublimation point, creating individual molecular beams. The individual beam paths do not cross, and therefore the species do not react with each other until they reach the substrate surface. The substrate is maintained at an elevated temperature, and the deposition rate is low, both of which are important factors for epitaxial growth of the film. In contrast to the energy intensive techniques, several epitaxial films have been produced using electrodeposition. The electrodeposition of low lattice mismatch systems such as Prussian Blue on Au(110)[53] and ZnO on Si(110)[49] has been demonstrated. Several other epitaxial metal oxides have been deposited by electrodeposition including Cu_2O,[30,31,33,54] CuO,[21] AgO,[55] Fe_3O_4,[56-58] δ-Bi_2O_3,[19,59] PbO_2,[60] Tl_2O_3,[61] SnS,[62] PbS,[63] Co_3O_4[46] and methylammonium lead iodide perovskite[4] on Cu, Au, Au/Si, Si and InP substrates. The epitaxial deposition of oxides on semiconductor substrates such as Si and InP is important because of the highly sought after applications in solar energy harvesting and nanometer-scale electronic devices.

Epitaxial films allow the study of the materials' intrinsic properties rather than their grain boundaries. Through electrodeposition techniques, epitaxial films can be tuned in many aspects including size, shape, chirality and even macro structures as in superlattices. For example, the size and shape of the epitaxial Cu_2O can be controlled by the pH and additives in the solution.[25,33] While the out-of-plane and in-plane orientations of the deposit are determined by the single crystal substrate, the shape can be modified by solution additives that selectively adsorb on specific crystal faces.[64] The dominant faces in the final film are the slowest growing faces. These advantages make electrodeposition an attractive technique in producing epitaxial films.

1.2. ENERGY CONVERSION AND STORAGE

Converting solar energy to the chemical bond in the simplest molecule—hydrogen—requires the splitting of water on the electrode surface. On a p-type semiconductor photocathode, photogenerated hole moves towards the bulk of the electrode and the photo-excited electron moves towards the surface of the electrode to reduce water to H_2. On an n-type semiconductor photoanode, photo-excited electrons move towards the bulk whereas photogenerated holes move to the surface of the electrode to oxidize water to O_2. To accomplish efficient water splitting, the photoelectrodes must meet three basic requirements. They must generate electron-hole pairs upon absorption of the solar irradiation, separate the photogenerated charge carriers, and promote the oxidation or reduction of water (e.g., through catalysts).

To date, some PEC devices have been developed to achieve overall water splitting using only solar irradiation as the energy input.[65] Although this dissertation does not

focus on solar-driven PEC water splitting cells, it introduces basic concepts and physics behind PEC devices. PEC devices are based around semiconductor photoelectrodes, which are used to absorb light, separate photogenerated charge carriers and, in some cases, perform catalysis. For example, a photoanode produces an electron-hole pair upon absorption of the solar radiation. In an alkaline solution, the holes move toward the surface of the electrode to oxidize hydroxide anions to oxygen gas whereas the electrons travel through the external circuit to the counter electrode to reduce water molecules to hydrogen gas, thus accomplishing overall water splitting. The following section explains the basic principles of semiconductor photoelectrochemical devices.

1.2.1. Semiconductor Photoelectrochemistry. A basic understanding of the device physics of semiconductors and their junctions between a metal or a solution is essential to the design and engineering of efficient solar water splitting cells. When a semiconductor is in intimate contact with a metal or a solution, the energy must reach equilibrium at the interface. The discussion here will focus on metal-semiconductor junction energetics. Solution-semiconductor interfaces, on the other hand, follow a similar fashion except that the work function of the metal is replaced by the equilibrium potential of the solution. Figure 1.2 shows the energy diagrams of an n-type silicon (n-Si) in contact with a metal before and after equilibrium. The solid horizontal line to the left of the metal-semiconductor interface represents the energy level of the metal's work function, φ_m. This is the minimum energy required for an electron to escape the metal surface into vacuum. The dashed line on the semiconductor side represents the energy level where the probability of finding an electron is exactly one half. It is referred to as the Fermi level, E_F, of the semiconductor. As depicted in Figure 1.2a, most of the

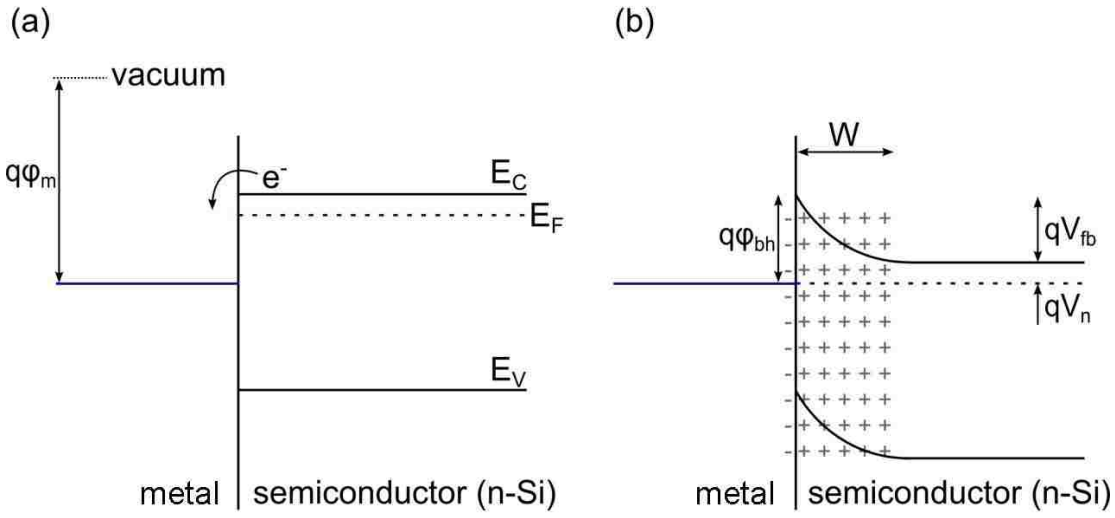

Figure 1.2. Energy diagrams of a metal in contact with n-Si (a) before equilibrium and (b) after equilibrium

electrons on the n-Si are at a higher energy level than the work function of the metal. The electrons will flow from the n-Si to the metal leaving a positively charged region (i.e., depletion width, *W*) near the surface of the n-Si, as shown in Figure 1.2b. The conduction band, E_C, and valence band, E_V, positions are both lowered in the depletion region due to the local positive charge until the semiconductor Fermi level is aligned with the metal work function. All energy terms are multiplied by *q*, the charge of an electron, because the scale commonly used to express the energy bands is the electron volt (eV).

The energy bands are bent in the depletion region of the semiconductor as a result of thermal equilibrium. This creates an energy barrier (i.e., barrier height, φ_{bh}) between the metal work function and the conduction band of the semiconductor. If a positive bias is applied to the n-Si, it will cause the bands to bend further down. Electrons do not have high enough energy to overcome the barrier height and no significant current flow should

be observed (except for small tunneling currents). If a negative bias is applied to the n-Si, the bands will rise and become flat. The voltage required for the semiconductor bands to become flat is called the flat band voltage, V_{fb}, which is also the energy difference between the initial semiconductor Fermi level and the metal work function. The electrons on the conduction band of the semiconductor can therefore flow to the metal whose work function is at a lower energy level. The work function of Au (~5.3 eV) is larger (thus at lower energy level) than the Fermi level of an n-Si (~4.3 eV). The Au/n-Si junction behaves as a Schottky diode that allows current flow in one (forward) direction and prohibits it in the other (reverse) direction with the Schottky barrier. The diode behavior can be observed in a simple solid-state current-voltage (*J*-*V*) measurement, as shown in Figure 1.3. The working electrode is connected to the n-Si through a Ag wire; whereas

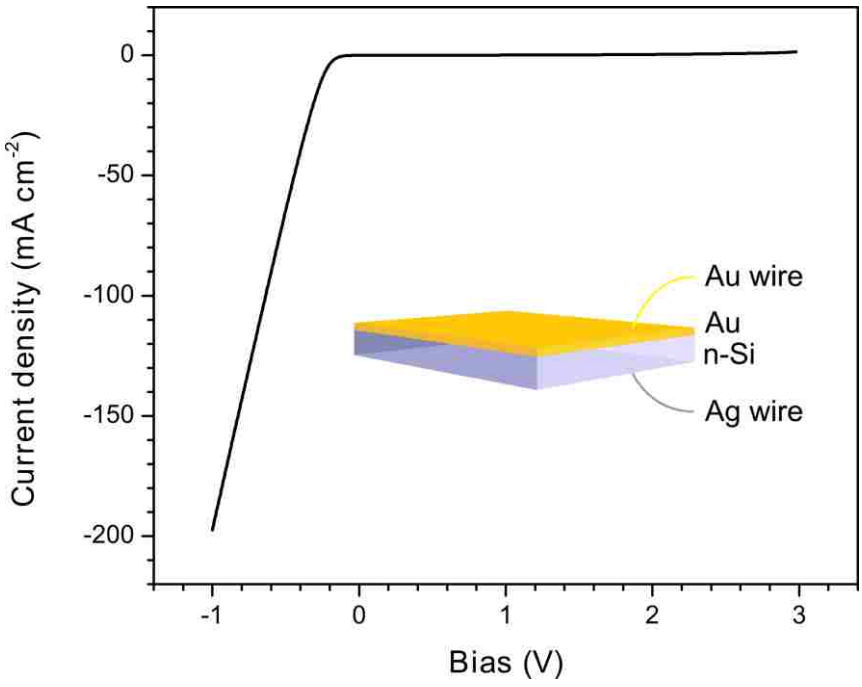

Figure 1.3. Solid-state *J*-*V* curve of Au/n-Si

the counter and reference electrodes are connected to the Au film through a Au wire. No significant current is observed when the device is positively biased, but when the potential is scanned in the negative direction, the amount of current increases sharply with the increased negative bias.

The above discussion is for a Schottky diode working in the dark. When the device is under solar illumination (often implemented through the use of a solar simulator with an AM 1.5 filter), the *J-V* curve will shift upward for the amount equal to the photocurrent at a given bias, shown as red curves in Figure 1.4. Recall the energy

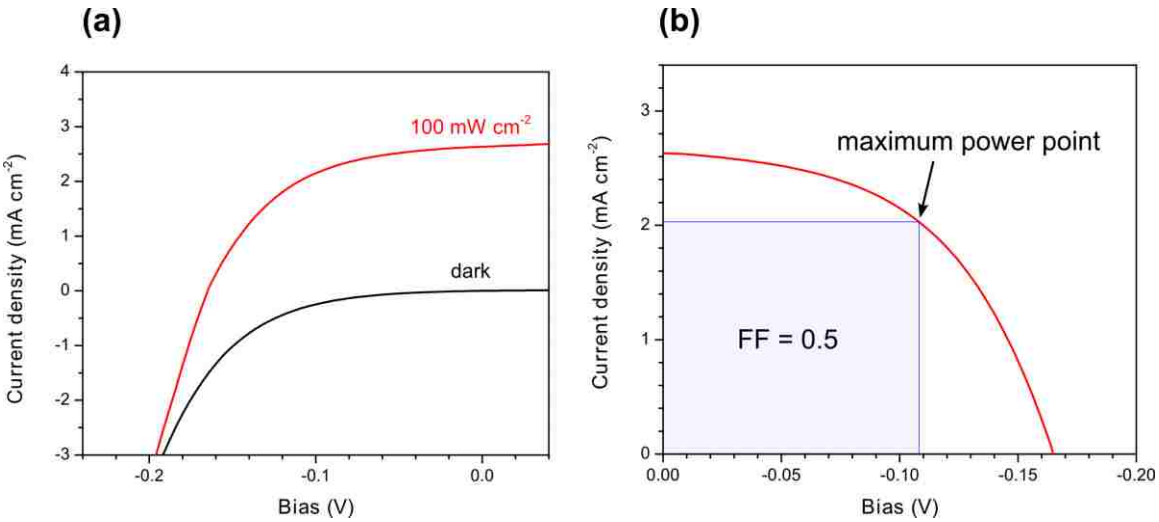

Figure 1.4. *J-V* curves of the Au/n-Si diode (a) comparing the performance in dark (black) versus under illumination (red), and (b) showing the maximum power point

diagram in Figure 1.4b, a photo-generated electron in the depletion region will be pushed towards the bulk of the semiconductor, whereas a photo-generated hole will move to the metal-semiconductor interface due to the local electric field. The result is the increased

(more positive) current at each bias compared to the current measured in dark (black curve), as shown in Figure 1.4a. The difference between the red curve and the black curve in Figure 1.4a is the photocurrent. When the device is under illumination, the measured current density at zero bias is the short circuit current density, J_{sc}, and the bias at zero current density is the open circuit voltage, V_{oc}. Within the boundary defined by J_{sc} and V_{oc}, the point with the maximum power (i.e., current × bias) is the maximum power point whose current density is J_{mpp} and voltage is V_{mpp}, as indicated by the arrow in Figure 1.4b.

If this device is to be evaluated as a solar cell, then the fill factor, *FF*, and the efficiency can be calculated using Equations 3 and 4 below:[66]

$$FF = \frac{J_{mpp} \times V_{mpp}}{J_{sc} \times V_{oc}} \tag{3}$$

$$efficiency = \frac{J_{mpp} \times V_{mpp}}{P_{in}} \tag{4}$$

where P_{in} is the power input (e.g., 100 mW cm^{-2}). For the said Au/n-Si diode, the fill factor is 0.5 and the efficiency is 0.2% (i.e., not an efficient solar cell).

The barrier height, φ_{bh}, is the energy difference between the metal work function and the semiconductor conduction band edge at the interface, which is also the energy required for electrons to flow from the metal into the semiconductor. The maximum photovoltage that can be produced by the junction is limited by the barrier height. Therefore, an accurate determination of barrier height can provide useful information for designing device interfaces. Common methods for measuring the barrier height and other energetic parameters include solid-state analysis (Figure 1.5) of current-voltage (*J*-*V*) curves (Figure 1.5a) and Mott-Schottky analysis (Figure 1.5b).

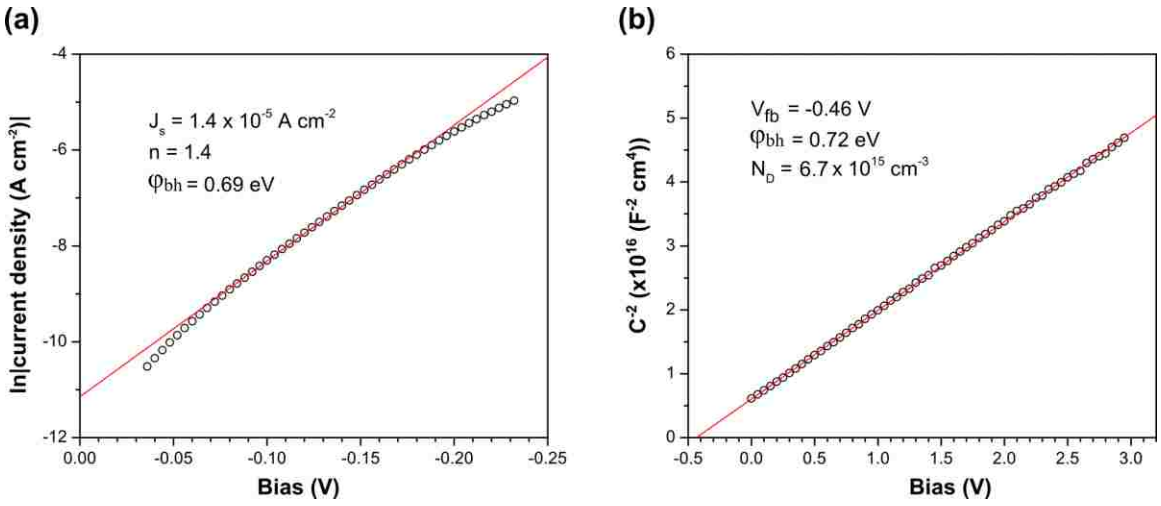

Figure 1.5. Junction characteristics of Au/n-Si. The red lines are linear fits of (a) the current-voltage curve and (b) the Mott-Schottky measurement

The response of a solid-state Au/n-Si Schottky diode can be calculated using the diode equation,[40]

$$J = J_s\left(exp^{qV/nkT} - 1\right) \tag{5}$$

where V is the voltage (V), n is the diode quality factor, k is Boltzmann's constant (1.38×10^{-23} J K^{-1}), T is the temperature (294 K), q is the charge of an electron (1.60×10^{-19} C), J is the measured current density (A cm^{-2}), J_s is the dark saturation current density (A cm^{-2}), J_L is the limiting current density (A cm^{-2}), R_s is the series resistance (Ω), and A is the area (cm^2). Figure 1.5a plots the current-voltage curve in ln(J) versus V scale; the slope gives a diode quality factor of 1.4, and the y-intercept (extrapolated value of current density at zero voltage) is the dark saturation current density. The barrier height can then be calculated from the dark saturation current using Equation 6,[40]

$$\varphi_{bh} = \frac{kT}{q} ln\left(\frac{A^{**}T^2}{J_s}\right) \tag{6}$$

where A^{**} is the effective Richardson's constant (120 A cm^{-2} K^{-2} for n-Si). The calculated barrier height is 0.69 eV from the current-voltage response measurement.

Other useful information about the junction energetics can be calculated from the Mott-Schottky equation,[15]

$$\frac{1}{C^2} = \frac{2}{q\varepsilon_s A^2 N_D}\left(V - V_{fb} - \frac{kT}{q}\right) \tag{7}$$

where C is the capacitance (F cm^{-2}), ε_s is the permittivity of silicon (1.05×10^{-12} F cm^{-2}), N_D is the carrier (donor) density, and V_{fb} is the flat band voltage; q, A, V, k and T are the same as described previously. The Mott-Schottky plot (Figure 1.5b) of C^{-2} versus reverse bias gives the doping density in the depletion region of 6.7×10^{15} cm^{-3} from the slope of the line, and a flat band voltage of -0.46 V from the x-intercept. The barrier height can be calculated from the flat band voltage using Equation 8,[40]

$$\varphi_{bh} = V_{fb} + V_n + \frac{kT}{q} - \Delta\varphi \tag{8}$$

where the $-\Delta\varphi$ term is the image-force-induced lowering of the potential energy. It can be calculated using Equation 9 if the breakdown voltage can be accurately determined,[40]

$$\Delta\varphi = \sqrt{\frac{q\mathcal{E}}{4\pi\varepsilon_s}} \tag{9}$$

where $\mathcal{E}$ is the maximum field at the interface associated with the dielectric breakdown. In Equation 8, V_n is the difference in energy between the conduction band and the Fermi level and can be calculated using Equation 10,[40]

$$V_n = kTln\left(\frac{N_C}{N_D}\right) \tag{10}$$

where N_C is the density of states in the conduction band (2.8×10^{19} cm^{-3}). N_D is the donor density obtained from the Mott-Schottky analysis or it can be measured separately using Equation 11,[15]

$$N_D = \frac{1}{q\mu\rho} \tag{11}$$

where μ is the electron mobility (1500 cm^2 V^{-1} s^{-1} in Si), and ρ is the resistivity of the silicon wafer (~1.77 Ω·cm, measured using a 4-point probe). The calculated barrier height from the Mott-Schottky analysis is 0.72 eV (without using $-\Delta\varphi$ in Equation 8), slightly larger than the 0.69 eV determined from the current-voltage response measurement. Mott-Schottky analysis often overestimates barrier heights because it assumes parabolic energy profile up to the interface.[40,67] The image force lowering term (if determined accurately) can bring the calculated barrier height closer to its true value. Therefore, the actual barrier height of the Au/n-Si diode should be close to the value determined from the forward bias current-voltage curve.

Photoelectrochemistry occurs at solution-semiconductor interfaces, which behave in an analogous manner to the metal-semiconductor junction discussed above. Recall the energy-band diagram in Figure 1.2, the work function of the metal term can be replaced with the electrochemical potential, $-qE°$ where $E°$ is the Nernst potential of the redox couple. For photoelectrochemical water splitting, the redox couples of interest are O_2/H_2O (at a photoanode) and H^+/H_2 (at a photocathode). Upon contact to the solution with the redox couple, electrons will flow between the semiconductor and the solution until equilibrium is established. A typical n-type semiconductor photoanode in equilibrium with the O_2/H_2O redox couple will carry an excess positive charge, arising from the ionized dopant atoms, in the depletion region of the semiconductor. The solution

will have an excess negative charge, but spread over a much narrower region (i.e., the *Helmholtz* layer, discussed in section 1.2.3.). The energy bands will bend in the similar fashion as in the case of a metal-semiconductor junction. The electric field strength depends on the initial energy difference between the value of $-qE°(O_2/H_2O)$ and the Fermi level of the semiconductor. Such energy difference is on the order of 1 eV, whereas the depletion width in a semiconductor is typically sub-micrometer. The resulting electric field in the semiconductor can easily reach 10^5 V cm^{-1}.[68] Photogenerated charge carriers can be very effectively separated by this large electric field, because of their high mobility (1500 cm^2 V^{-1} s^{-1} for electrons and 450 cm^2 V^{-1} s^{-1} for holes of Si). At an n-type semiconductor photoanode, the photogenerated electrons will flow towards the bulk of the electrode while the photogenerated holes move into the solution to participate in the oxidation of water.

The energy that can be extracted from the photogenerated electron-hole pairs defines the theoretical limits on the efficiency of the photoelectrode. The maximum internal energy that can be extracted from these pairs is given by the barrier height of the junction. To optimize the photoelectrochemical performance, the barrier height should be as large as possible. Since the barrier height is determined by the energy difference between $-qE°(O_2/H_2O)$ and E_c (for an n-type photoanode), tuning these energy levels can potentially improve the efficiency of the photoelectrode. Changing the redox couple changes $-qE°$, but for water oxidation and reduction, the redox couple is fixed. According to Nernst equation, the redox potential for water oxidation, for example, is pH dependent, as shown in Equation 12,

$$E°(O_2/H_2O) = 1.23\,V - 0.059\,V \times pH \qquad (12)$$

where the potentials are with respect to a normal hydrogen electrode (NHE). Although the implication suggests that the solution-semiconductor interfacial energetics can be tuned by adjusting the solution pH, this approach has been unsuccessful.[69] Another strategy is to tune the band edge positions by incorporating fixed diploes or charges on the semiconductor surface.[70] Researchers have been able to shift the band edges[71-75] by modifying the semiconductor surface, in attempts to improve the efficiencies of semiconductor photoelectrochemistry.

1.2.2. Oxygen Evolution Reaction Catalyst. Most of the oxygen evolution reaction catalysts consisting of earth-abundant transition metals are not stable in acidic solution.[76] Therefore, the studies on their catalytic activities are often done in alkaline solutions such as 1 M NaOH (pH 14). At pH 14, the overall water splitting is accomplished by two half reactions, as shown in Equations 13 and 14,[50]

$$2H_2O + 2e^- \leftrightarrows H_2 + 2OH^- \qquad E^\circ = -0.83\ V_{NHE} = -1.03\ V_{Ag/AgCl} \qquad (13)$$

$$O_2 + 2H_2O + 4e^- \leftrightarrows 4OH^- \qquad E^\circ = 0.40\ V_{NHE} = 0.20\ V_{Ag/AgCl} \qquad (14)$$

where E°, the standard reduction potentials are expressed with respect to NHE and Ag/AgCl reference electrodes. This implies that the minimum energy for splitting water requires 1.23 V between the anode and the cathode. However, in typical applications, greater applied energy is necessary due to kinetic barriers that are commonly encountered in performing multistep, multielectron reactions. This additional voltage applied to the electrode relative to the redox potential of the couple (e.g., O_2/OH^-) is called the *overpotential*, η, as expressed in Equation 15 below.

Applied potential = overpotential + thermodynamic (redox) potential (15)

The overpotential is needed to drive the kinetically rate-limiting step in the multistep water oxidation (or reduction) reactions. The main function of a catalyst is to reduce the overpotential towards the desired reaction. The catalytic behavior of a given material is often evaluated by *i*) how much overpotential is required to reach a certain current density, and *ii*) how much current density can be obtained at a given overpotential. For oxygen evolution reaction catalysts, the benchmarking protocol[77] calls for the examination of the overpotential required to produce 10 mA cm^{-2}, the current density expected for a 10% efficient solar water-splitting cell,[66,78,79] and the measurement of current density at η = 350 mV[66,78,80] in 1 M NaOH. For example, a generic "good" OER catalyst can drive a current density of 10 mA cm^{-2} using only ~100 mV overpotential, whereas a "bad" OER catalyst will need ~600 mV or more overpotential to achieve the same current density.[66] Some of the best known OER catalysts, such as RuO_2,[81] can drive a 10 mA cm^{-2} OER current density with 290 mV overpotential.[76] In an effort to search for earth-abundant OER catalysts that meet or exceed the catalytic performance of those containing noble metals (e.g., Ir and Ru), various compounds of Fe, Co, and/or Ni have been under investigation.[76] Recently, a form of nickel selenide—Ni_3Se_2—was found to accomplish OER catalytic performance on par with RuO_2.[82]

The catalytic performance of an electrode can be described by a Tafel relationship, shown in Equation 16,[50]

$$\eta = a + b \cdot \log i \tag{16}$$

where η is the overpotential, i is the measured current, and a is the *log* of exchange current. The Tafel slope, b, is the extent of potential increase required to raise the current 1 order of magnitude, thus commonly expressed in voltage per decade (mV dec^{-1}). The

exchange current can be determined from the x-intercept of the η versus log(I) plot (i.e., a Tafel plot), and is often described in terms of geometric area as the exchange current density, J_0 (A cm^{-2}). The exchange current density is a measure of how vigorously the forward and reverse reactions occur during dynamic equilibrium and thus yields the standard heterogeneous rate constant k^0.[83] Although the exchange current density alone provides ample information for evaluating catalytic performance, the Tafel slope is also an important parameter. The Tafel slope gauges how efficiently an electrode can produce current in response to an applied potential. It also accounts for changes in reaction mechanism at different overpotentials. However, due to the extreme irreversibility of the oxygen evolution process,[84] the steady state kinetic analysis of the OER can only provide mechanistic information up to and including the rate-determining step (RDS).[83]

The experimentally observed Tafel slope of multistep reactions such as the OER can be described in Equation 17,[85,86]

$$b = 2.303\left(\frac{RT}{\vec{\alpha}F}\right) \tag{17}$$

where R is the gas constant (8.314 J mol^{-1} K^{-1}), T is the absolute temperature (K), F is the Faraday constant (96485 C mol^{-1}), and $\vec{\alpha}$ is the transfer coefficient given by Equation 18,[83]

$$\vec{\alpha} = \frac{\vec{n}}{\nu} + n_r\beta \tag{18}$$

where $\vec{n}$ is the number of electrons transferred prior to RDS, ν is the stoichiometric number defined as the number of times the RDS occurs for each repetition of the overall reaction, n_r is the number of electrons transferred during each RDS, and β is the symmetry factor, usually taken to be ½, associated with the activation of vibrational

states and the energy required to break bonds.[83] It can be seen that Tafel slopes commonly adopt values of 120, 60, and 40 mV dec^{-1} at 25°C as explained in the following. If the first electron transfer step is the rate-determining step, then $n_r = 1$, $\vec{n} = 0$, and $\vec{\alpha} = \beta = 1/2$, resulting in a Tafel slope of about 120 mV dec^{-1}. Likewise, if the second electron transfer step is the RDS, then $n_r = 1$, $\vec{n} = 1$, and assuming $\nu = 1$, thus $\vec{\alpha} = 3/2$ and Tafel slope is about 40 mV dec^{-1}. Alternatively, if the first electron transfer step is followed by a rate-determining chemical step, then $n_r = 0$, $\vec{n} = 1$, again assuming $\nu = 1$, thus $\vec{\alpha} = 1$ and Tafel slope is about 60 mV dec^{-1}. Therefore, by analyzing the Tafel slopes, one can differentiate between possible reaction mechanisms.

A general mechanism for the OER on metal oxides in acidic solutions is proposed based on experimentally obtained Tafel slopes as shown in Scheme 1.4.[66] The first step (a) of oxygen evolution reaction is the discharge of water to oxidize a surface-active site (asterisk), corresponding to a Tafel slope of 120 mV dec^{-1}. This produces an unstable intermediate species, designated in square brackets in (b) and (c). After chemical conversion to a more stable surface species (b; 60 mV dec^{-1}), the surface is oxidized

(a) $*OH + H_2O \rightarrow [HO*OH] + H^+ + e^-$

(b) $[HO*OH] \rightarrow HO*OH$

(c) $HO*OH \rightarrow O*OH + e^- + H^+$

(d) $2O*OH \rightarrow 2*OH + O_2$

Scheme 1.4. General mechanism for the OER on metal oxides in acidic solutions

further (c; 40 mV dec^{-1}). Upon the reaction of two highly oxidized surface sites, oxygen is finally liberated (d). The multistep reaction mechanism and the involvement of several intermediates add complexity to the kinetics of the oxygen evolution reaction. The use of OER catalysts is an attempt to tackle the kinetic bottleneck in water splitting.

A catalyst, by definition, must improve the kinetics of the desired reaction. In the case of OER, the catalyst must be capable of producing large quantities of oxygen at a minimum overpotential as quickly as the absorber can supply holes to the catalyst. An effective catalyst must also be robust enough to maintain its efficiency over practical time scales. For photoelectrochemical applications, the catalysts are usually deposited as thin layers or as nanoparticles to minimize light absorption or reflection, and to preserve desired interfacial energetics. CoOOH and Co_3O_4 are known OER catalysts.[46,87,88] The effect of OER catalysis can be easily observed when comparing the oxygen evolution activities of an inert substrate with and without the catalyst. In Paper I, Figure 5 shows an excellent example where three electrodes are subjected to linear sweep voltammetry (LSV) at 1 mV s^{-1} in 1 M KOH at room temperature. The bare Ti substrate does not show any noticeable OER current, whereas the $Co(OH)_2$ and Co_3O_4 modified electrodes show the onset of OER at about 0.5 V and the current densities reach 100 and 40 mA cm^{-2}, respectively at 1 V. Note that the surface of $Co(OH)_2$ becomes CoOOH under oxidation conditions (demonstrated in Paper I and II) thus promoting OER catalytic activities.

1.2.3. Electrochemically Active Surface Area Measurement. The activities of OER catalysts are often evaluated by how much OER current density can be produced at a given overpotential or how much overpotential is required to reach a certain OER current density. The ability to measure or estimate the surface area of an electrode is

essential to calculate accurate current densities and thus becomes a crucial part of catalyst benchmarking. Although there are many ways to measure surface areas, electrochemists are most interested in the electrochemically active surface area of the electrodes. Underpotential deposition (UPD) of metals is a favorable method for electrochemists to accurately measure the real surface area because the metal atoms will adsorb for only a monolayer on the surface of the electrode. The atomic coverage (i.e., atoms per area) of common UPD materials is well documented, so the area of the electrode can be calculated based on the charges passed during adsorption or desorption of the monolayer. Figure 1.6 is an example of Pb UPD study on a Au sputtered glass (Au-glass) sample. The working electrode is the Au-glass, the reference electrode is a lead strip, and the counter electrode is a Au coil. The UPD is accomplished by scanning cyclic voltammetry (CV) in an Ar-saturated solution containing 1 mM $Pb(ClO_4)_2$ and 10 mM $HClO_4$ at room

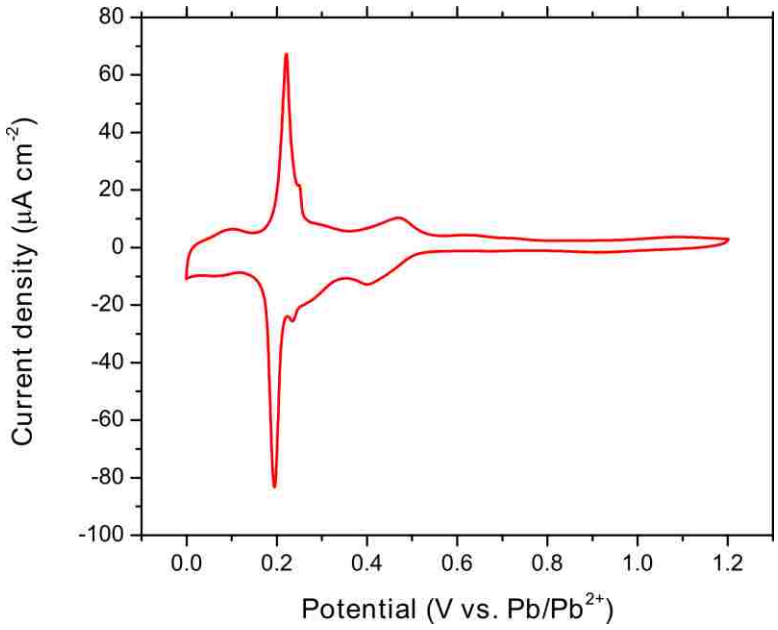

Figure 1.6. CV of Pb UPD on Au-glass

temperature. The scan rate is 20 mV s^{-1} starting in the cathodic direction. The cathodic and anodic peaks correspond to the different adsorption and desorption mechanisms, respectively. Note that the features seen in Figure 1.6 are similar to the literature reported Pb UPD on Au(111) single crystal,[89,90] meaning that the surface of the Au-glass largely presents Au(111) faces. Typically, the desorption peaks of UPD are better defined and are often used to characterize the electrode surfaces, including surface areas. In Figure 1.6, the total charge associated with Pb desorption is 393 μC. Assuming 275 μC cm^{-2} of Pb monolayer desorption,[91] the electrochemically active surface area of the Au-glass electrode is 1.43 cm^2. The geometric area of this electrode is 1.3 cm^2, hence the roughness factor of the Au surface is 1.1.

The electrochemically active surface area of the Au-glass can also be determined through a Au oxide reduction experiment. Figure 1.7 on the next page shows a CV at 20 mV s^{-1} in 0.1 M H_2SO_4 performed on the same Au-glass. The anodic peaks are associated with the oxidation of the Au surface. The sharp reduction peak at 0.9 V accounts for 660 μC of charge passed, indicated by the shaded area. Using 482 μC cm^{-2} Au oxide reduction charge reported in the literature,[92] the electrochemically active surface area of this particular sample is 1.37 cm^2, corresponding to the roughness factor of 1.05, in close agreement with the value determined by the Pb UPD method.

Many OER catalysts under current study are oxides and (oxy-)hydroxides. The surface area determination of these materials is a challenge because they are not suitable for the common surface area measurement methods such as those mentioned above. One alternative is to measure the electrochemical double layer capacitance, C_d, of the catalytic surface.[93] In a solution, the surface of an electrode is covered with a layer of solvent

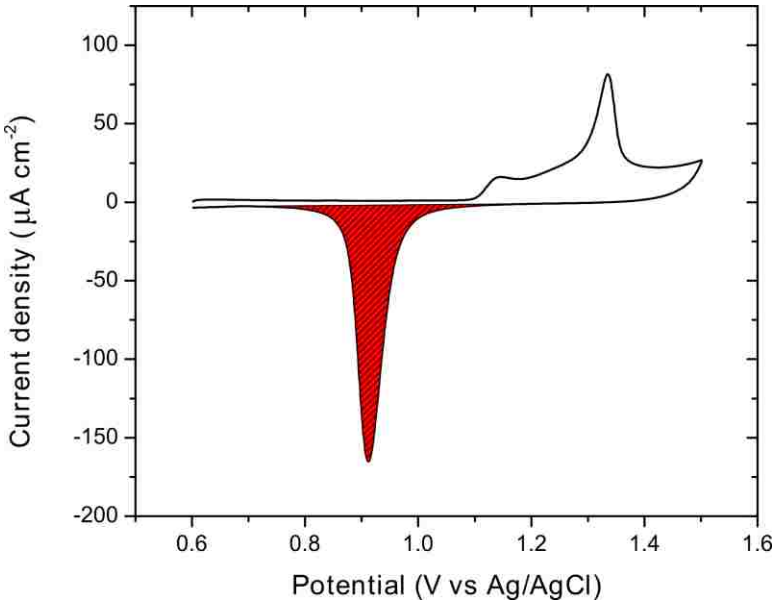

Figure 1.7. Au surface area determination by measuring the Au oxide reduction charge (shaded area) in 0.1 M H_2SO_4

molecules and sometimes specifically adsorbed ions or molecules. This layer is called the *inner Helmholtz* or *Stern layer*. The solvated ions can only approach the surface of the electrode at a distance defined by the *inner Helmholtz layer* and the diameter of the solvent molecules. These solvated ions are nonspecifically adsorbed and their distribution extends into the bulk of the solution, forming the *diffuse layer*. Together, the *electrical double layer* contributes to the capacitive behavior when charges accumulate in the solution near the biased electrode. The charge divided by the electrode surface area is the charge density (μC cm^{-2}), and the charge density divided by the applied potential is the specific capacitance (μF cm^{-2}). If we know the specific capacitance of a material with a known surface area, i.e., the Au surface characterized using previous methods, then the surface area of the electrode of interest can be back calculated using the measured C_d. A

major assumption here is that the specific capacitance is material independent. In the literature, the values of C_d typically fall between 10 and 40 μF cm^{-2}.[50] That is, by assuming the same specific capacitance for different materials, the surface area could be under- or overestimated by a factor of 4.

Unlike real capacitors, whose capacitances are independent of the voltage across them, C_d is often a function of potential. Double layer capacitance measurements are done in a narrow potential range (±20 mV vs. OCP) to minimize the potential dependence and to avoid Faradaic reactions. In an effort to standardize the electrochemically active surface area determination technique, Jaramillo and coworkers[76] proposed measuring the C_d by sweeping the potential ±50 mV vs. OCP at different scan rates in 1 M NaOH. This is a convenient approach because OER catalysis studies are commonly performed in alkaline solutions such as NaOH. However, cations are known to intercalate into oxide layers causing large pseudo capacitance.[93-95] Alternatively, an acetonitrile solution of tetrabutylammonium hexafluorophosphate ($TBAPF_6$) can be used as the electrolyte to avoid intercalation because of the large cations in the system.[46,96] This method is described in more detail in Paper II. After all, knowing the electrochemically active surface areas of the electrodes is crucial in comparing catalytic activities of different OER catalysts.

1.3. MATERIALS CHARACTERIZATION

Materials characterization is an essential element for synthetic chemists and materials scientists. Many characterization instruments are dedicated to analyze and provide certain information about the synthesized materials. For inorganic materials,

information such as chemical composition, oxidation states, resistivity, crystallinity, and structural orientation are all important parameters to know about a material. In Papers I, II, and III, the characterization of those parameters are demonstrated. To avoid an exhaustive review of the commonly used characterization techniques, this section will focus on the less exploited techniques for sample thickness determination.

In many cases, the information about the thicknesses of the deposited films becomes important when, for instance, estimating the current efficiency of the deposition and when calculating the extinction coefficient of the films from spectrophotometry measurements. If part of the film can be removed from the substrate leaving a clean edge of the remaining film intact with the substrate, profilometry may be used to probe the elevation profile from the top of the substrate to the top of the film, thus yielding the thickness of the film. Common profilometry instruments include atomic force microscope (AFM) and a conventional profilometer. Another straightforward method to determine the film thickness is to obtain a cross-section image of the sample. If the film is deposited on a fragile substrate (e.g. Au-coated glass or a Si chip), the sample can simply be snapped in halves by hand. Otherwise, a focused ion beam (FIB) milling can create a small cross-section on a selected area of the sample. The cross-sections can then be examined under a scanning electron microscope (SEM) and the thickness can be determined from the image. For ultra-thin films where the required resolution of the cross-sectional image exceeds the limit of the SEM (typically 1-5 nm), other techniques are employed to acquire the thickness information. One method to image an ultra-thin film is to cut out a FIB slice and analyze it using the transmission electron microscope (TEM) whose resolution is typically ~0.25 nm. Although all the techniques above allow

direct measurement of the film thickness, they probe only a small area of the sample and they require some forms of alternation, after which the samples may or may not be useable for other experiments. The following subsections introduce some functions of X-ray diffraction (XRD) as non-destructive techniques for analyzing ultra-thin films.

1.3.1. X-ray Diffraction. X-rays, discovered by a German physicist Wilhelm Röntgen in 1895, are a form of electromagnetic radiation having wavelengths on the order of 0.01 to 10 nm. At this scale, the X-rays are capable of probing structures as small as the inter-atomic distance in condensed matter. X-ray diffraction works on the principles of scattering by the regularly spaced atoms in a crystal. X-ray diffraction is a powerful and versatile tool for identifying crystal structure, crystallite size, texture, stress and even thickness of a smooth sample. Film thickness can be determined via peak broadening, Laue oscillation, and reflectivity measurements as explained in the following.

1.3.1.1. Peak broadening. In 1918, Swiss physicist Paul Scherrer determined the inverse relationship between the width of the XRD peak and the crystallite size. Assuming the XRD peak broadening is due solely to the crystallite size, their relationship can be described by the Scherrer equation (Equation 19),

$$\tau = \frac{K\lambda}{\beta cos\theta} \tag{19}$$

where τ is the particle size or film thickness, K is a dimensionless shape factor ~0.9, λ is the X-ray wavelength, β is the full width of the peak at half of the maximum intensity of the peak (FWHM), and θ is the position of the center of the peak (2θ) devided by 2. For the particular Au on Si sample described in Section 1.1.1, the peak broadening is observed in the X-ray 2θ pattern, as shown in Figure 1.8. The FWHM of the Au(111)

peak is 0.35° and the peak is centered on $2\theta = 38.18°$. Using Equation 19, the thickness of the Au film is estimated to be ~24 nm.

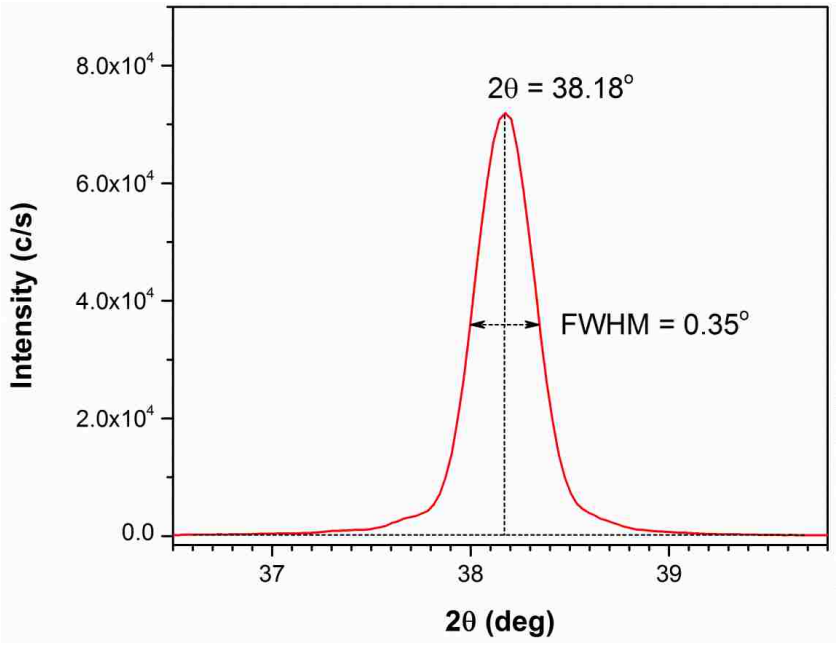

Figure 1.8. Peak broadening in 2θ pattern of the Au(111) peak

The above analysis neglects the instrumental broadening and broadening due to nonuniform strain. The instrumental broadening effect can be simply subtracted from the FWHM of the XRD pattern. The broadening due to nonuniform strain, however, requires the following analysis described by English metallurgist G.K. Williamson and his student W.H. Hall in 1953. The Williamson-Hall equation (Equation 20) is a modified version of Scherrer equation accounting for the effect of nonuniform strain ($\frac{\Delta d}{d}$) on total peak broadening (β_{total}).

$$cos\theta \cdot \beta_{total} = \frac{K\lambda}{\tau} + 4\left(\frac{\Delta d}{d}\right) sin\theta \quad (20)$$

By plotting $cos\theta \cdot \beta_{total}$ vs. $sin\theta$, one can obtain the strain from the slope and the particle size from the y-intercept. One can also conclude that if the nonuniform strain was present in the sample, the crystallite size calculated from Scherrer equation would be smaller than the actual crystallite size.

1.3.1.2. Laue oscillations. German physicist Max von Laue was awarded the 1914 Nobel Prize in Physics for his discovery of the diffraction of X-rays by crystals. He also observed that in highly resolved XRD 2θ pattern, signal oscillation occurred due to the constructive and destructive interference of the reflected waves. When the incident beam interacts with highly ordered planes of atoms, or superlattices, it produces many parallel reflected waves whose interference effect is more pronounced (than that of less ordered structures). This results in satellite peaks at lower (labeled −1, −2, etc.) and higher (labeled +1, +2, etc.) angles of the main Bragg peak, as presented in Figure 1.9 on the next page.

The orders of the observed satellite peaks and their respective peak positions can be used to calculate the film thickness as shown in Equation 21,

$$\Lambda = \frac{\lambda(L_1 - L_2)}{2(sin\theta_1 - sin\theta_2)} \quad (21)$$

where Λ is the modulation wavelength—the bilayer thickness of two alternating materials in a superlattice—which is regarded as the film thickness in this application, and L_1 and L_2 are the satellite peak orders. Based on the observed satellite peak positions in Figure 1.9, the calculated Au thickness is ~22 nm using Equation 21.

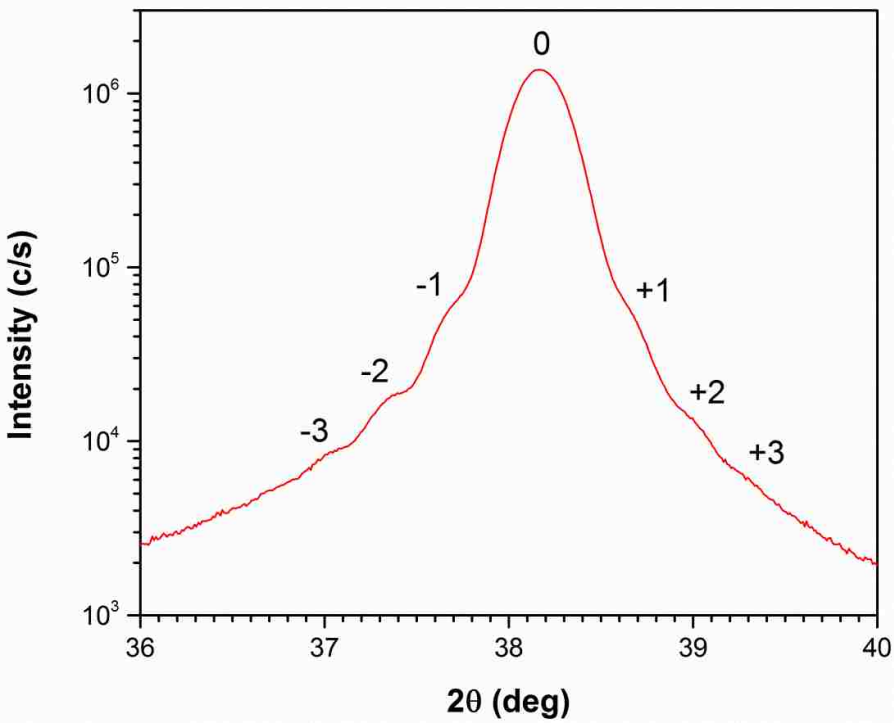

Figure 1.9. Laue oscillation observed on Au(111) peak

1.3.1.3. X-ray reflectivity. The X-ray reflectivity technique probes the sample at very low angles ($0.2° < 2\theta < 5°$). The detected signal originates from the specular reflection of X-rays when they encounter a change in electron density regardless of the material crystallinity. In the typical three-system scenario of air/film/substrate, the specular reflection happens at the air/film interface and the film/substrate interface, assuming sufficient smoothness of those interfaces.

In a simple system of a bare substrate, the X-rays are reflected at angles less than the critical angle of the substrate. For SiO_2, $\theta_c = 0.21°$. In the three-system scenario described earlier, the reflections from both air/film and film/substrate interfaces interfere

causing Kiessig fringes.[97] Figure 1.10 displays the XRR measurement of the aforementioned Au/Si sample.

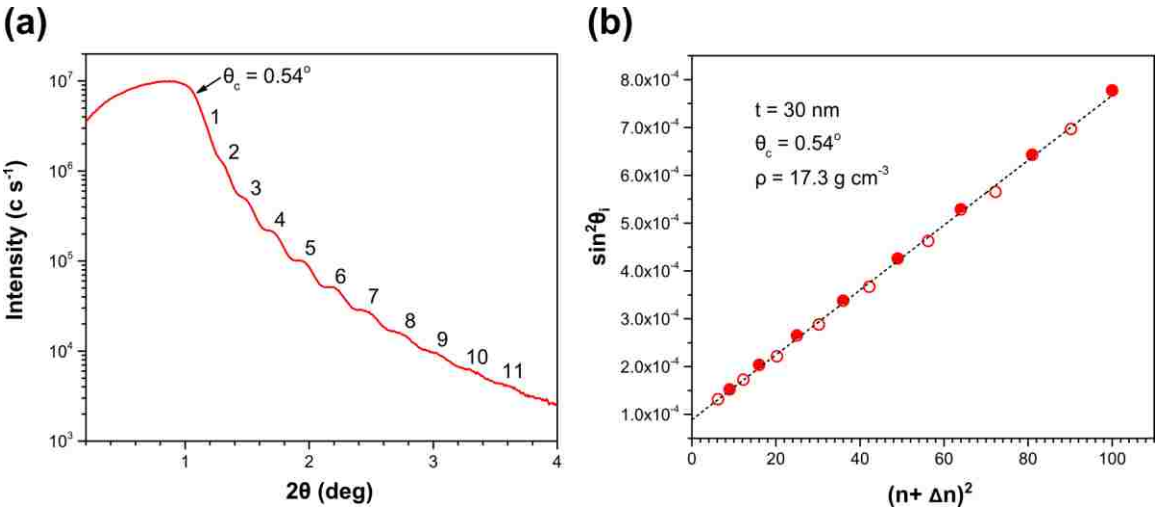

Figure 1.10. X-ray reflectivity measurement on Au/Si. The Kiessig fringes in (a) are indicated by the numbers, and their corresponding θ positions are plotted in (b).

The positions of the local fringe maxima θ_i of the specular reflected X-ray beam is given by the modified Bragg's law[98] (Equation 22) to include the critical angle θ_c,

$$n_i\lambda = 2t\sqrt{sin^2\theta_i - sin^2\theta_c} \tag{22}$$

where t is the thickness of the film and n_i is the order of the ith minima. This equation can be further modified[99] to accommodate for the fringe maxima, shown in Equation 23,

$$(n_i + \Delta n)\lambda = 2t\sqrt{sin^2\theta_i - sin^2\theta_c} \tag{23}$$

where $\Delta n = 0$ or ½ for fringe minima and fringe maxima, respectively. By rearranging Equation 23, a linear relationship between film thickness and sine of fringe extrema can be obtained, as shown in Equation 24 and 25,[99]

$$sin^2\theta_i = \frac{(n_i + \Delta n)^2\lambda^2}{4t^2} + sin^2\theta_c \tag{24}$$

or $$sin^2\theta_i = \frac{(n_i+\Delta n)^2\lambda^2}{4t^2} + \theta_c^2 \quad \text{(for small angles where } sin\theta \approx \theta\text{)}. \tag{25}$$

To extract useful information from the XRR measurement, the data should be plotted as $sin^2\theta_i$ vs. $(n_i + \Delta n)^2$, as shown in Figure 1.10b. According to Equation 25, the slope of the trend line equals to $\frac{\lambda^2}{4t^2}$, and the y-intercept equals to θ_c^2. In Figure 1.10b, the slope of the trend line is 6.8×10^{-6}, yielding the Au thickness of ~30 nm, and the intercept of 8.9×10^{-5} gives the critical angle of 0.54°.

During low angle X-ray measurements, such as XRR, part of the X-ray is reflected off of the substrate surface and part of it penetrates into the substrate. When the incident angle is low enough, i.e., below the critical angle, no more X-ray penetrate into the substrate and the result is *total internal reflection* within the film. The critical angle can provide information about the density of the film, assuming negligible anomalous dispersion, by Equation 26,[100]

$$\theta_c^2 = \frac{N_A r_e \lambda^2 f}{\pi A}\rho \tag{26}$$

where N_A is Avogadro's number, r_e is the classical electron radius (2.8179×10^{-13} cm), λ is the X-ray wavelength, f is the real part of the atomic scattering factor for Au, which is close to its atomic number (Z = 79), A is the average atomic mass (196.97 g mol^{-1} for Au), and ρ is the film density. From the critical angle 0.54° calculated previously, the

density of the Au film is 17.3 g cm^{-3}. Considering the bulk Au density of 19.3 g cm^{-3}, the electrodeposited Au film is ~90% dense.

In summary, all three X-ray techniques introduced in this section provide the thickness values in a reasonable range. Note that the peak broadening analysis by the Scherrer equation may be in error because some strain is present in the sample. Because only Au(111) and Au(222) peaks are observed in a 2θ scan, there are only two data points for Williamson-Hall analysis, thus limiting the separation of strain effect from the size effect. For Laue oscillations, the accurate reading of the peak positions is the key leading to the final thickness calculation. In XRR measurement, the determination of fringe orders is crucial in obtaining the right thickness and density calculations. If practiced carefully, all three X-ray techniques can serve as useful tools for non-destructive thin film thickness determination.

PAPER

I. DEPOSITION OF β-$Co(OH)_2$ FILMS BY ELECTROCHEMICAL REDUCTION OF TRIS(ETHYLENEDIAMINE)COBALT(III) IN ALKALINE SOLUTION

*Jakub A. Koza, Caleb M. Hull, Ying-Chau Liu, and Jay A. Switzer**

Missouri University of Science and Technology, Department of Chemistry and Graduate Center for Materials Research, Rolla, MO 65409-1170, USA

ABSTRACT

Films of β-$Co(OH)_2$ with a dense microcone morphology are electrodeposited at room temperature by reducing tris(ethylenediamine)cobalt(III) in alkaline solution. The synthesis exploits the fact that the kinetically-inert Co(III) complex of ethylenediamine (en) is 35 orders of magnitude more stable than the kinetically-labile Co(II) complex. $[Co(en)_3]^{3+}$ is therefore stable in alkaline solution, but $[Co(en)_3]^{2+}$ reacts with excess hydroxide ion to produce β-$Co(OH)_2$. The electrodeposited β-$Co(OH)_2$ is an active catalyst for the oxygen evolution reaction. Raman spectroscopy suggests that the surface of β-$Co(OH)_2$ is converted to CoOOH at the potentials at which oxygen evolution occurs.

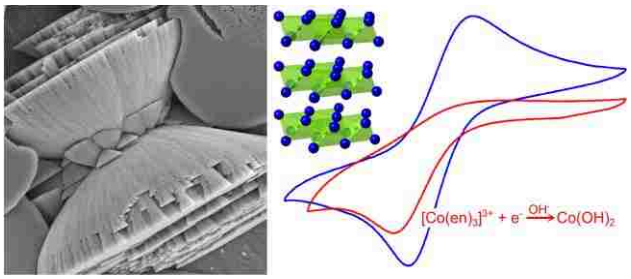

KEYWORDS

Cobalt hydroxide, $Co(OH)_2$, electrodeposition, oxygen evolution reaction, oxygen evolution catalyst

INTRODUCTION

Cobalt hydroxide, β-$Co(OH)_2$, is a promising material for energy conversion and storage. It is a common additive in Ni-based rechargeable alkaline batteries.[1] Nano-architectured $Co(OH)_2$ pseudocapacitors have shown a specific capacity as high as 2800 F g^{-1} without significant deterioration upon cycling.[2] $Co(OH)_2$ is known as an earth-abundant catalyst for the oxygen reduction[3] and hydrogen evolution[4] reactions. It is also an active catalyst for ozone and *p*-chloronitrobenzene decomposition in water.[5] In addition, $Co(OH)_2$ exhibits the giant reversible magnetocaloric effect, which makes it a promising candidate for low temperature magnetic refrigeration applications.[6] $Co(OH)_2$ can be oxidized electrochemically[1,4] to CoOOH, which is an excellent oxygen evolution reaction (OER) catalyst,[4,7] and it is used in room temperature CO sensors.[8] Several other groups have shown that $Co(OH)_2$ nanoplatelets can be electrodeposited using OH^- that is generated by reduction of nitrate ions.[3,9-11] Here, we introduce a method to electrodeposit crystalline β-$Co(OH)_2$ films. Dense $Co(OH)_2$ microcones are electrodeposited potentiostatically from a solution of 45 mM $[Co(en)_3]^{3+}$ (en − ethylenediamine) in 2 M NaOH (pH ≈ 14) at room temperature. We also show that the electrodeposited $Co(OH)_2$ is an active OER catalyst.

EXPERIMENTAL SECTION

Tris(ethylenediamine)cobalt(III) synthesis. $[Co(en)_3]Cl_3$ was synthetized using a literature procedure.[12] One solution was prepared by dissolving 12 g of $CoCl_2 \cdot 6H_2O$ in 35 mL of water. Another solution was prepared by dissolving 6 mL anhydrous ethylenediamine in 25 mL of water, cooled down to 0°C and partially neutralized with

8.5 mL of 6 M HCl. Both solutions were mixed together, and 10 mL of 30 % H_2O_2 was added while stirring the solution. The solution was boiled until it evaporated to a volume of approximately 60 mL. 60 mL of 12 M HCl was added, followed by addition of 120 mL of ethanol. The solution was cooled to about 0°C and the precipitate, which is $[Co(en)_3]Cl_3 \cdot 1{-}3H_2O$, was filtered and washed with ice-cold ethanol. The final product was dried in air.

Deposition solution. The electrolyte used for deposition of $Co(OH)_2$ was prepared by dissolving the appropriate amount of the as-synthetized $[Co(en)_3]Cl_3$ in 2 M NaOH to form a nominal 45 mM concentration.

Electrochemical methods. The electrodeposition experiments were performed in 125 ml of electrolyte at room temperature in a standard three-electrode setup using a Brinkmann PGSTAT 30 Autolab potentiostat. The electrolyte was stirred at a rate of 200 rpm with a magnetic stirrer. The in-situ mass changes were monitored with a Stanford Research Systems QCM200 electrochemical quartz crystal microbalance (EQCM). A Ti, an Au rotating disc electrode (RDE), and a Au sputtered quartz were used as the working electrodes. A Pt mesh served as the counter electrode. The Ti and Au-RDE substrates were mechanically polished, sonicated in acetone and rinsed with DI water prior to experiments.

The catalytic properties of the films for the OER were investigated in 1 M KOH solution at room temperature in a three-electrode cell using a Brinkmann PGSTAT 30 Autolab potentiostat. The deposit served as the working electrode and a Pt grid was the counter electrode. The OER experiments were performed on fresh layers immediately (after rinsing with DI water) after deposition. The potentials were corrected for the IR

drop, which was determined by electrochemical impedance spectroscopy. All potentials are referred with respect to the $Ag/AgCl/KCl_{sat.}$ reference electrode.

Characterization. The films were characterized using a high-resolution Philips X-Pert MRD X-ray diffractometer (XRD) with a $CuK_{\alpha 1}$ radiation source (λ = 1.54056 Å). XPS investigations were performed in a Kratos AXIS 165 spectrometer using monochromatic AlK_{α} radiation energy (1486.6 eV). Raman measurements were carried out using a Horiba Jobin-Yvon LabRam Aramis Microscope with a HeNe laser (λ = 633 nm) as the excitation source with an incident power of about 0.5 mW to minimize sample heating. The morphology of films was determoned by means of scanning electron microscopy (SEM – Hitachi S4700 FESEM) and atomic force microscopy (AFM) in the contact mode (Digital instruments Nanoscope III).

RESULTS AND DISCUSSION

We exploit the well-known inorganic chemistry that Co(III) favors nitrogen ligands over oxygen ligands, whereas Co(II) favors oxygen ligands over nitrogen ligands. $[Co(en)_3]^{3+}$ is nearly 35 orders of magnitude more stable than $[Co(en)_3]^{2+}$. The formation constants for $[Co(en)_3]^{3+}$ and $[Co(en)_3]^{2+}$ are 1048.69 and 1013.94, respectively.[13] Co(III) complexes are also substitutionally inert, whereas Co(II) complexes are substitutionally labile in aqueous solution.[14] Hence, $[Co(en)_3]^{3+}$ is stable in an alkaline solution, but $[Co(en)_3]^{2+}$ reacts with excess OH^- to produce $Co(OH)_2$. The formation constant of $Co(OH)_2$ is 1014.96.[15]

Figure 1a shows the cyclic voltammograms (CVs) measured on an Au electrode in the deposition solution (red) and in a solution of 45 mM $[Co(en)_3]^{3+}$ and 0.5 M

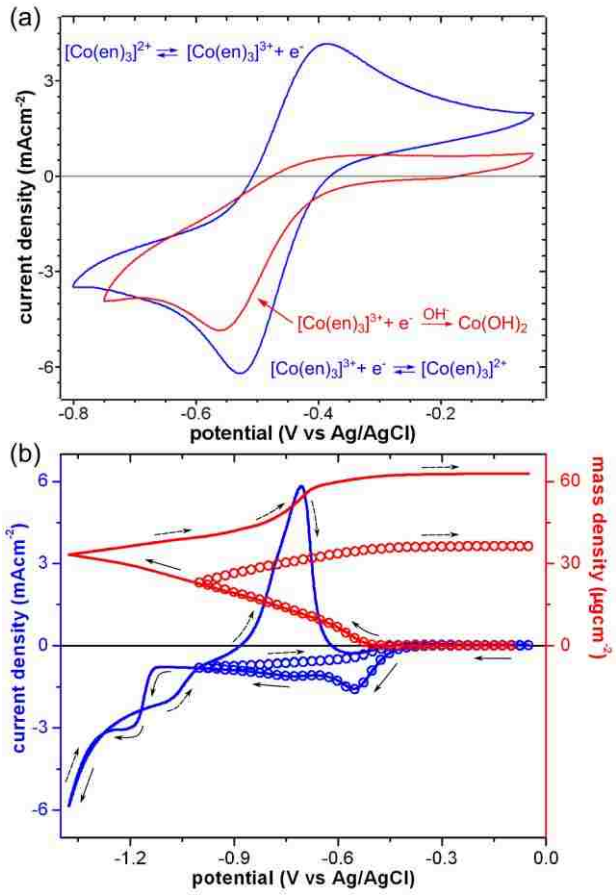

Figure 1. (a) CVs measured at an Au electrode in the $Co(OH)_2$ deposition electrolyte (red) and 45 mM $[Co(en)_3]^{3+}$ and 0.5 M ethylenediamine electrolyte of pH 9 (blue) at 100 mVs^{-1} scan rate. (b) CVs (blue) together with the corresponding mass changes (red) measured at an Au coated quartz crystal microbalance electrode in the deposition solution at 20 mV s^{-1} scan rate. The black arrows indicate the scan direction.

ethylenediamine of pH 9 (blue). The CV measured in the solution containing excess ethylenediamine (blue) shows quasireversible $[Co(en)_3]^{3+/2+}$ oxidation-reduction (eq 1) with a reduction peak at -0.525 $V_{Ag/AgCl}$ and an oxidation peak at -0.39 $V_{Ag/AgCl}$. In contrast, the CV obtained in the deposition solution (red), with a large excess of OH^-, shows irreversible behavior. A reduction peak at -0.55 $V_{Ag/AgCl}$ is observed without the corresponding oxidation peak. At this potential the mass also starts to increase (Figure 1b

– red), measured with an EQCM, due to the $Co(OH)_2$ formation (eq 2). The deposition of $Co(OH)_2$ occurs in the potential range of -0.5 to -1.1 $V_{Ag/AgCl}$. At more negative potentials Co is produced (eq 3), with a second peak in the CV at about -1.2 $V_{Ag/AgCl}$.

$$[Co(en)_3]^{3+} + e^- \leftrightarrows [Co(en)_3]^{2+} \quad (1)$$

$$[Co(en)_3]^{2+} + 2OH^- \rightarrow Co(OH)_2\downarrow + 3en \quad (2)$$

$$[Co(en)_3]^{3+} + 3e^- \rightarrow Co + 3en \quad (3)$$

Uniform pink films were deposited potentiostatically at -1 $V_{Ag/AgCl}$ and room temperature on Ti electrodes. The deposition proceeds with 100 % current efficiency (determined with the EQCM. Figure 2 shows the XRD pattern of the electrodeposited film. All reflections originating from the film can be assigned as β-$Co(OH)_2$ with the brucite $Mg(OH)_2$ layered structure with measured lattice parameters of a = b = 3.179 Å and c = 4.658 Å in $P\bar{3}m1$ symmetry. The intensity of the (001) peak is higher than that of the (101), suggesting a preferred [001] growth direction. Figure 3 shows the X-ray

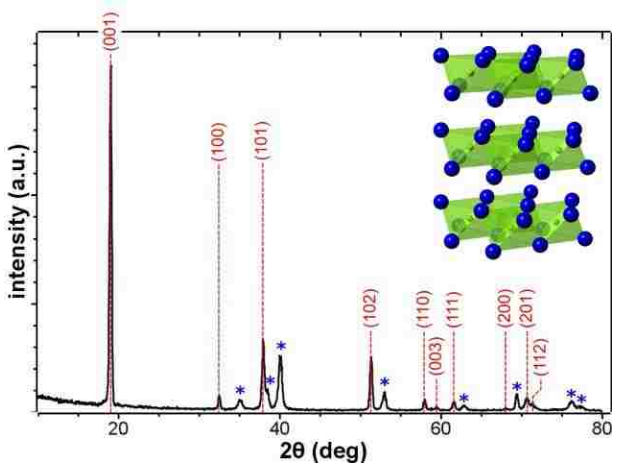

Figure 2. XRD pattern of electrodeposited $Co(OH)_2$. $Co(OH)_2$ reflections are indicated in red (JCPDS #30-0443), blue asterisks stand for the Ti substrate. The inset shows the $Co(OH)_2$ structure.

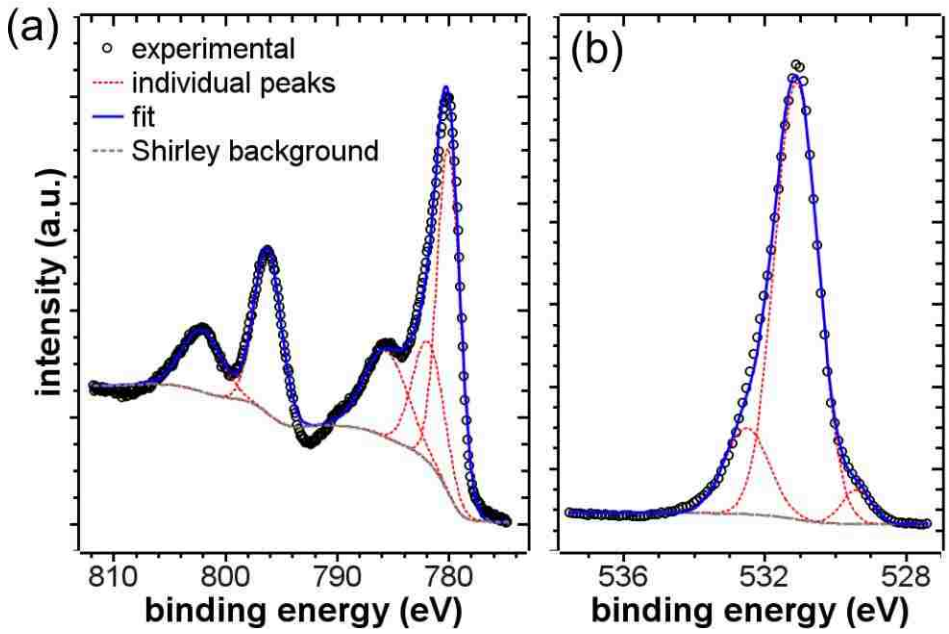

Figure 3. XPS spectra of electrodeposited $Co(OH)_2$. (a) Co2p and (b) O1s binding energy ranges.

photoemission (XPS) spectra of the as-deposited $Co(OH)_2$ film in the Co2p (a) and O1s (b) binding energy ranges. The XPS spectrum of the film in the Co2p binding energy range exhibits 5 deconvolved peaks at 780.2, 782, 790, 796.3 and 802.3 eV (Figure 3a) which match $Co(OH)_2$.[16,17] The O1s spectrum (Figure 3b) exhibits the main peak at 531.2 eV which corresponds to OH bonded to Co(II),[16,18] and two additional low intensity peaks at 529.4 and 532.5 eV corresponding to CoO and structural water, respectively.[2,18] The oxygen to cobalt ratio in the film was 2.05, consistent with stoichiometric composition.

Figures 4a,b show SEM images of the $Co(OH)_2$ film. The film consists of conical grains, which tend to align with the top disk surface parallel to the substrate. This morphology is very different than that of sparse, nanoplatelets electrodeposited via base

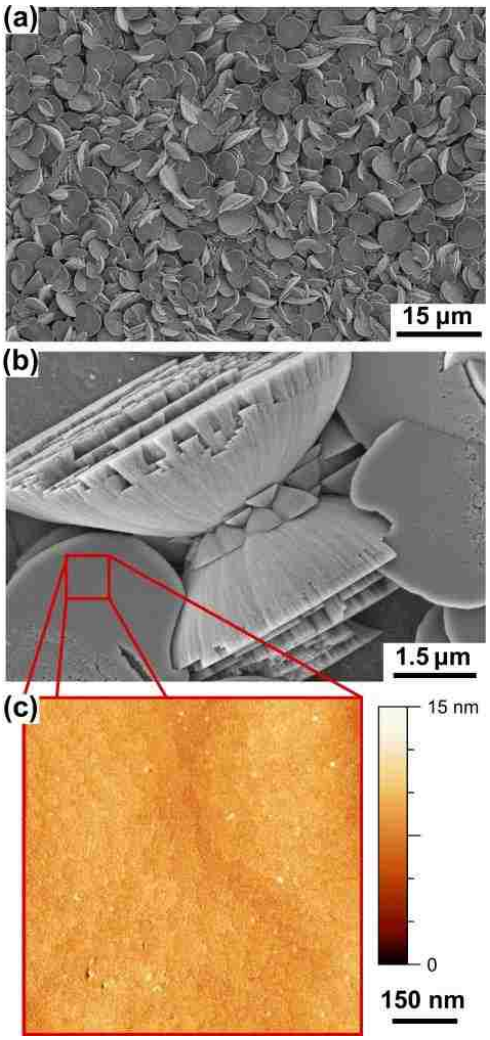

Figure 4. Morphology of electrodeposited $Co(OH)_2$ to a charge density of 0.6 C cm^{-2}. (a) and (b) SEM images of the film. (c) AFM image of a flat disk surface.

generation.[3,9-11] A closer look at the sidewalls of the cones reveals that they grow with an onion-skin-like morphology (Figure 4b).

Electrodeposited $Co(OH)_2$ is a potent catalyst for the OER. Linear sweep voltammograms (LSVs) at a scan rate of 1 mV s^{-1} on a Ti electrode (blue) and a $Co(OH)_2$-coated Ti electrode (red) in unstirred 1 M KOH at room temperature are shown in Figure 5. The LSV measured on electrodeposited, crystalline Co_3O_4 film, which is an

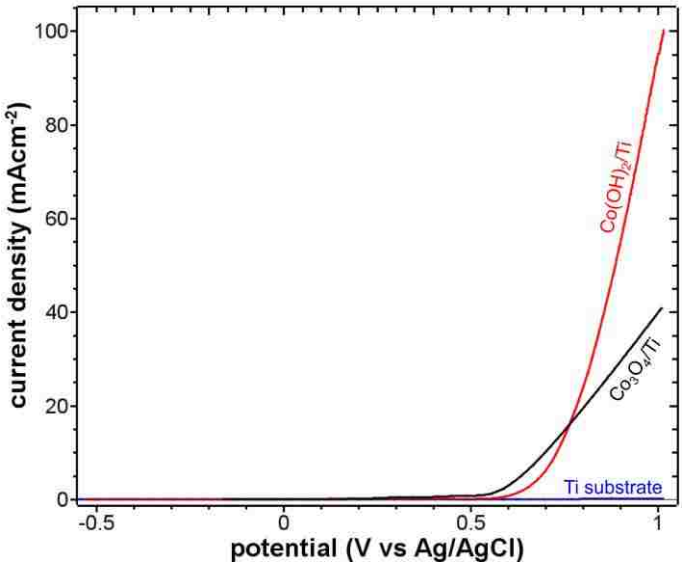

Figure 5. LSVs measured at 1 mVs^{-1} scan rate in 1 M KOH at electrodeposited $Co(OH)_2$ (red), crystalline Co_3O_4 (black) and uncoated Ti substrate (blue).

active OER catalyst,[19] is also shown (black) because the surface chemistry of both materials during OER is similar. From Figure 5 it is apparent that the electrodeposited $Co(OH)_2$ is an active catalyst for the OER. The onset of OER on $Co(OH)_2$ is 0.51 $V_{Ag/AgCl}$ which is about 50 mV higher than that measured on Co_3O_4. However, current densities, based on the geometry of the electrodes, are much higher on the $Co(OH)_2$ film at more positive potentials, possibly due to the roughness of $Co(OH)_2$ compared to the smooth Co_3O_4 film.[19] Figure 6 shows the initial CVs of the $Co(OH)_2$ film at 1 mV s^{-1} in 1 M KOH. In the first anodic scan (black) two peaks are observed. The first high current density peak (A_1) at 0.25 $V_{Ag/AgCl}$ is assigned to oxidation of $Co(OH)_2$ to CoOOH (eq 4).[2] The second peak (A_2) at about 0.4 $V_{Ag/AgCl}$ is attributed to the oxidation of CoOOH to CoO_2 (eq 5).[2] No reduction peak corresponding to A_1 was observed. The A_1 peak current density reduces dramatically in the second scan and is not detected in the fifth scan

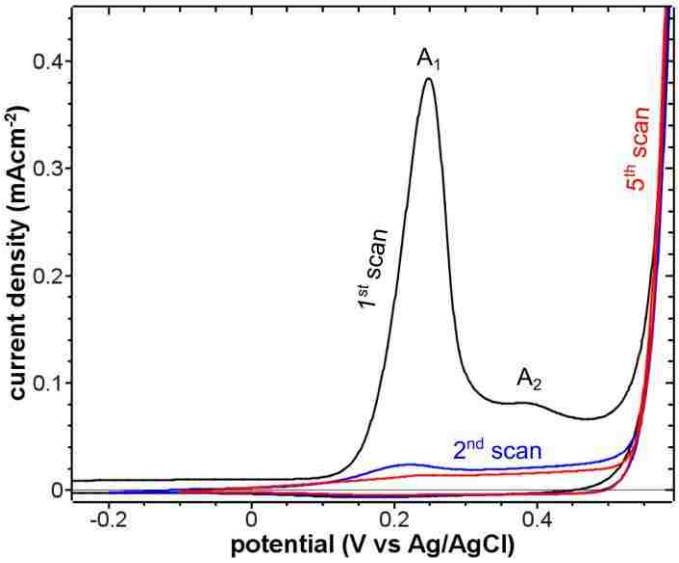

Figure 6. CVs of the $Co(OH)_2$ showing the film oxidation peaks prior to the onset of OER. Voltammograms measured at 1 mVs^{-1} scan rate in 1 M KOH.

indicating that the oxidation of $Co(OH)_2$ to CoOOH is irreversible. This is in agreement with results published by other researchers that $Co(OH)_2$ can be electrochemically oxidized to CoOOH.[1,4] The analysis of the deposition and oxidation charges shows that approximately 7 % of the film is oxidized.

$$Co(OH)_2 + OH^- \rightarrow CoOOH + H_2O + e^- \quad (4)$$

$$CoOOH + OH^- \rightarrow CoO_2 + H_2O + e^- \quad (5)$$

The film after OER experiments changes color from pink to black (Figure 7a). SEM investigations (not shown) did not reveal any morphological changes caused by film oxidation. Also the XRD pattern of the oxidized film did not show dramatic changes. Only a shoulder to the (001) peak is observed (indicated with an arrow in Figure 7b) which could be assigned to the CoOOH(003) reflection. Figure 7c shows Raman spectra of the as-deposited material (blue) and the film after OER experiments (red). The as-

deposited film spectrum (blue) matches that of $Co(OH)_2$.[20] The spectrum of the oxidized film (red) has the characteristic shape of CoOOH,[21,22] confirming the oxidation of $Co(OH)_2$ to CoOOH.

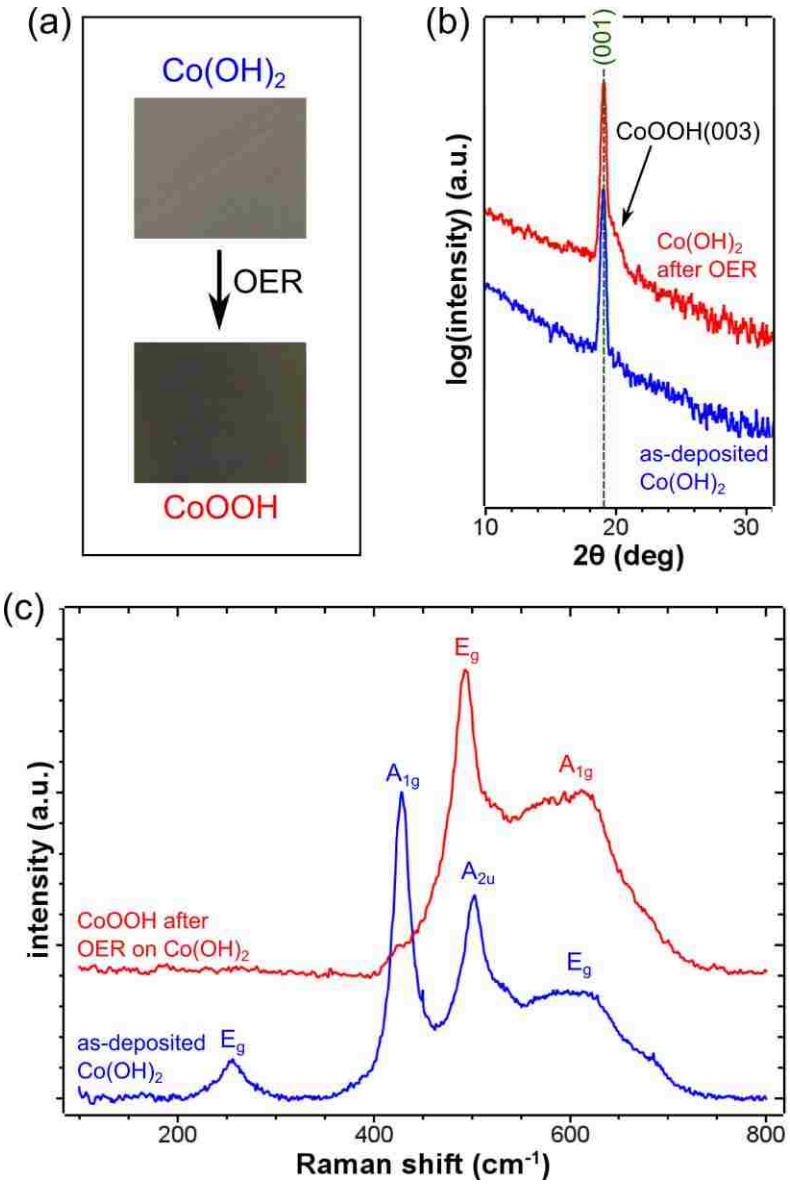

Figure 7**.** (a) Optical images of the $Co(OH)_2$ film prior to and after OER experiments. (b) XRD patterns of the as-deposited $Co(OH)_2$ film (blue) and the film after OER experiments. (c) Raman spectra of as-deposited $Co(OH)_2$ (blue) and the film after OER experiments (red).

CONCLUSIONS

We have shown that films of β-$Co(OH)_2$ can be deposited by electrochemical reduction of $[Co(en)_3]^{3+}$ in alkaline solution at room temperature. The low deposition temperature and cathodic deposition is ideal for electrodepositing $Co(OH)_2$ onto *n*-type semiconductor substrates. The as-deposited films are highly crystalline and do not require any further heat treatment. The β-$Co(OH)_2$ films exhibit excellent catalytic activity towards OER in 1 M KOH, comparable to Co_3O_4. During OER the surface of the material is oxidized to CoOOH, which is a conductive material,[1] minimizing the IR drop due to the film resistivity. As only the surface of pink $Co(OH)_2$ film oxidizes to black CoOOH, the film should not adsorb light as strongly as black Co_3O_4. This could prove to be important if the material is used as an OER catalyst on *n*-type semiconductors in photoelectrochemical cells.

AUTHOR INFORMATION

Corresponding Author

*E-mail: jswitzer@mst.edu

ACKNOWLEDGMENT

This work was supported by the U.S. Department Of Energy, Office of Basic Sciences under Grant No. DE-FG02-08ER46518.

REFERENCES

1. Pralong, V.; Delahaye-Vidal, A.; Beaudoin, B.; Leriche, J-B.; Tarascon, J-M. *J. Electrochem. Soc.* **2000**, 147, 1306.

2. Chang, J.-K.; Wu, C.-M.; Sun, I-W. *J. Mater. Chem.* **2010**, 20, 3729.

3. Wu, J.; Zhang, D.; Wang, Y.; Wan, Y.; Hou, B. *J. Power Sources* **2012**, 198, 122.

4. Subbaraman, R.; Tripkovic, D.; Chang, J. –C.; Strmcnik, D.; Paulikas, A. P.; Hirunsit, P.; Chan, M.; Greeley, J.; Stamenkovic, V.; Markovic, N. M. *Nat. Mater.* **2012**, 11, 550.

5. Xu, Z. Z.; Chen, Z. C.; Joll, C.; Ben, Y.; Shen, J. M.; Tao, H. *Catal. Commun.* **2009**, 10, 1221.

6. Liu, X. H.; Liu, W.; Hu, W. J.; Guo, S.; Lv, X. K.; Cui, W. B.; Zhao, X. G.; Zhang, Z. D. *Appl. Phys. Lett.* **2008**, 93, 202502.

7. Garcia-Mota, M.; Bajdich, M.; Viswanathan, V.; Vojvodic, A.; Bell, A. T.; Nørskov, J. K. *J. Phys. Chem. C* **2012**, 116, 21077.

8. Geng, B.; Zhan, F.; Jiang, H.; Xing, Z.; Fang, C. *Cryst. Growth Des.* **2008**, 8, 3497.

9. Yarager., M. S.; Steinmiller, E. M. P.; Choi, K.-S. *Chem. Commun.* **2007**, 159.

10. Zhou, W.-J.; Zhang, J.; Xue, T.; Zhao, D.-D.; Li, H. L. *J. Mater. Chem.* **2008**, 18, 905.

11. Brownson, J. R. S.; Lévy-Clément, C. *Electrochim. Acta* **2009**, 54, 6637.

12. Krause, R. A.; Megargle, E. A. *J. Chem. Ed.* **1976**, 53, 667.

13. *Lange's handbook of chemistry 15th Edition;* Dean, J. A., Ed; McGraw-Hill, Inc.: New York, 1999.

14. Marusak, R. A.; Doan, K.; Cummings, S. D. *Integrated approach to coordination chemistry: an inorganic laboratory guide;* John Wiley & Sons, Inc.: Hoboken, New Jersey, 2007.

15. *CRC Handbook of Chemistry and Physics 74th Edition;* Lide, D. R., Ed; CRC Press, Inc.: Boca Raton, 1994.

16. Yang, J.; Liu, H; Martens, W. N.; Frost, R. L. *J. Phys. Chem. C* **2010**, 114, 111.

17. Biesinger, M. C.; Payne, B. P.; Grosvenor, A. P.; Lau, L. W. M.; Gerson, A. R.; Smart, R. St.C. *J. Appl. Surf. Sci.* **2011**, 257, 2717.

18. *Handbook of X-ray Photoelectron Spectroscopy;* Chastain, J., Ed.; Perkin-Elmer Corporation: Eden Prairie, MN, 1992.

19. Koza, J. A.; He, Z.; Miller, A. S.; Switzer, J. A. *Chem. Mater.* **2012**, 24, 3567.

20. Shieh, S. R.; Duffy, T. S. *Phys. Rev. B* **2002**, 66, 134301.

21. Ludvigsson, M.; Lindgren, J.; Tegenfeldt, J. *J. Mater. Chem.* **2001**, 11, 1269.

22. Pauporté, T.; Mendoza, L.; Cassir, M.; Bernard, M. C.; Chivot, J. *J. Electrochem. Soc.* **2005**, 152, C49.

II. CONVERSION OF ELECTRODEPOSITED $Co(OH)_2$ TO CoOOH AND Co_3O_4, AND COMPARISON OF THEIR CATALYTIC ACTIVITY FOR THE OXYGEN EVOLUTION REACTION

*Ying-Chau Liu, Jakub A. Koza, and Jay A. Switzer**

Department of Chemistry and Graduate Center for Materials Research, Missouri University of Science and Technology, Rolla, Missouri, 65409-1170, United States

ABSTRACT

Cobalt hydroxide, β-$Co(OH)_2$, was electrodeposited cathodically from an alkaline solution of tris(ethylenediamine)cobalt(III). The $Co(OH)_2$ crystals grew into a microcone morphology and the surface became CoOOH at oxidizing potentials. The $Co(OH)_2$ film was fully converted to CoOOH by electrochemical oxidation at 95^{o}C in 1 M KOH and to Co_3O_4 by thermal decomposition at 300^{o}C in air. The $Co(OH)_2$ and CoOOH films grew with a [001] orientation on Au(111), and the converted Co_3O_4 films had a [111] orientation. The overall morphology was retained upon conversion. However, an increase in roughness was observed on the surface of the CoOOH and Co_3O_4 microcones. The electrochemically active area of the films was estimated from double layer capacitance measurements in acetonitrile with tetrabutylammonium hexafluorophosphate electrolyte. The CoOOH had a roughness factor of 9.4, and the Co_3O_4 had a roughness factor of 63.6. The catalytic activities of the films for the oxygen evolution reaction (OER) were compared by Tafel analysis in an O_2 saturated 1 M KOH at room temperature. The CoOOH and Co_3O_4 films appeared to exhibit different Tafel behavior

with Co_3O_4 being the superior catalyst when the geometric area was used in the Tafel analysis. However, when the observed current densities were corrected for the measured electrochemically active areas, the linear regions of the two Tafel plots fell on the same line. The results suggest that the active species, likely Co(IV), for the OER is the same on both materials. Both CoOOH and Co_3O_4 had a Tafel slope of 60 mV dec^{-1} and an exchange current density of 6.1×10^{-11} A cm^{-2}. The conversion method outlined in the paper provides a means to produce Co_3O_4 with a large electrochemically-active area.

KEYWORDS

Oxygen evolution reaction, cobalt hydroxide, cobalt oxyhydroxide, cobalt oxide, surface area measurement

INTRODUCTION

The oxygen evolution reaction (OER) is the kinetic bottleneck in the electrochemical and photoelectrochemical splitting of water into hydrogen and oxygen. The increasing demand for energy has intensified the search for active, earth-abundant catalysts for the oxygen evolution reaction. Cobalt hydroxide, $Co(OH)_2$,[1] cobalt oxyhydroxide, CoOOH,[2,3] and cobalt oxide, Co_3O_4,[4-10] are materials known to show electrocatalytic activity for the OER. Although the Co oxidation state of the above materials is either Co(II) or Co(III), it is believed that the active species participating in the OER is CoO_2, *i.e.* Co(IV).[11,12]

$Co(OH)_2$ can be prepared by various base precipitation methods[13,14] and can also be deposited electrochemically by localized cathodic electrogeneration of OH^- via the

reduction of nitrate ions, as demonstrated by other groups.[15-18] In recent work, we introduced another electrochemical route for depositing $Co(OH)_2$ by reducing tris(ethylenediamine)cobalt(III) in alkaline solution.[1] Electrodeposition offers low cost and high tunability. Compared with other synthetic routes for $Co(OH)_2$, our method utilizes direct electrodeposition of the crystalline material, which results in better adhesion of the films and provides the possibility to grow them epitaxially. $Co(OH)_2$ can then be converted to CoOOH by electrochemical oxidation[2,19] and to Co_3O_4 by thermal decomposition.[20-22] Here, we show a scheme for the synthesis of $Co(OH)_2$, CoOOH and Co_3O_4 films with a microcone morphology. We also compare the OER catalytic activities of those films in alkaline solution.

EXPERIMENTAL

Film synthesis and conversion. The $Co(OH)_2$ deposition method was the same as in our previous work except that a lower concentration of the $Co(en)_3^{3+}$ was used here. Briefly, the deposition solution containing 10 mM $Co(en)_3^{3+}$ and 2 M NaOH was stirred at 200 rpm with a magnetic stir bar. The three-electrode set up consisted of Au-coated glass as the working electrode, Au mesh as the counter electrode, and $Ag/AgCl/KCl_{sat.}$ as the reference electrode. The deposition was performed by applying -1 $V_{Ag/AgCl}$ at the working electrode to a charge density of 0.5 C cm^{-2} using a Brinkman PGSTAT 30 Autolab potentiostat. The same deposition was also done on stainless steel (SS430) and Ti substrates for the comparison of the morphology. To fully oxidize the $Co(OH)_2$ film to CoOOH, the potential was scanned between the open circuit potential (OCP) *ca*. -0.2 $V_{Ag/AgCl}$ to 0.2 $V_{Ag/AgCl}$ at 1 mV s^{-1} scan rate for 5 cycles in a 95^{o}C 1 M KOH solution

stirred at 200 rpm. Thermal decomposition of the films to Co_3O_4 was done by annealing the films at 300^oC for 2 hours in air.

OER studies. Linear sweep voltammetry (LSV) was done in an O_2 saturated 1 M KOH solution stirred at 200 rpm, and an O_2 atmosphere was maintained throughout the experiments. The three-electrode set up involved a Pt mesh counter electrode, an $Ag/AgCl/KCl_{sat.}$ reference electrode and the modified Au-coated glass substrate as the working electrode. The potential sweep rate of 1 mV s^{-1} was controlled by the Autolab potentiostat. The Tafel plot was constructed using the LSV data. The reported overpotential was calculated to reflect the thermodynamic potential of oxygen evolution at pH 14 and was corrected for the IR drop in the solution. The solution resistance, R, was measured by electrochemical impedance spectroscopy on the Autolab potentiostat.

Surface area measurement. The surface area of the Au-coated glass was determined from the reduction of the surface oxide on Au by performing three cycles of cyclic voltammetry (CV) in a 0.1 M H_2SO_4 solution at 20 mV s^{-1} from -0.6 to 1.5 $V_{Ag/AgCl}$. The cathodic peak from the third cycle was integrated and converted to the surface area using a literature reported conversion factor.[39]

The surface areas of the films were estimated by double layer capacitance measurements in an acetonitrile solution containing 0.1 M tetrabutylammonium hexafluorophosphate. We assume that the double layer capacitance is determined solely by the electrode area, and is not a function of the electrode material. A specific capacitance of 8 μF cm^{-2} was assumed for the area estimations. A series of CVs were performed across ±20 mV of the OCP at 50, 100, 150, 200, 250, 300 and 400 mV s^{-1} scan

rates. The anodic current densities at the OCP were plotted against the scan rates. The slope of this plot was recorded as the double layer capacitance of the film.

Characterization. The structures of the films were probed through a high-resolution Philips X-Pert MRD X-ray diffractometer (XRD) with a $CuK\alpha_1$ radiation source (λ = 1.54056 Å). The morphology of the films was revealed by a Hitachi S4700 field emission scanning electron microscope (SEM). Raman measurements were obtained with a Horiba Jobin-Yvon LabRam Aramis Microscope with a HeNe laser (λ = 633 nm) excitation source. To reduce sample heating, the incident power was reduced to about 1 mW.

RESULTS AND DISCUSSION

$Co(OH)_2$ film deposition, morphology and surface reaction. The heart of our $Co(OH)_2$ deposition method rests on the well-known inorganic chemistry that Co(III) favors nitrogen ligands, whereas Co(II) favors oxygen ligands. The formation constant of $[Co(en)_3]^{3+}$ is $10^{48.69}$, which is nearly 35 orders of magnitude larger than the formation constant of $10^{13.94}$ of $[Co(en)_3]^{2+}$.[23] In an aqueous environment, Co(III) complexes are substitutionally inert, whereas Co(II) complexes are substitutionally labile.[24] While $[Co(en)_3]^{3+}$ is stable in an alkaline solution, the less stable $[Co(en)_3]^{2+}$ species generated at the cathode reacts with excess OH^- to produce $Co(OH)_2$. The formation constant of $Co(OH)_2$ is $10^{14.96}$.[25] The electrochemical-chemical reaction scheme used to produce $Co(OH)_2$ is shown in equations 1 and 2 below.

$$[Co(en)_3]^{3+} + e^- \rightleftharpoons [Co(en)_3]^{2+} \quad (1)$$

$$[Co(en)_3]^{2+} + 2OH^- \rightarrow Co(OH)_2 \downarrow + 3en \quad (2)$$

The microcone morphology of the electrodeposited $Co(OH)_2$ crystals is observed on several substrates including Au-coated glass, stainless steel (SS430) and Ti, as shown in Figure 1. It is also apparent that the microcones grow in a preferred orientation, with the flat side facing up, on the Au-coated glass (Figure 1a) which naturally exhibits a strong [111] orientation. Hence, the microcones have a disk-like appearance when viewed from the top. Randomly oriented microcones grow on the SS and Ti substrates, as seen in Figures 1b and c.

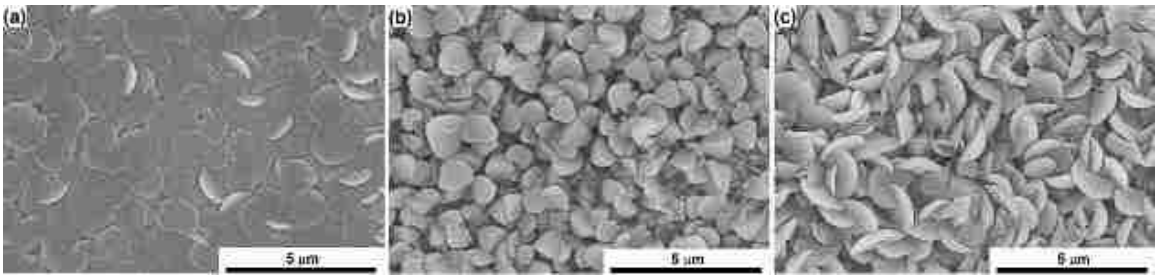

Figure 1. SEM images of as-deposited $Co(OH)_2$ films on (a) Au-coated glass, (b) stainless steel and (c) Ti substrates

The as-deposited $Co(OH)_2$ film is subjected to CV from the OCP of about -0.1 V to +0.55 V vs Ag/AgCl at 1 mV s^{-1} rate for five cycles in an O_2 saturated 1 M KOH as shown in Figure 2. The anodic peak A_1 is attributed to oxidation of Co(II) to Co(III), and A_2 is assigned to oxidation of Co(III) to Co(IV).[26] That is, the surface of the $Co(OH)_2$ film is converted to CoOOH and CoO_2 during the anodic scan of the CV, because CoOOH and CoO_2 are the thermodynamically stable species under oxidizing conditions.[27]

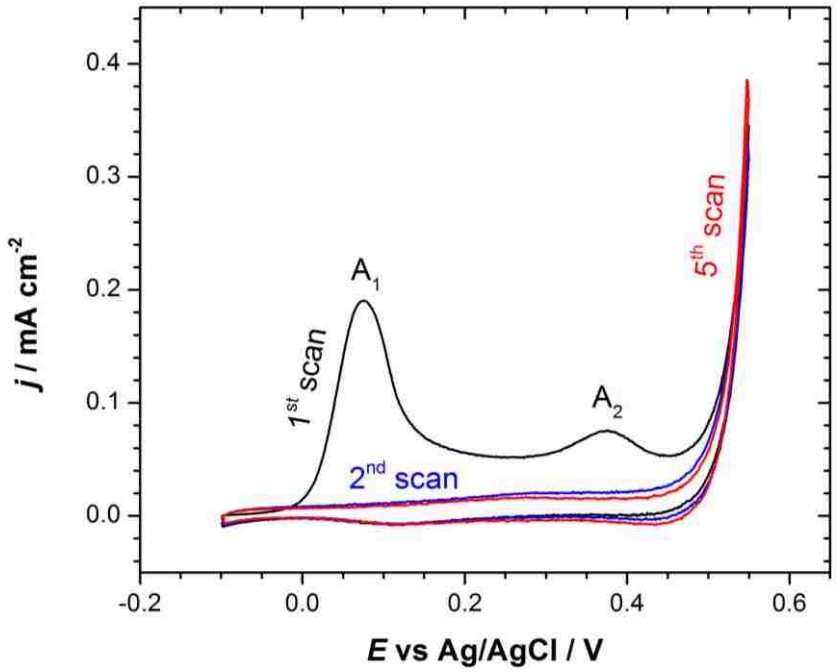

Figure 2. Cyclic voltammetry of the as-deposited $Co(OH)_2$ film at 1 mV s^{-1} scan rate in an O_2 saturated 1 M KOH at room temperature

Film conversion and characterization. $Co(OH)_2$ is a gateway material for conversion to CoOOH and Co_3O_4. CoOOH can be derived from the $Co(OH)_2$ precursor by calcination at modest temperatures,[22] by hydrothermal oxidation,[28] or by electrochemical oxidation.[2,19] Thermal decomposition is a common method for Co_3O_4 synthesis, whether from $Co(OH)_2$ precursors,[20-22] from CoOOH[22] or from other suitable salts of cobalt such as $Co(NO_3)_2$.[10,29] Here, an easy-to-follow scheme of the conversion platform is displayed in Scheme 1. The $Co(OH)_2$ film is synthesized as described above. It is converted to CoOOH by performing CV across the A_1 peak (in Figure 2), from OCP to 0.2 $V_{Ag/AgCl}$, in a 95^{o}C solution of 1 M KOH. Five cycles of the CV at 1 mV s^{-1} are sufficient to fully convert the film. The completion of the conversion is confirmed by the disappearance of the Co(II) to Co(III) peak in the fifth scan of the CV, as well as by XRD

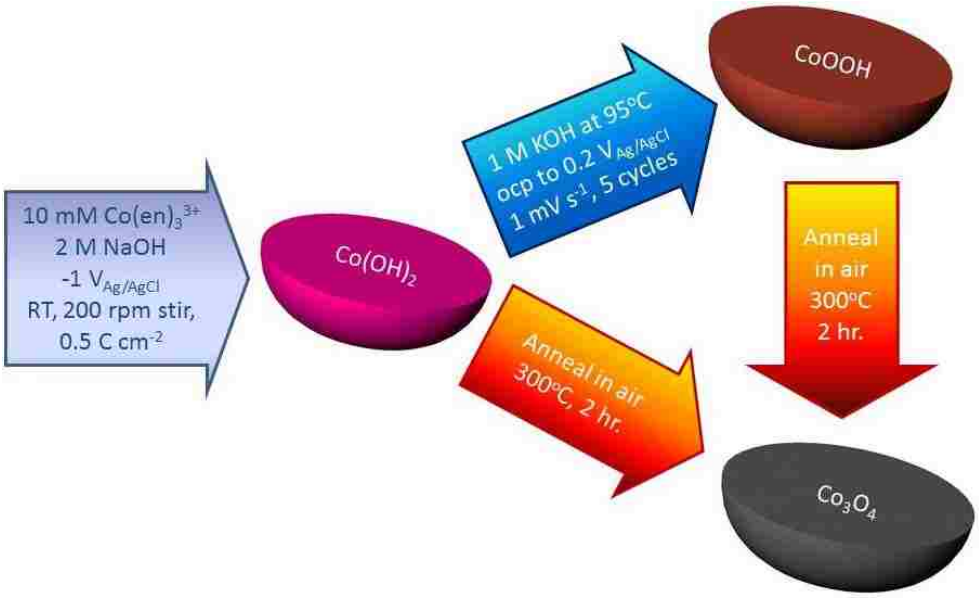

Scheme 1. Scheme for $Co(OH)_2$ deposition and the conversion to CoOOH and Co_3O_4 microcones

analysis. Conversion to Co_3O_4 is achieved by simply annealing either $Co(OH)_2$ or CoOOH at 300°C for 2 hours in air. The identities of the converted films are verified by X-ray diffraction (XRD) analysis with grazing incidence beam as shown in Figure 3. The peaks are indexed according to JCPDS no. 30-0443 and 01-074-1057 for $Co(OH)_2$, no. 01-073-0497 for CoOOH, and no. 42-1467 for Co_3O_4. The symmetric scan of the XRD reveals the preferred orientation of the crystalline films as shown in Figure 4. The $Co(OH)_2$ and CoOOH grow with a [001] preferred orientation, whereas Co_3O_4 shows a [111] preferred orientation. The orientation of the films is determined by the [111] orientation of the sputter-deposited Au. This opens up the possibility of growing epitaxial $Co(OH)_2$ films on single-crystal substrates and converting them to epitaxial CoOOH and Co_3O_4 films. Thus, the catalytic activities on different exposed lattice planes could be studied.

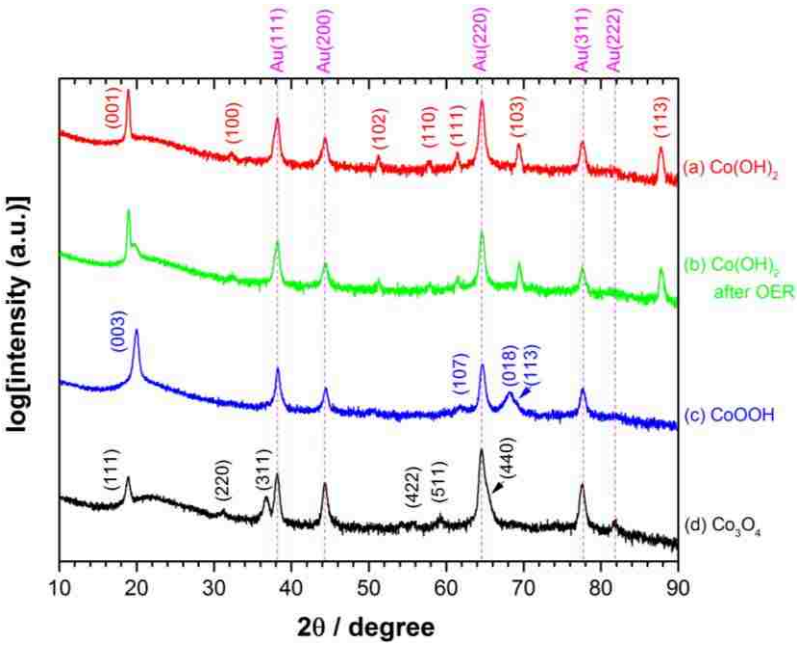

Figure 3. XRD pattern measured with a grazing incidence beam showing the identity of (a) $Co(OH)_2$, (b) $Co(OH)_2$ after OER studies, (c) CoOOH and (d) Co_3O_4.

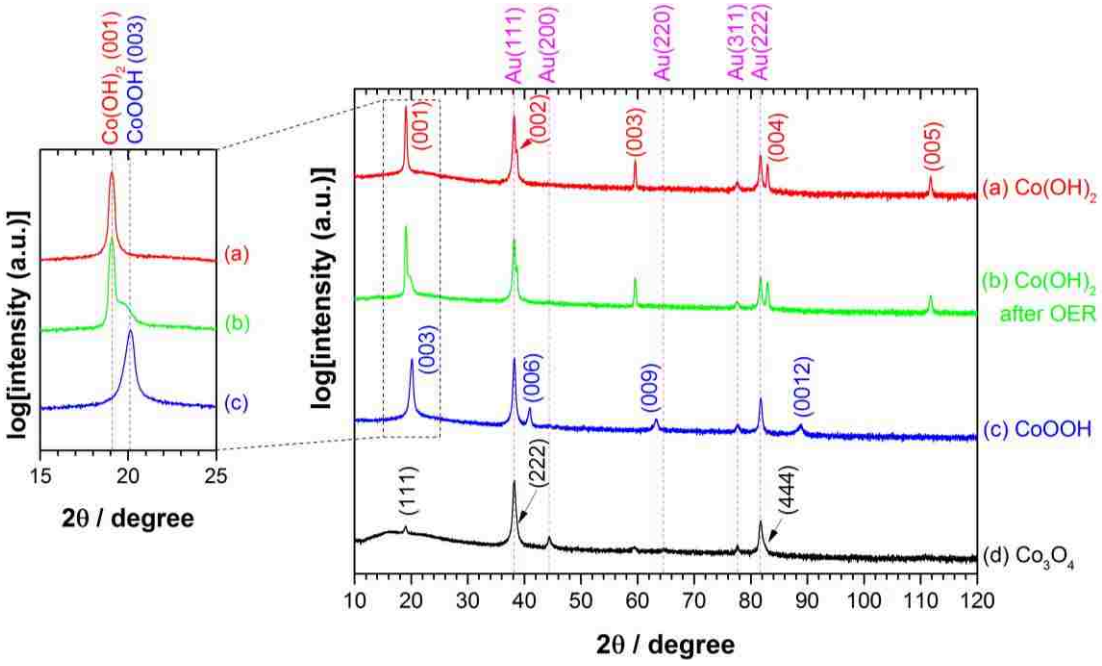

Figure 4. Symmetric scan of the XRD pattern showing the preferred crystal orientation of (a) $Co(OH)_2$, (b) $Co(OH)_2$ after OER studies, (c) CoOOH and (d) Co_3O_4. The zoom-in view emphasizes the convoluted peak of (b) due to surface oxidation to CoOOH.

The films are also characterized by Raman spectra as shown in Figure 5. The peak positions match that of the literature values for $Co(OH)_2$,[1,30] CoOOH[1,31,32] and Co_3O_4.[33-35] It is evident from the Raman spectra that the $Co(OH)_2$ film after OER studies (Figure 5b) shows what resembled the spectrum of the fully oxidized CoOOH film. However, the XRD of the $Co(OH)_2$ after OER showed that the majority of the film was still $Co(OH)_2$ with a convoluted peak reflecting the surface CoOOH species, as shown in the zoomed-in view of Figure 4.

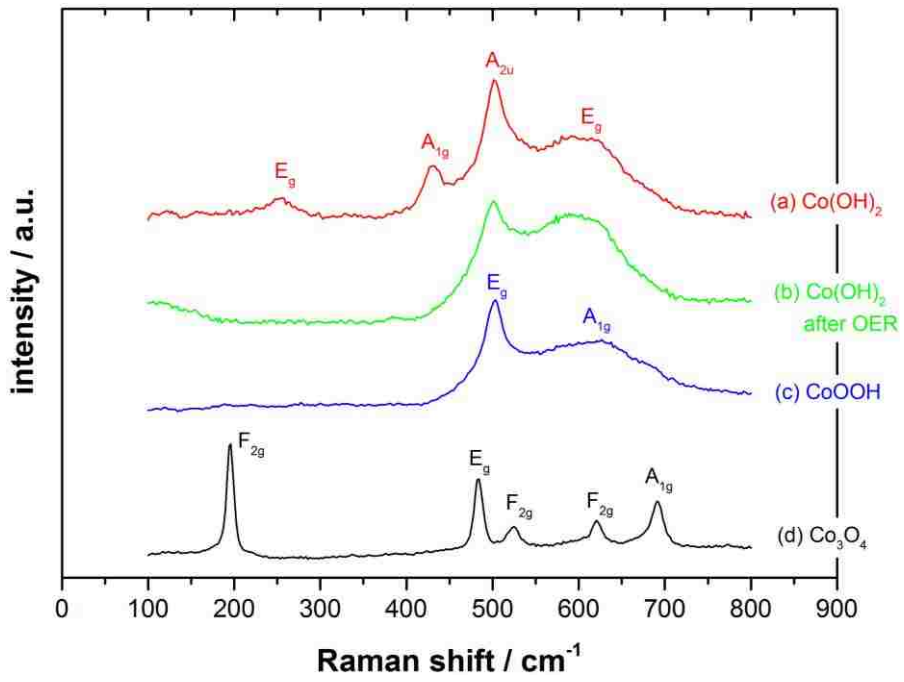

Figure 5. Raman spectra of (a) $Co(OH)_2$, (b) $Co(OH)_2$ after OER studies, (c) CoOOH and (d) Co_3O_4.

Surface area measurement. The surface area of an Au substrate can be estimated from the charge under the AuO cathodic peak as described in the literature.[36-38]

For the 1.00 cm^2 geometric area of the Au-coated glass substrate used later for the deposition of the films, we first perform two cycles of CV at 20 mV s^{-1} in a 0.1 M H_2SO_4 soultion. The integrated area of the AuO reduction peak from the second CV is 505 μC, and we use the conversion factor of 482 μC cm^{-2} [38,39] to derive our calculated surface area of 1.05 cm^2. Since the geometric area of the substrate is 1.00 cm^2, we assign a roughness factor of 1.05 to the Au-coated glass substrate.

The use of the double layer capacitance measurement for determining the electrochemically active surface area was described by Trasatti and Petrii in their early work.[36] However, due to the large pseudo capacitance caused by cation intercalation into the oxide,[11,36,40] this method is not be feasible in an aqueous solution. Instead, we perform the double layer capacitance measurements in an acetonitrile solution containing 0.1 M tetrabutylammonium hexafluorophosphate, as demonstrated in our previous work.[33] Using this method, we find that the specific capacitances of metal substrates, such as Au and Pt, and oxide substrates, such as indium-tin oxide (ITO) and fluorine-tin oxide (FTO), all fall in the tight range of 8-13 μF cm^{-2}. Thus, we assume that the double layer capacitance is determined solely by the electrode area because of the large cation in our measurements, and is not a function of the electrode material. CVs of ±20 mV across the OCP are scanned at 50, 100, 150, 200, 250, 300 and 400 mV s^{-1} as shown in Figure 6a and b, and the anodic current densities at OCP for each scan is plotted against the scan rates as shown in Figure 6c. The slopes from such a plot provide the double layer capacitances, C_d, of the substrate and the films. The roughness factors can then be calculated by taking the C_d ratio between the film and the substrate and multiplying by the substrate roughness factor. For example, the CoOOH film shows 72 μF cm^{-2} whereas

the substrate shows 8 μF cm^{-2}. The roughness factor of CoOOH is 72 μF cm^{-2} / 8 μF cm^{-2} × 1.05 = 9.45. The results are tabulated in Table 1. Note that the as-deposited $Co(OH)_2$ has a low apparent C_d, presumably due to its resistive nature. That is, the capacitance measurements may be probing the area of exposed Au rather than the $Co(OH)_2$ area. The film after OER experiments becomes more conductive due to the surface CoOOH species and therefore shows higher C_d. Another possibility for the low value of calculated area for $Co(OH)_2$ is that the specific capacitance of $Co(OH)_2$ is smaller than the assumed value of 8 μF cm^{-2}.

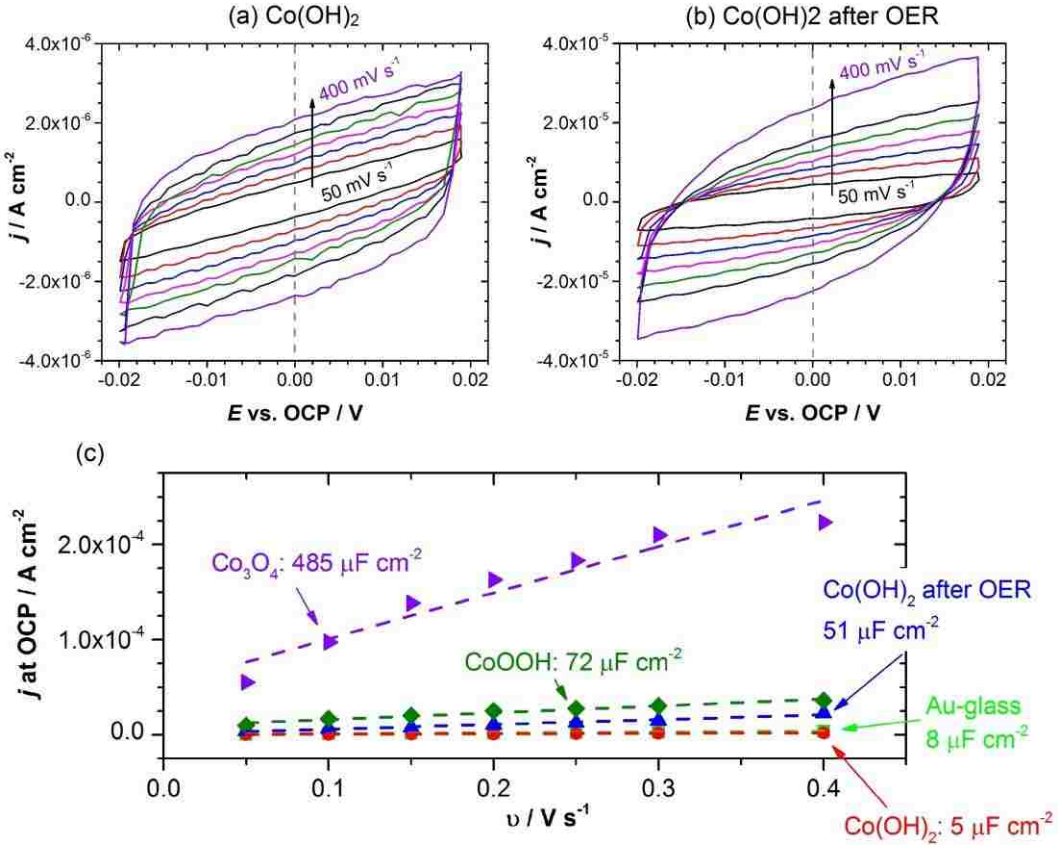

Figure 6. Double layer capacitance measurements on (a) $Co(OH)_2$ film and (b) $Co(OH)_2$ after OER. The slope of current density at OCP vs. scan rate plot shown in (c) is the double layer capacitance of the film or the substrate.

Table 1. Measured double layer capacitance (C_d) and the calculated roughness factors of the substrate and the films

Material	C_d / μFcm^{-2}	Roughness Factor
Au-coated glass	8	1.05
$Co(OH)_2$	5	0.63
$Co(OH)_2$ after OER	51	6.72
CoOOH	72	9.45
Co_3O_4	485	63.6

Change in surface area. Upon conversion of the films, the gross morphology of the crystals is retained. Figure 7a, b and c show the microcone features on $Co(OH)_2$, CoOOH and Co_3O_4, respectively, under a scanning electron microscope (SEM).

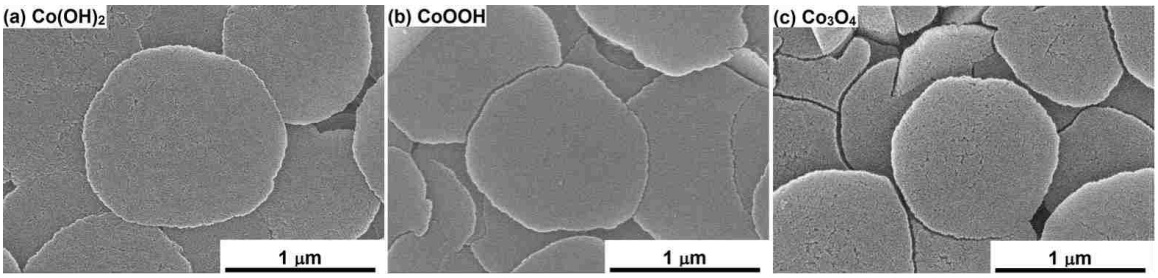

Figure 7. SEM images of (a) as-deposited $Co(OH)_2$, (b) CoOOH and (c) Co_3O_4

However, the surface becomes rougher after each conversion, as evident from the SEM images and the measured surface area (Table 1). The change in the surface area can be explained by the volume shrinkage of the crystal structure. Lou *et al*. have shown that

single crystal nano-needles of $Co(OH)_2$ are converted into porous nano-needles of Co_3O_4 when $Co(OH)_2$ is thermally converted to Co_3O_4.[21] Table 2 summarizes the structural properties of the three materials. It is important to note that although the unit cell volume increases from $Co(OH)_2$ to CoOOH and to Co_3O_4, the unit cell volume per Co atom decreases upon the conversion because there is only 1 Co atom in a $Co(OH)_2$ unit cell, whereas there are 3 in CoOOH, and 24 in Co_3O_4 unit cells. The volume shrinkage is 24.5 % from $Co(OH)_2$ to CoOOH and 28.6 % from CoOOH to Co_3O_4. The large volume shrinkage causes the crystals to crack or to develop pores.[21] Because the roughness factor of Co_3O_4 is 63.6, the conversion method outlined in Scheme 1 provides a means to produce Co_3O_4 with a relatively high surface area.

Table 2. Structural properties of $Co(OH)_2$, CoOOH and Co_3O_4

		$Co(OH)_2$	CoOOH	Co_3O_4
Space group		$P\bar{3}m1$	$R\bar{3}m$	$Fd\bar{3}m$
Lattice parameters	a (nm)	0.3183	0.2851	0.8084
	b (nm)	0.3183	0.2851	0.8084
	c (nm)	0.4652	1.315	0.8084
	α (^{o})	90	90	90
	β (^{o})	90	90	90
	γ (^{o})	120	120	90
Unit cell volume	(nm^3)	0.04082	0.09257	0.52824
# Co / unit cell		1	3	24
Unit cell volume / Co (nm^3)		0.04082	0.03086	0.02201

Catalytic activity for OER. The catalytic behavior of the CoOOH and Co_3O_4 films are studied by LSV and Tafel analysis in an O_2 saturated 1 M KOH at room temperature. As shown in Figure 8, Co_3O_4 appears to be a better catalyst than CoOOH owing to the earlier onset and higher OER current density when calculated based on the

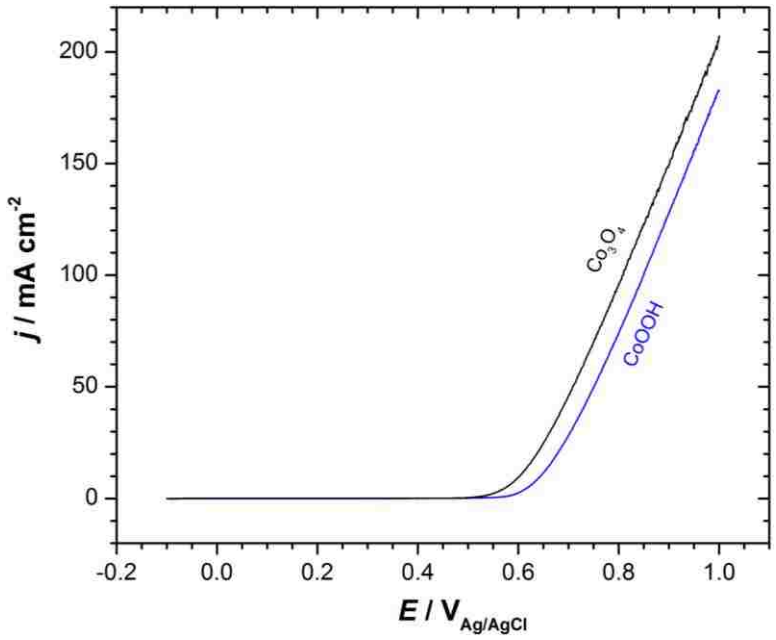

Figure 8. LSV of the CoOOH and Co_3O_4 films at 1 mV s^{-1} scan rate in an O_2 saturated 1 M KOH at room temperature. The solution was stirred at 200 rpm with a magnetic stir bar and the current density was calculated based on the geometric area of the substrate

geometric area of the substrates. The Tafel plot, constructed directly from the LSV data, is corrected for the solution resistance (~3 ohm) and is shown in Figure 9. Co_3O_4 has a Tafel slope of 61 mV dec^{-1} and an exchange current density, j_0, of 6.0 × 10^{-9} A cm^{-2}. CoOOH on the other hand shows a 54 mV dec^{-1} Tafel slope and j_0 of 1.2 ×10^{-10} A cm^{-2}. Both materials have Tafel slopes in the 60 mV dec^{-1} range, implying that the reaction

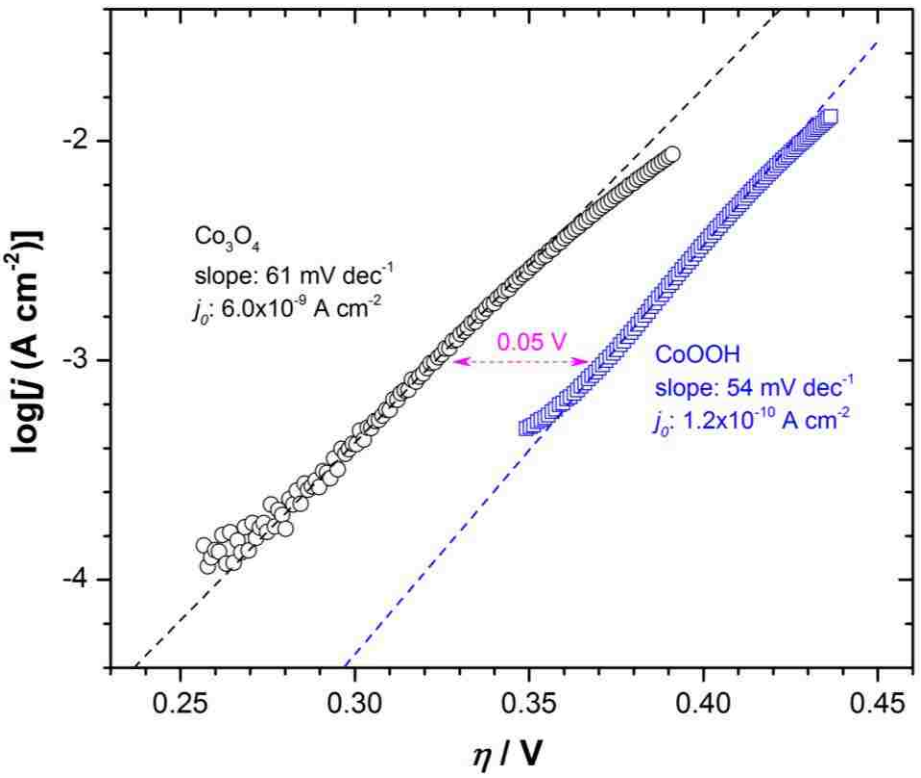

Figure 9. Tafel plot of the CoOOH and Co_3O_4 films. It is constructed from the data in Figure 8 with the overpotential, η, corrected for the IR drop in the solution. The current density was calculated using the geometric area of the substrate

mechanisms of the catalytic behavior are similar. Yet, the exchange current densities suggest that Co_3O_4 is 50 times more active than CoOOH. However, if the current densities are corrected based on the measured electrochemically active surface, then the two Tafel plots fall on the same line with the slope of 60 mV dec^{-1} and j_0 of 6.1×10^{-11} A cm^{-2} as shown in Figure 10. This result suggests that both materials have the same active species, likely Co(IV), for OER, which is in agreement with several other studies.[11,12,41] The Tafel slopes at about 60 mV dec^{-1} suggests that the first electron transfer step, associated with the adsorption of OH^-, is followed by a subsequent chemical step – the recombination of the surface OH species – involved in the rate-determining reaction.[2,42,43]

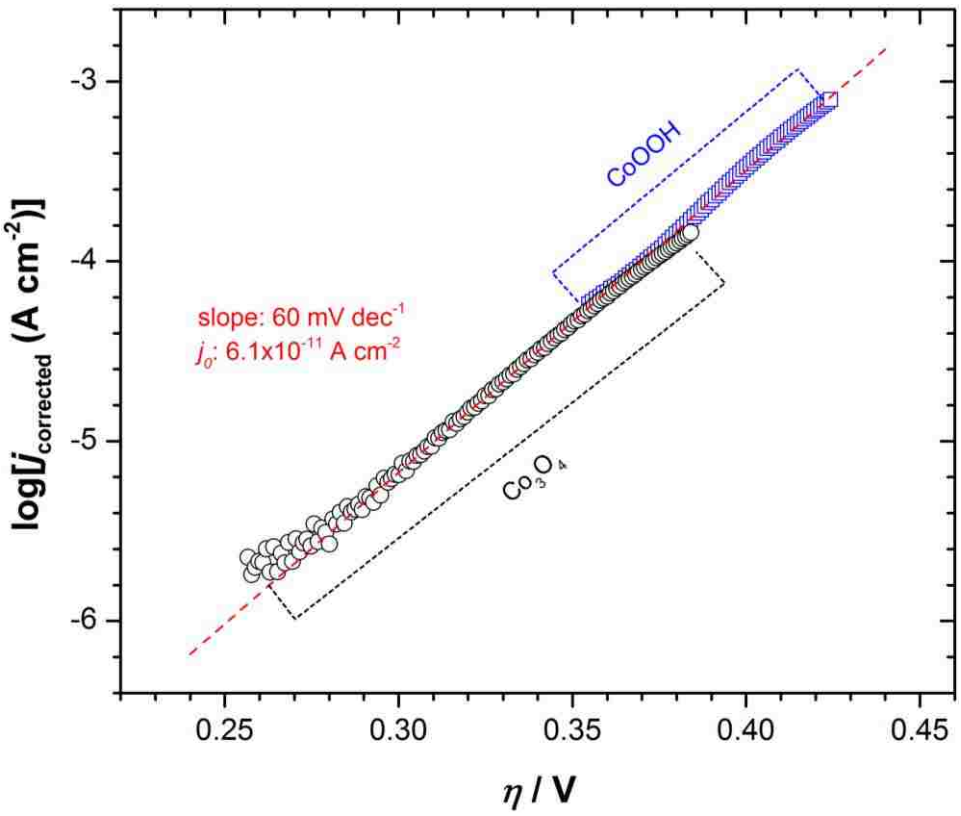

Figure 10. Tafel plot of the CoOOH and Co_3O_4 films with the current density corrected based on the measured surface area estimated from the double-layer capacitance

ACKNOWLEDGEMENT

The work was supported by the U.S. Department Of Energy, Office of Basic Sciences under Grant No. DE-FG02-08ER46518.

The authors thank Dr. Eric Bohannan for assistance in the XRD measurements.

AUTHOR INFORMATION

*Corresponding author. Tel.: +1 573 341 4383; E-mail address: jswitzer@mst.edu

REFERENCES

1. Koza, J. A.; Hull, C. M.; Liu, Y.-C.; Switzer, J. A.: Deposition of β-$Co(OH)_2$ Films by Electrochemical Reduction of Tris(ethylenediamine)cobalt(III) in Alkaline Solution. *Chem. Mater.* **2013**, *25*, 1922-1926.

2. Subbaraman, R.; Tripkovic, D.; Chang, K.-C.; Strmcnik, D.; Paulikas, A. P.; Hirunsit, P.; Chan, M.; Greeley, J.; Stamenkovic, V.; Markovic, N. M.: Trends in activity for the water electrolyzer reactions on 3d M(Ni,Co,Fe,Mn) hydro(oxy)oxide catalysts. *Nat. Mater.* **2012**, *11*, 550-557.

3. Garcia-Mota, M.; Bajdich, M.; Viswanathan, V.; Vojvodic, A.; Bell, A. T.; Noerskov, J. K.: Importance of Correlation in Determining Electrocatalytic Oxygen Evolution Activity on Cobalt Oxides. *J. Phys. Chem. C* **2012**, *116*, 21077-21082.

4. Iwakura, C.; Honji, A.; Tamura, H.: *Electrochim. Acta* **1981**, *26*, 1319.

5. Tseung, A. C. C.; Jasem, S.: *ibid.* **1977**, *22*, 31.

6. Trasatti, S.: *ibid.* **1984**, *29*, 1503.

7. Efremov, B. N.; Tarasevich, M. R.: *Elektrokhimiya* **1981**, *17*, 1672.

8. Tarasevich, M. R.; Efremov, B. N.: Properties of spinel-type oxide electrodes. *Stud. Phys. Theor. Chem.* **1980**, *11*, 221-259.

9. Esswein, A. J.; McMurdo, M. J.; Ross, P. N.; Bell, A. T.; Tilley, T. D.: Size-Dependent Activity of Co_3O_4 Nanoparticle Anodes for Alkaline Water Electrolysis. *J. Phys. Chem. C* **2009**, *113*, 15068-15072.

10. Trasatti, S.: Electrocatalysis in the anodic evolution of oxygen and chlorine. *Electrochim. Acta* **1984**, *29*, 1503-1512.

11. Boggio, R.; Carugati, A.; Trasatti, S.: Electrochemical surface properties of cobalt oxide (Co_3O_4) electrodes. *J. Appl. Electrochem.* **1987**, *17*, 828-840.

12. Lyons, M. E. G.; Brandon, M. P.: A comparative study of the oxygen evolution reaction on oxidized nickel, cobalt and iron electrodes in base. *J. Electroanal. Chem.* **2010**, *641*, 119-130.

13. Zeng, H. C.; Xu, Z. P.; Qian, M.: Synthesis of Non-Al-Containing Hydrotalcite-like Compound Mg0.3CoII0.6CoIII0.2(OH)2(NO3)0.2·H2O. *Chem. Mater.* **1998**, *10*, 2277-2283.

14. Hou, Y.; Kondoh, H.; Shimojo, M.; Kogure, T.; Ohta, T.: High-Yield Preparation of Uniform Cobalt Hydroxide and Oxide Nanoplatelets and Their Characterization. *J. Phys. Chem. B* **2005**, *109*, 19094-19098.

15. Brownson, J. R. S.; Levy-Clement, C.: Nanostructured α- and β-cobalt hydroxide thin films. *Electrochim. Acta* **2009**, *54*, 6637-6644.

16. Zhou, W.-j.; Zhang, J.; Xue, T.; Zhao, D.-d.; Li, H.-l.: Electrodeposition of ordered mesoporous cobalt hydroxide film from lyotropic liquid crystal media for electrochemical capacitors. *J. Mater. Chem.* **2008**, *18*, 905-910.

17. Yarger, M. S.; Steinmiller, E. M. P.; Choi, K.-S.: Electrochemical synthesis of cobalt hydroxide films with tunable interlayer spacings. *Chem. Commun. (Cambridge, U. K.)* **2007**, 159-161.

18. Wu, J.; Zhang, D.; Wang, Y.; Wan, Y.; Hou, B.: Catalytic activity of graphene-cobalt hydroxide composite for oxygen reduction reaction in alkaline media. *J. Power Sources* **2012**, *198*, 122-126.

19. Pralong, V.; Delahaye-Vidal, A.; Beaudoin, B.; Leriche, J. B.; Tarascon, J. M.: Electrochemical behavior of cobalt hydroxide used as additive in the nickel hydroxide electrode. *J. Electrochem. Soc.* **2000**, *147*, 1306-1313.

20. Hu, L.; Peng, Q.; Li, Y.: Selective Synthesis of Co_3O_4 Nanocrystal with Different Shape and Crystal Plane Effect on Catalytic Property for Methane Combustion. *J. Am. Chem. Soc.* **2008**, *130*, 16136-16137.

21. Lou, X. W.; Deng, D.; Lee, J. Y.; Archer, L. A.: Thermal formation of mesoporous single-crystal Co_3O_4 nano-needles and their lithium storage properties. *J. Mater. Chem.* **2008**, *18*, 4397-4401.

22. Xu, Z. P.; Zeng, H. C.: Thermal evolution of cobalt hydroxides: a comparative study of their various structural phases. *J. Mater. Chem.* **1998**, *8*, 2499-2506.

23. *Lange's Handbook of Chemistry*; 15 ed.; McGraw-Hill, Inc.: New York, 1999.

24. Marusak, R. A.; Doan, K.; Cummings, S. D. *Integrated Approach to Coordination Chemistry: An Inorganic Laboratory Guide*; John Wiley & Sons, Inc: Hoboken, NJ, 2007.

25. *CRC Handbook of Chemistry and Physics*; 74 ed.; CRC Press, Inc.: Boca Raton, LA, 1994.

26. Chang, J.-K.; Wu, C.-M.; Sun, I. W.: Nano-architectured $Co(OH)_2$ electrodes constructed using an easily-manipulated electrochemical protocol for high-performance energy storage applications. *J. Mater. Chem.* **2010**, *20*, 3729-3735.

27. Chen, J.; Selloni, A.: First Principles Study of Cobalt (Hydr)oxides under Electrochemical Conditions. *J. Phys. Chem. C* **2013**, *117*, 20002-20006.

28. Yang, J.; Liu, H.; Martens, W. N.; Frost, R. L.: Synthesis and Characterization of Cobalt Hydroxide, Cobalt Oxyhydroxide, and Cobalt Oxide Nanodiscs. *J. Phys. Chem. C* **2010**, *114*, 111-119.

29. Wendt, H.; Hofmann, H.; Plzak, V.: Materials research and development of electrocatalysts for alkaline water electrolysis. *Mater. Chem. Phys.* **1989**, *22*, 27-49.

30. Shieh, S. R.; Duffy, T. S.: Raman spectroscopy of $Co(OH)_2$ at high pressures: implications for amorphization and hydrogen repulsion. *Phys. Rev. B Condens. Matter Mater. Phys.* **2002**, *66*, 134301/134301-134301/134308.

31. Ludvigsson, M.; Lindgren, J.; Tegenfeldt, J.: Incorporation and characterization of oxides of manganese, cobalt and lithium into Nafion 117 membranes. *J. Mater. Chem.* **2001**, *11*, 1269-1276.

32. Pauporte, T.; Mendoza, L.; Cassir, M.; Bernard, M. C.; Chivot, J.: Direct low-temperature deposition of crystallized CoOOH films by potentiostatic electrolysis. *J. Electrochem. Soc.* **2005**, *152*, C49-C53.

33. Koza, J. A.; He, Z.; Miller, A. S.; Switzer, J. A.: Electrodeposition of Crystalline Co_3O_4-A Catalyst for the Oxygen Evolution Reaction. *Chem. Mater.* **2012**, *24*, 3567-3573.

34. Khadzhiev, V.; Iliev, M.; Vergilov, I.: The Raman spectra of cobalt oxide (Co_3O_4). *J. Phys. C Solid State Phys.* **1988**, *21*, L199-L201.

35. Wang, G.; Shen, X.; Horvat, J.; Wang, B.; Liu, H.; Wexler, D.; Yao, J.: Hydrothermal Synthesis and Optical, Magnetic, and Supercapacitance Properties of Nanoporous Cobalt Oxide Nanorods. *J. Phys. Chem. C* **2009**, *113*, 4357-4361.

36. Trasatti, S.; Petrii, O. A.: Real surface area measurements in electrochemistry. *Pure Appl. Chem.* **1991**, *63*, 711-734.

37. Hoogvliet, J. C.; Dijksma, M.; Kamp, B.; Van Bennekom, W. P.: Electrochemical pretreatment of polycrystalline gold electrodes to produce a reproducible surface roughness for self-assembly. A study in phosphate buffer pH 7.4. *Anal. Chem.* **2000**, *72*, 2016-2021.

38. Oesch, U.; Janata, J.: Electrochemical study of gold electrodes with anodic oxide films. I. Formation and reduction behavior of anodic oxides on gold. *Electrochim. Acta* **1983**, *28*, 1237-1246.

39. Marsh, D. A.; Yan, W.; Liu, Y.; Hemminger, J. C.; Penner, R. M.; Borovik, A. S.: Water Oxidation Using a Cobalt Monolayer Prepared by Underpotential Deposition. *Langmuir* **2013**, *29*, 14728-14732.

40. Minguzzi, A.; Fan, F.-R. F.; Vertova, A.; Rondinini, S.; Bard, A. J.: Dynamic potential-pH diagrams application to electrocatalysts for water oxidation. *Chem. Sci.* **2012**, *3*, 217-229.

41. Gerken, J. B.; McAlpin, J. G.; Chen, J. Y. C.; Rigsby, M. L.; Casey, W. H.; Britt, R. D.; Stahl, S. S.: Electrochemical Water Oxidation with Cobalt-Based Electrocatalysts from pH 0-14: The Thermodynamic Basis for Catalyst Structure, Stability, and Activity. *J. Am. Chem. Soc.* **2011**, *133*, 14431-14442.

42. Doyle, R. L.; Godwin, I. J.; Brandon, M. P.; Lyons, M. E. G.: Redox and electrochemical water splitting catalytic properties of hydrated metal oxide modified electrodes. *Phys. Chem. Chem. Phys.* **2013**, *15*, 13737-13783.

43. Dau, H.; Limberg, C.; Reier, T.; Risch, M.; Roggan, S.; Strasser, P.: The Mechanism of Water Oxidation: from Electrolysis via Homogeneous to Biological Catalysis. *ChemCatChem* **2010**, *2*, 724-761.

III. NANOMETER-THICK GOLD ON SILICON AS A PROXY FOR SINGLE-CRYSTAL GOLD FOR THE ELECTRODEPOSITION OF EPITAXIAL CUPROUS OXIDE THIN FILMS

Jay A. Switzer,[†,*] *James C. Hill,*[†,§] *Naveen K. Mahenderkar,*[‡] *and Ying-Chau Liu*[†]

[†]Department of Chemistry and Graduate Center for Materials Research, Missouri University of Science and Technology, Rolla, Missouri 65409-1170, United States, and

[‡]Department of Materials Science and Engineering and Graduate Center for Materials Research, Missouri University of Science and Technology, Rolla, Missouri 65409-1170, United States.

ABSTRACT

Single-crystal Au is an excellent substrate for electrochemical epitaxial growth due to its chemical inertness, but the high cost of bulk Au single-crystals prohibits their use in practical applications. Here, we show that ultrathin epitaxial films of Au electrodeposited onto Si(111), Si(100), and Si(110) wafers can serve as an inexpensive proxy for bulk single-crystal Au for the deposition of epitaxial films of cuprous oxide (Cu_2O). The Au films range in thickness from 7.7 nm for a film deposited for 5 minutes to 28.3 nm for a film deposited for 30 minutes. The film thicknesses are measured by low-angle X-ray reflectivity and X-ray Laue oscillations. High-resolution TEM shows that there is not an interfacial SiO_x layer between the Si and Au. The Au films deposited

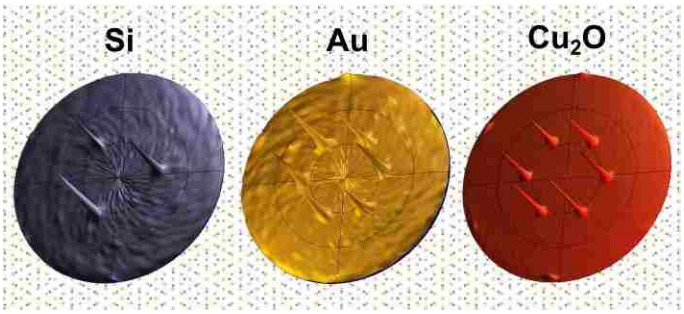

on the Si(111) substrates are smoother and have lower mosaic spread than those deposited onto Si(100) and Si(110). The mosaic spread of the Au(111) layer on Si(111) is only 0.15^{o} for a 28.3 nm thick film. Au films deposited onto degenerate Si(111) exhibit ohmic behavior, whereas Au films deposited onto n-type Si(111) with a resistivity of 1.15 Ω-cm are rectifying with a barrier height of 0.85 eV. The Au and the Cu_2O follow the out-of-plane and in-plane orientations of the Si substrates, as determined by X-ray pole figures. The Au and Cu_2O films deposited on Si(100) and Si(110) are both twinned. The films grown on Si(100) have twins with a [221] orientation, and the films grown on Si(110) have twins with a [411] orientation. An interface model is proposed for all Si orientations, in which the -24.9% mismatch for the Au/Si system is reduced to only +0.13% by a coincident site lattice in which 4 unit meshes of Au coincide with 3 unit meshes of Si. Although this study only considers the deposition of epitaxial Cu_2O films on electrodeposited Au/Si, the thin Au films should serve as high-quality substrates for the deposition of a wide variety of epitaxial materials.

KEYWORDS

Electrodeposition, epitaxy, thin films, gold, cuprous oxide, silicon, coincident site lattice

INTRODUCTION

Gold metal electrodes are a preeminent choice for electrochemical studies due to their chemical inertness. Single-crystal Au has also been used extensively as a substrate for the electrodeposition of thin layers of metals by underpotential deposition (UPD),[1-3] and as a substrate for epitaxial growth of semiconductors.[4-8] Our group has been involved

with the epitaxial electrodeposition of thin films and superlattices of metal oxide ceramics for several years. We define epitaxy as the growth of crystalline films on an ordered substrate in which the out-of-plane and in-plane orientation of the film is controlled by the substrate. Epitaxial films can provide superior electronic or optical properties because of the low number of grain boundaries that can act as defects or electron-hole recombination sites. Although some work has been done in our lab on single-crystal Si[9] and InP[10-12] substrates, the majority of our epitaxial films have been electrodeposited onto single-crystal Au. Examples of epitaxial ceramic films that we have electrodeposited on Au include δ-Bi_2O_3,[13,14] Cu_2O,[15-17] ZnO,[18,19] Fe_3O_4,[20-24] CuO,[25,26] SnS,[27] $CoFe_2O_4$,[28] Mn_3O_4,[29] Co_3O_4,[30] and methylammonim lead iodide perovskites.[31] We have also electrodeposited ceramic superlattices based on PbO_2/Tl_2O_3[32-35] and $Fe_3O_4/ZnFe_2O_4$[23,28] onto single-crystal Au. Although single-crystal Au does provide a platform for studies of the basic science behind epitaxial electrodeposition, there is little probability that these epitaxial systems will be technologically exploited, due to the very high cost and small size (about 1 cm^2) of Au single crystals. Hence, an inexpensive alternative to Au single crystals is needed.

Researchers have used vapor-deposited Au layers on glass and mica as a proxy for single-crystal gold for the deposition of self-assembled monolayers.[36] However, the Au layers on glass are only [111]-oriented out-of-plane with no in-plane order, and the Au layers on mica have deep grooves between the [111]-oriented crystals. The Au on mica samples have large enough grains for scanning probe microscopy studies, but they do not have long-range, in-plane order that extends across the entire sample. Researchers have also produced epitaxial Au nanostructures on Si(111) and Si(100) substrates by

galvanic displacement, in which the Si substrate acts as a reducing agent to deposit the epitaxial Au.[37] Although the Au nanostructures produced by galvanic displacement do follow the orientation of the Si substrates, the Au islands grow by the Volmer-Weber mechanism. This method, therefore, does not produce smooth Au films that mimic the surface of single-crystal Au substrates.

Allongue and co-workers pioneered an electrochemical method to grow thin, ultraflat Au(111) epitaxial buffer layers on hydrogen-terminated Si(111).[38,39] Although metal films typically grow three-dimensionally on Si, and there is typically an SiO_x interlayer, the Allongue group showed that Au deposited at large negative potentials (c.a., -2 V vs. the mercury sulfate electrode) at which there was concomitant evolution of hydrogen gas were very smooth, epitaxial, and did not have an interfacial SiO_x layer. They deposited the Au onto 0.2^o miscut Si(111) oriented towards $[11\bar{2}]$ with a long-range staircase structure. The goal of their work was to produce ultrathin layers of non-magnetic substrates for the epitaxial growth of ultrathin magnetic metals, in order to probe the effects of thickness on the magnetic properties of the metals.[40,41]

Here, we show that nanometer-thick electrodeposited epitaxial layers of Au on Si(111), Si(100), and Si(110) can serve as a proxy for bulk single-crystal Au for the electrodeposition of epitaxial thin films of cuprous oxide (Cu_2O). Although this paper focuses on the deposition of Cu_2O on Au/Si, the epitaxial Au/Si substrates will provide a platform for the deposition of a wide variety of epitaxial ceramic and semiconductor thin films. The highly-ordered Au/Si substrates can be synthesized at a small fraction of the cost of bulk Au single crystals because of the low mass (i.e., micrograms) of Au that is used, they can conceivably be made as large as a Si wafer, and they may allow for the

integration of electrodeposited functional ceramics with traditional semiconductor devices. In addition, the Au/Si interface is an interesting example of epitaxy, because high-quality, smooth Au epitaxial films are produced even though there is a -24.9% lattice mismatch between the Au film and Si substrate.

RESULTS AND DISCUSSION

Ultra-thin films of Au were electrodeposited onto Si(111), Si(100), and Si(110) substrates using the method developed by Allongue and co-workers for the deposition of Au onto Si(111). [38,39] The deposition was performed on wafers with n-type doping, and on degenerately-doped wafers. The n-Si(111) was miscut 0.2° towards [11$\bar{2}$] with a resistivity of 1.15 Ω-cm, the n^{++}-Si(100) had a resistivity of 0.001 Ω-cm, and the p^{++}-Si(110) had a resistivity of 0.005 Ω-cm. The miscut Si(111) will hereafter be referred to simply as Si(111). The deposition was done at room temperature in a solution containing 0.1 mM $HAuCl_4$, 1 mM KCl, 1 mM H_2SO_4 and 0.1 M K_2SO_4 using a Si electrode that was pre-polarized at -1.9 V vs. Ag/AgCl before inserting it in the deposition solution. X-ray diffraction (XRD) patterns of films that were deposited for 30 minutes onto Si(111), Si(100), and Si(110) are shown in Figure 1. The XRD patterns show that the Au follows the out-of-plane orientation of the Si for all three orientations. The Au peaks are broader than the Si peaks primarily because of the nanoscale thickness (i.e., short X-ray coherence length) of the Au films.

The Au thickness on the Si wafers can be measured by X-ray diffraction. Constructive and destructive interference of X-rays that are reflected from the Au-air and Si-Au interfaces manifests itself as interference fringes in low-angle X-ray reflectivity

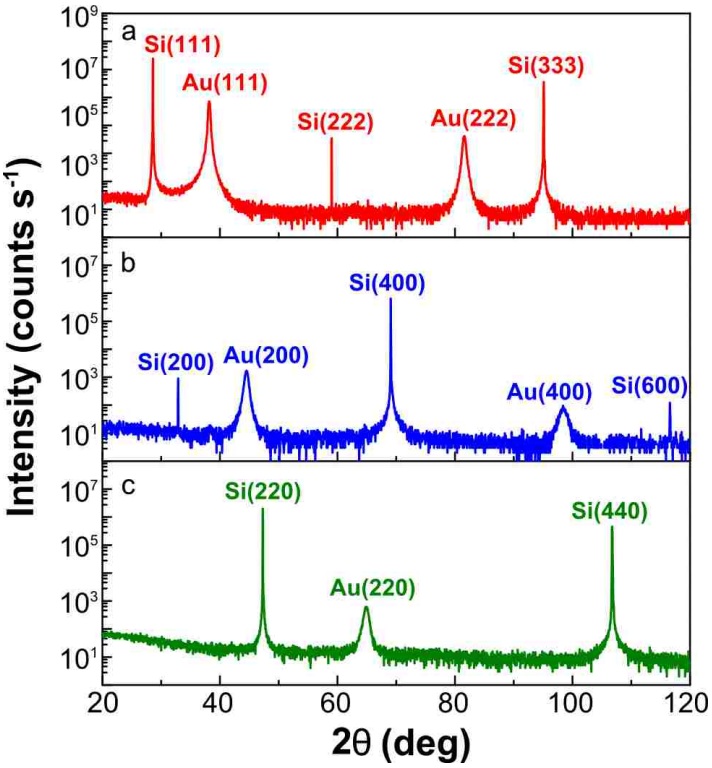

Figure 1. X-ray diffraction patterns of Au on Si. Out-of-plane orientation of electrodeposited (a) Au(111) on Si(111), (b) Au(100) on Si(100) and (c) Au(110) on Si(110).

(Kiessig fringes)[42,43] and as satellites flanking the Bragg peaks at higher angles (Laue oscillations).[23,28] These fringes and satellites are only observed for very smooth, nanometer-thick films. In our work, they were observed for films deposited onto Si(111), but not for films deposited onto Si(100) or Si(110). Kiessig fringes in the low-angle X-ray reflectivity are shown in Figure 2a for an Au film that was deposited for 30 minutes onto n-Si(111) with a resistivity of 1.15 Ω-cm. The Kiessig fringes can be used to calculate the Au film thickness and density from Equations 1 and 2,

$$\sin^2\theta_i = (n_i + \Delta n)^2\left(\frac{\lambda}{2t}\right)^2 + \sin^2\theta_c \quad (1)$$

$$\rho = \left(\frac{\theta_c^2 \pi A}{N_A r_e \lambda^2 f}\right) \quad (2)$$

where θ_i is the Kiessig fringe angle, n_i is the fringe order of the minima, $n_i + \Delta n$ is the fringe order of the maxima (with $\Delta n = ½$), λ is the X-ray wavelength (0.15418 nm), t is the film thickness, θ_c is the critical angle, ρ is the film density (g cm^{-3}), N_A is Avogadro's number (6.023×10^{23}), r_c is the radius of the electron (2.818×10^{-13} cm), f is the atomic scattering factor for Au (79), and A is the atomic mass for Au (196.97 g mol^{-1}).[42,43] Figure 2b shows a plot of $\sin^2\theta_i$ versus $(n + \Delta n)^2$ for the reflectivity data from Figure 2a. Fringe maxima are denoted as closed circles, whereas fringe minima are denoted as open circles. The slope of the plot ($(\lambda/2t)^2$) gives a film thickness of 28.6±0.1 nm, and the intercept ($\sin^2\theta_c$) gives a critical angle of 0.56°. The density of the film calculated from Equation 2 is 18.6 g cm^{-3}. Because the bulk density of Au is 19.31 g cm^{-3}, this measurement shows that the electrodeposited Au is 96.3% dense. Laue oscillations around the Au(111) peak are shown in Figure 2c for the same Au film. The film thickness can be determined from the satellite positions in the XRD pattern using Equation 3,

$$t = \left(\frac{(L_1 - L_2)\lambda}{2(\sin\theta_1 - \sin\theta_2)}\right) \quad (3)$$

where t is the film thickness, L is the satellite peak order, λ is the X-ray wavelength, and θ is the satellite angle.[23,28] This is the same equation that is used to calculate modulation wavelengths in epitaxial superlattices.[23,28] The plot of $\sin\theta_1 - \sin\theta_2$ versus L_1-L_2 shown in Figure 2d gives a thickness of 28.3±0.1 nm, in excellent agreement with the low-angle reflectivity data. Figure 2e shows a plot of Au thickness measured by the Laue oscillations as a function of deposition time. The Au thickness ranges from 7.7 nm for a film deposited for 5 minutes to 28.3 nm for a film deposited for 30 minutes. It is

noteworthy that a 1 cm^2 electrode deposited with the thickest (28.3 nm) of these Au films contains only 54 μg of Au. Hence, the Au/Si substrate is a very inexpensive proxy for single-crystal Au. Figure 2f shows a cross-sectional transmission electron micrograph (TEM) of the Au film that was deposited for 30 minutes followed by the deposition of a Cu_2O film. The measured film thickness for the Au was 25±2 nm, in reasonable agreement with the more-accurate X-ray measurements. Also, the TEM measurements did not show an interfacial SiO_x layer between the Si(111) and Au(111).

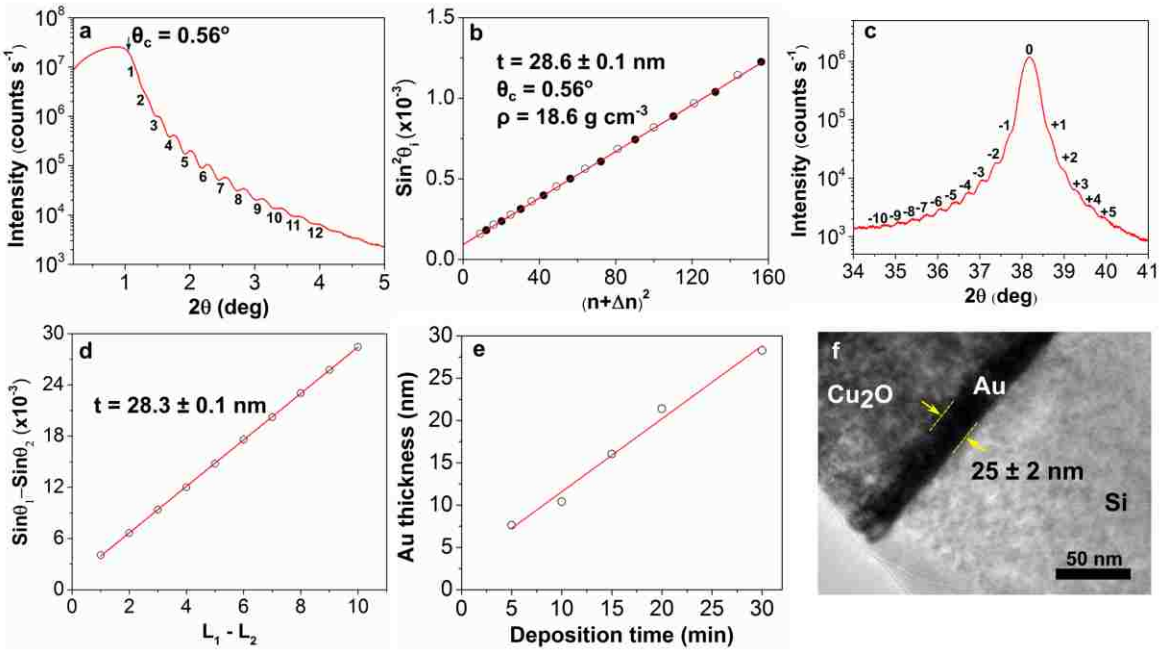

Figure 2. Thickness measurement of Au(111) on Si(111) by X-ray reflectivity, Laue oscillations, and TEM. (a) Low-angle X-ray reflectivity for a 30 minute Au(111) on Si(111) deposit showing air-Au and Au-Si interference fringes (Kiessig fringes). (b) Plot of $\sin^2\theta_i$ versus $(n + \Delta n)^2$ for the reflectivity data from (a) using equation 1. (c) Out-of-plane X-ray diffraction showing satellite peaks (Laue oscillations) corresponding to the X-ray coherence length of Au on Si. (d) Plot of $\sin\theta_1 – \sin\theta_2$ versus L_1-L_2 for the Laue oscillations from (c) using equation 3. (e) Plot of Au thickness measured by the Laue oscillations as a function of deposition time. (f) TEM cross-section of Cu_2O/Au/Si layers with Au thickness of 25±2 nm in close agreement with X-ray measurements.

Plan-view scanning electron micrograph (SEM) images of 28 nm thick Au films grown on Si(111), Si(100), and Si(110) are shown in Figure 3. The images are consistent with the X-ray results, because the Au(111) surface is very smooth and featureless (except for 16 nm pores), whereas the Au(100) and Au(110) surfaces are rough. This explains why the Kiessig fringes and Laue oscillations are only observed for the Au(111) films on Si(111).

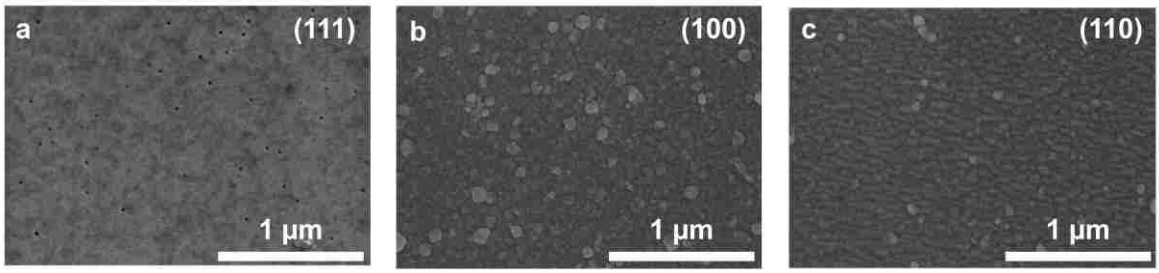

Figure 3. Surface morphology of the epitaxial Au films on Si. Plan-view SEM images of (a) Au(111), (b) Au(100) and (c) Au(110) films. The films are all approximately 28 nm thick. The Au(111) is smooth and featureless, whereas the Au(100) and Au(110) films are rough. The scale bar is 1 µm

The Au/Si junction can have ohmic or rectifying behavior, depending on the doping type and concentration in the Si wafer. If the Si is doped to degeneracy, the Au/Si functions as an ohmic contact, whereas if the Si is n-doped to moderate doping densities, the Au/Si functions as a Schottky barrier. Figure 4a shows the ohmic response that is observed when 28 nm of Au are deposited onto n^{++}-Si(111) with a resistivity of 0.05 Ω-cm. The same behavior is observed with p^{++}-Si substrates. In both cases the Si acts like a metal because the Fermi level is situated either in the conduction band (n^{++}-Si) or in

the valence band (p^{++}-Si) of the semiconductor. Degenerate Si substrates would be preferred if the Au/Si substrate were to be used for anodic depositions, or if precise control of the potential at the Au surface is required. As shown in Figure 4b, rectifying behavior is observed for 28 nm of Au deposited onto n-Si(111) with a resistivity of 1.15 Ω-cm. The Au/Si Schottky junction passes cathodic currents, but is blocking to anodic currents. This type of junction could be used for cathodic deposition of materials, but materials requiring anodic currents for deposition would require photo-assisted deposition. The interfacial energetics of the Au/Si Schottky barrier were determined by analysis of the current-voltage curves (Figure 4c) and by Mott-Schottky analysis (Figure 4d).[44] Figure 4c shows a plot of log(J) versus V in the forward bias regime. The slope of the plot gives a diode quality factor of 1.4, and the y-intercept gives a dark saturation current density of 2.5×10^{-8} A cm^{-2}, which corresponds to a barrier height of 0.85 eV. The Mott-Schottky plot of C^{-2} versus reverse bias gives the doping density in the depletion region of 3.8×10^{15} cm^{-3} from the slope of the line, and a flat band voltage of -0.68 V from the x-intercept. This flat band voltage corresponds to a barrier height of 0.90 eV, slightly larger than the 0.85 eV determined from the log(J) versus V plot. Mott-Schottky analysis often overestimates barrier heights, so we assume that the actual barrier height on the Au(111)/n-Si(111) is close to the 0.85 eV value determined from the forward bias current-voltage curve. It may be possible to exploit this relatively high barrier height in the Au(111)/n-Si(111) epitaxial junction to produce high photovoltage, stable photoanodes for photoelectrochemical cells.[44]

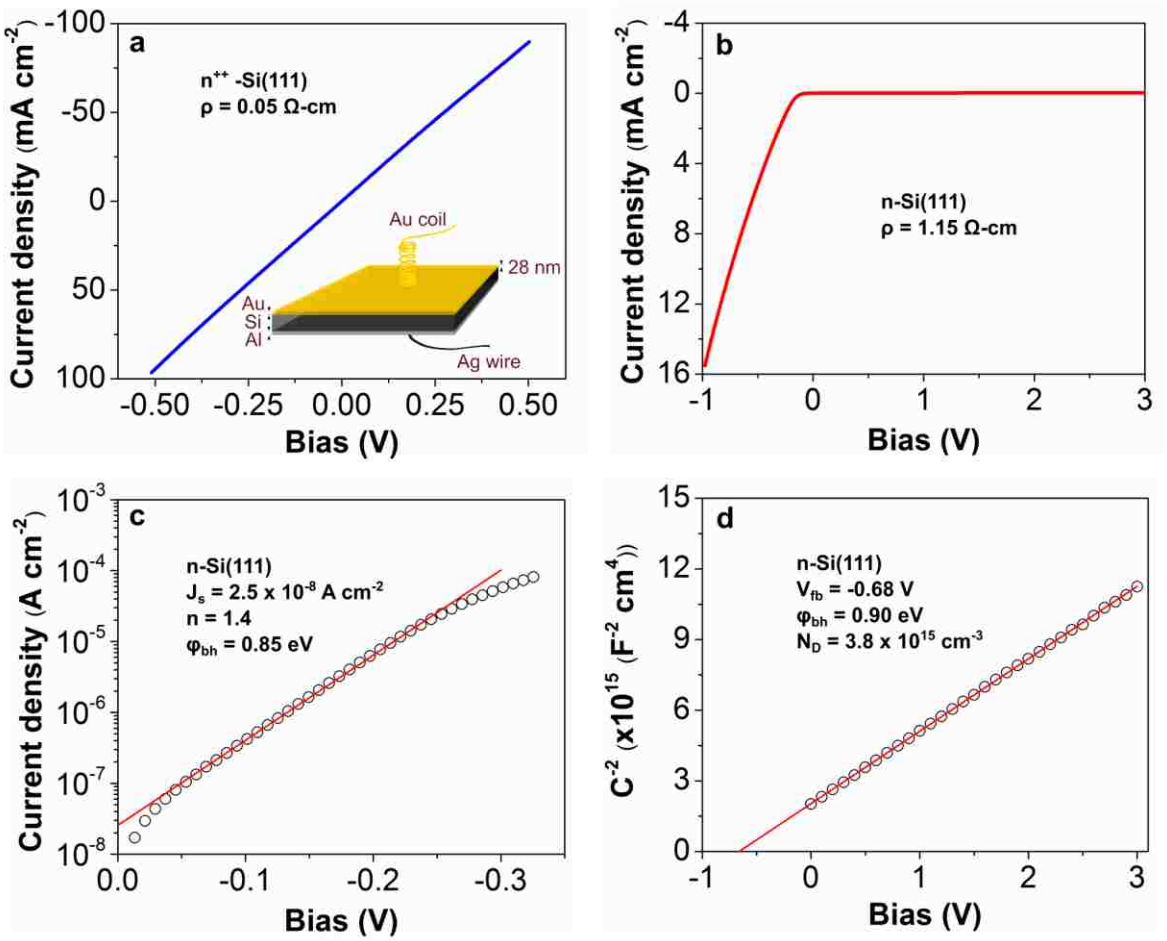

Figure 4. Junction characteristics of Au on Si(111). (a) Ohmic response of Au on n^{++}-Si(111) with a resistivity of 0.05 Ω-cm. Inset shows the schematic of measurement configuration with Au coil pressed against the Au layer as top contact and an aluminum sputtered back contact with a silver wire. (b) Current-voltage response of Au on n-Si(111) with resistivity of 1.15 Ω-cm showing rectifying behavior. (c) Short-circuit current density, diode quality factor and barrier height measured using log(J) vs. V at forward bias for Au on n-Si(111). (d) Flat-band voltage, doping density and barrier height measured using Mott-Schottky plot collected at 50 mV/s scan rate and 1 MHz frequency at reverse bias.

Cu_2O films were electrodeposited onto Si(111), Si(100), and Si(110) substrates covered with films of Au that were electrodeposited for 30 minutes. The deposition was performed from a solution containing 0.2 M $CuSO_4$, 0.2 M $C_4H_6O_6$ (tartaric acid), and

3.0 M NaOH at a constant cathodic current density of 1.0 mA cm^{-2} at 30 ^{o}C to a charge density of 0.1 C cm^{-2} (approximately 120 nm thick Cu_2O).[45] As shown in the XRD patterns in Figure 5, the Cu_2O followed the out-of-plane orientation of the Si substrates and the Au buffer layers for all three orientations of Si. Note that the log of intensity is plotted in the XRD patterns, so even minor orientations would be seen if they were present.

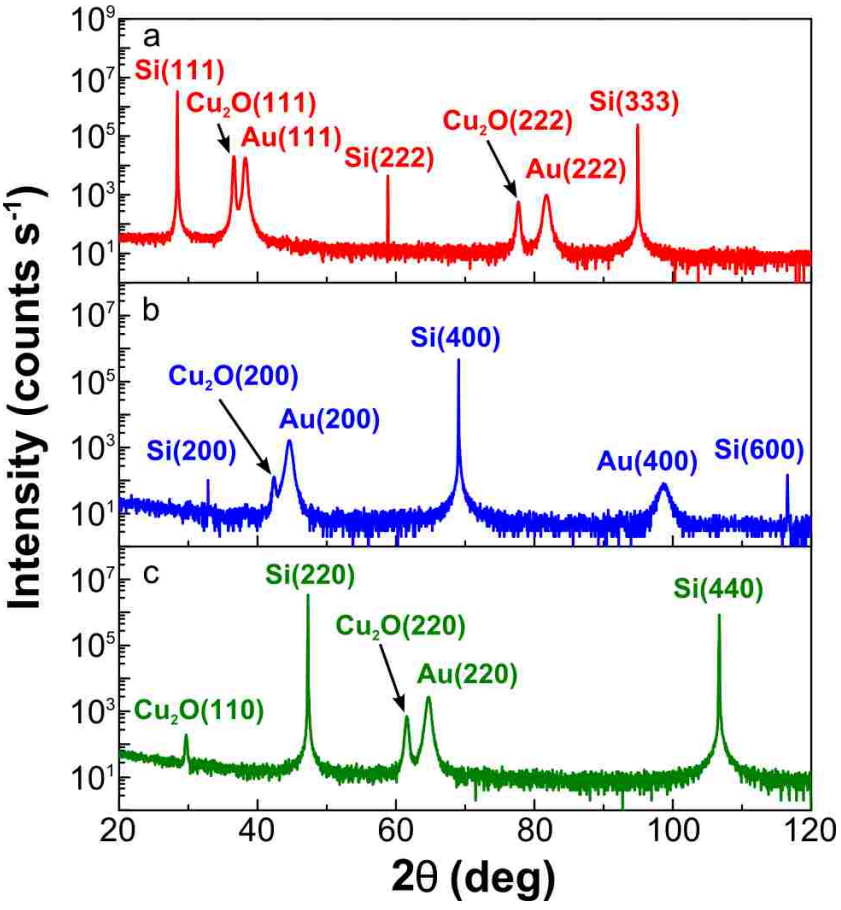

Figure 5. X-ray diffraction patterns of Cu_2O on Au on Si. Out-of-plane orientation of electrodeposited (a) Cu_2O(111) on Au(111)/Si(111), (b) Cu_2O(100) on Au(100)/Si(100) and (c) Cu_2O(110) on Au(110)/Si(110).

The out-of-plane perfection in the samples was also probed using X-ray rocking curves (Figure 6). The rocking angle, ω, is defined in Figure S1 of the Supporting Information. The rocking curves provide a direct measure of the mosaic spread (or distribution) of the films in the out-of-plane direction. The FWHM (full width at half maximum) of the rocking curves with a Gaussian distribution is equal to $2(2\ln 2)^{1/2}\alpha$, or $\sim 2.355\alpha$, where α is the standard deviation of the mosaic spread. Figure 6a shows rocking curves for Au films on Si(111) for various thicknesses of Au. It is seen that the rocking curve becomes sharper as the Au film thickness increases, and the curves develop a shape with a broad base and sharp peak for the thicker films. In Figure 6b the 28 nm Au film on Si(111) that was deposited for 30 minutes is deconvoluted into two Gaussian curves with FWHM of 0.15^{o} and 1.07^{o}. These results show that the mosaic spread of the Au on Si(111) decreases dramatically as the film thickness increases. Figure 6c compares the Au rocking curves on Si(111), Si(100), and Si(110). The Au on all three orientations of Si was electrodeposited for 30 minutes. The Au rocking curves on the Si(100) and Si(110) substrates do not show the two components that were observed on Si(111). The FWHM of the Au films on Si(111), Si(100), and Si(110) were 0.15^{o}, 2.03^{o}, and 1.29^{o}. Hence, the highest quality Au films are deposited on Si(111), and the quality of the film increases as the film thickness increases. Figure 6d shows rocking curves for 120 nm of Cu_2O that was deposited onto the three Au/Si orientations shown in Figure 6c. The FWHM of the Cu_2O rocking curves on Au(111)/Si(111), Au(100)/Si(100) and Au(110)/Si(110) was 1.15^{o}, 1.84^{o}, and 1.25^{o}, respectively. Again, the Cu_2O with the smallest mosaic spread is observed on Au(111)/Si(111).

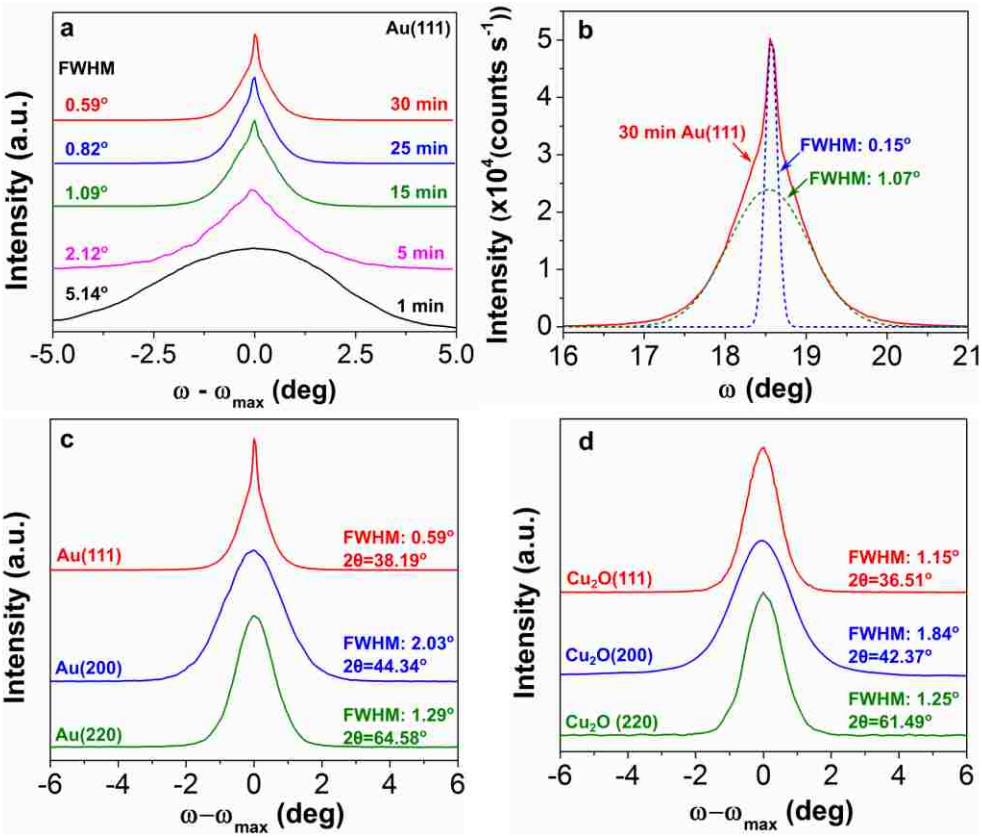

Figure 6. X-ray rocking curves of Au and Cu_2O on Si measure out-of-plane mosaic spread. (a) Rocking curves of Au on Si(111) as a function of deposition time. (b) Rocking curve of 30 minute Au on Si(111) deconvoluted into two Gaussian fits showing a mosaic spread of 0.15° and 1.07°. (c) Rocking curves of Au(111) on Si with FWHM of 0.59°, Au(100) with 2.03° and Au(110) with 1.29°. (d) Rocking curves of Cu_2O on Au/Si(111) with FWHM of 1.15°, Cu_2O(100) with 1.84° and Cu_2O(110) with 1.25°.

A high-resolution TEM micrograph is shown in Figure 7 for a 120 nm thick film of Cu_2O deposited onto a 25 nm thick Au buffer layer on miscut Si(111). The micrograph viewing direction is along the [11$\bar{2}$] zone axis. Figure 7a is a view showing all three materials, Figure 7b is a close-up of the Cu_2O(111)/Au(111) interface, and Figure 7c is a close-up of the Au(111)/Si(111) interface. A fairly sharp transition is seen at both interfaces. There are also no obvious dislocations or twins in the Au buffer layer. The

measured d-spacings for Au and Cu_2O are consistent with the bulk values. Most notable is the lack of an SiO_x interlayer at the Au(111)/Si(111) interface. We attribute this to the fact that the Si(111) electrode was pre-polarized at -1.9 V vs. Ag/AgCl before deposition of Au. Electron diffraction patterns of the Si and Au are shown in Figure S2 of the Supporting Information.

The out-of-plane and in-plane orientations of the Au buffer layer and Cu_2O film can be determined by X-ray pole figures. Because X-rays penetrate through the Au and Cu_2O layers and into the Si substrate, the pole figures can be used to determine the

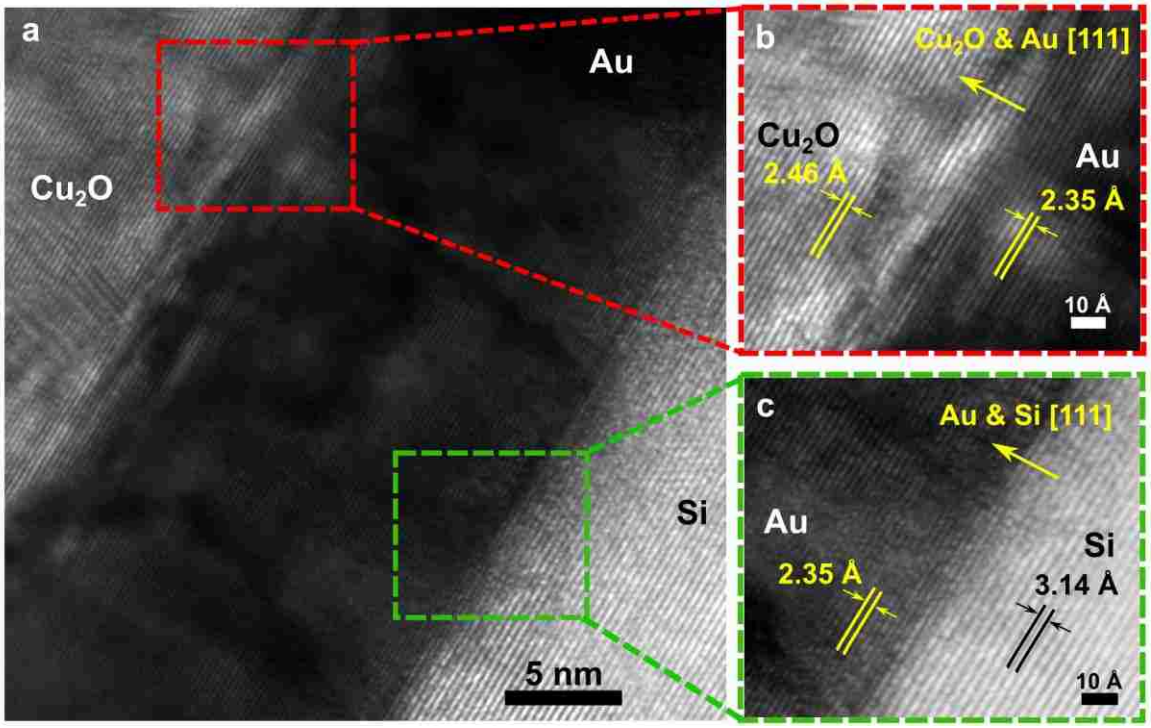

Figure 7. High-resolution cross-sectional TEM of Cu_2O(111) and Au(111) on Si(111). (a) TEM cross-section of Cu_2O(111)/Au(111)/Si(111) layers. (b) Cu_2O and Au high resolution TEM image with lattice spacings in agreement with bulk values and [111] growth direction is shown. (c) Au and Si high resolution TEM with lattice spacing in agreement with bulk values and no noticeable SiO_x interlayer.

epitaxial relationships of the film and buffer layer with respect to the Si substrate. In a pole figure, planes other than those parallel with the substrate surface are probed by selecting the Bragg angle, θ, for the plane of interest and then tilting the sample through a series of tilt angles, χ, from 0^o to 90^o and rotating the sample through a series of azimuthal angles, φ, from 0^o to 360^o. The measurement geometry for the pole figures is shown in Figure S1 of the Supporting Information. For films with in-plane order, peaks occur in the pole figure when the Bragg condition is satisfied, whereas for textured films with no in-plane order, rings are observed in the pole figure. X-ray pole figures of Si(111), Si(100), and Si(110) substrates with a 28 nm buffer layer of Au and a 120 nm film of Cu_2O are shown in Figure 8. In Figures 8a-c the (220) poles of Si(111), Au(111), and Cu_2O(111) are probed. The assignment of peaks in the pole figures was achieved by comparing the pole figures to calculated stereographic projections that are shown in Figure S3 of the Supporting Information. The Si pole figure in Figure 8a shows the expected 3 spots separated azimuthally by 120^o at a tilt angle of 35.5^o, consistent with the angle between the [111] and [220] directions in a cubic system. The (220) pole figures of the Au buffer layer and Cu_2O films shown in Figures 8b and 8c also show spots at the expected tilt angle of 35.5^o, however there are now six spots that are separated azimuthally by 60^o. These (220) pole figures show that the Si, Au, and Cu_2O all have a [111] out-of-plane orientation, and that the Au and Cu_2O are aligned in-plane both parallel and antiparallel with the Si substrate. The parallel and antiparallel in-plane orientations can also be described as rotation twins. Azimuthal and tilt scans of Cu_2O(111) on Au(111)/Si(111) are shown in Figure S4 of the Supporting Information. Epitaxial relationships consistent with these pole figures are $Cu_2O(111)[10\bar{1}]||$Au-

(111)[10$\bar{1}$]||Si(111)[10$\bar{1}$] and Cu_2O(111)[10$\bar{1}$]||Au(111)[10$\bar{1}$]||Si(111)[$\bar{1}$01]. In Figures 8d-f the (111) poles of Si(100) Au(100), and Cu_2O(100) are probed. All three pole figures show four spots separated azimuthally by 90^o at a tilt angle of 54.0^o consistent with the 54.74^o tilt between the [111] and [100] directions in a cubic system. The epitaxial relationship based on the major spots in the pole figures is Cu_2O(100)[011]||Au-(100)[011]||Si(100)[011]. In addition to the major spots at the expected tilt angle, however, there are also 4 spots at a tilt angle of 15.65^o and 8 spots at a tilt angle of 78.0^o. These additional spots are due to reflection twins with a [221] orientation.[21,46] That is, the [221] direction of the twinned crystallite is parallel to the [100] direction of the original crystallite. The (221) reflection is not observed in the 2θ plot in Figure 1b, because mixed-index reflections (i.e., even-even-odd) are systematically absent in an fcc structure. The higher-order (442) reflection should be observed, but it would occur at a 2θ value that exceeds our instrumental capability. Hence, the pole figure on the Si(100) sample shows both the epitaxial relationship, and it shows that the sample is twinned. A similar result is seen on Si(110). In Figures 8g-i the (111) poles of Si(110) Au(110), and Cu_2O(110) are probed. All three pole figures show two spots separated azimuthally by 180^o at a tilt angle of 34.5^o, consistent with the expected 35.26^o tilt between the [111] and [110] directions in a cubic system. The epitaxial relationship based on the major spots in the pole figures is Cu_2O(110)[001]||Au(110)[001]||Si(110)[001]. In addition to the major spots at the expected tilt angle, however, there are also 4 spots at a tilt angle of 57.0^o and 2 spots at a tilt angle of 75.0^o. These additional spots are due to reflection twins with a [411] orientation.[21,46] That is, the [411] direction of the twinned crystallite is parallel to the [110] direction of the original crystallite. The (411) reflection is also not observed in

the 2θ plot in Figure 1c, because it is a mixed-index reflection. Hence, the pole figures show that the Au buffer layers and Cu_2O films follow the out-of-plane and in-plane orientations of the Si(111), Si(100), and Si(110) substrates. In addition, the pole figures show that reflection twinning occurs in the samples on the Si(100) and Si(110) substrates but not on the Si(111) substrate. Reflection twinning on the Si(111) substrate would produce a [511] orientation,[21,46] which is not observed in the pole figures.

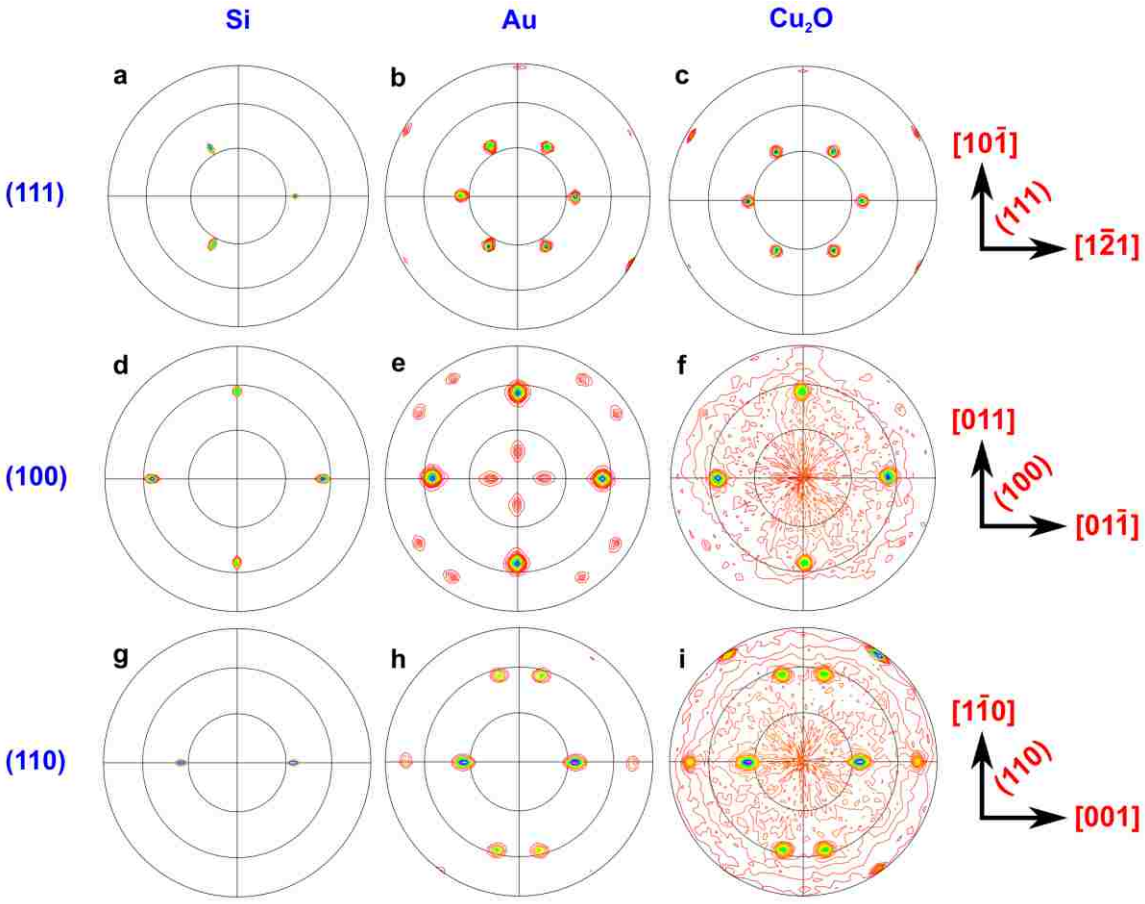

Figure 8. In-plane orientation of Au and Cu_2O on Si from X-ray pole figures. (a-c) (220) pole figures of Si(111), Au(111) and Cu_2O(111). (d-f) (111) pole figures of Si(100), Au(100) and Cu_2O(100) and (g-i) (111) pole figures of Si(110), Au(110) and Cu_2O(110). The radial grid lines in the pole figures represent 30^o increments of the tilt angle.

At this point, it is instructive to review the twinning relationships in a cubic system. Additional detail on the twinning transformation matrices is provided in the Supporting Information. Twinning can be described by the matrix, $T_{(hkl)}$, by the relationship

$$(PQR) = T_{(hkl)}(pqr) \tag{4}$$

where (PQR) is a column matrix for the lattice plane in a twinned crystallite that corresponds to the lattice plane, (pqr), of the original crystallite after twinning on (hkl). The general twin matrix for cubic systems is

$$T_{(hkl)} = \left(\frac{1}{h^2+k^2+l^2}\right)\begin{pmatrix} h^2-k^2-l^2 & 2hk & 2hl \\ 2hk & -h^2+k^2-l^2 & 2kl \\ 2hl & 2kl & -h^2-k^2+l^2 \end{pmatrix} \tag{5}$$

In face-centered cubic crystal structures, twinning occurs on {111} slip planes, and the twinning matrix becomes,

$$T_{(111)} = \left(\frac{1}{3}\right)\begin{pmatrix} -1 & 2 & 2 \\ 2 & -1 & 2 \\ 2 & 2 & -1 \end{pmatrix} \tag{6}$$

Hence, by using the twin matrix in Equation 6 and solving Equation 4, the twinning relationships shown in Equations 7-9 result.

$$(pqr) = (300); (PQR) = (\bar{1}22) \tag{7}$$

$$(pqr) = (330); (PQR) = (114) \tag{8}$$

$$(pqr) = (\bar{3}33); (PQR) = (5\bar{1}\bar{1}) \tag{9}$$

The pole figures in Figure 8 show that reflection twinning of Au occurs on the Si(100) and Si(110) substrates, but not on the Si(111) substrate. The pole figures also show that this twinning on Au(100) and Au(110) is transferred to the Cu_2O films on these buffer layers. This is especially obvious in the pole figure in Figure 8i for the Cu_2O films

deposited on Au(110) on Si(110). Hence, the twin orientation is present at the surface of the twinned Au films. There is not a simple explanation for why reflection twinning does not occur on the [111]-oriented substrate, whereas it does occur on the [100]- and [110]-oriented substrates, because the Au/Si lattice mismatch is the same on all three substrates. One possible explanation is that the [111] direction is both the thermodynamically and kinetically preferred growth direction for Au, because the (111) planes are the close-packed planes. This [111] orientation will develop even on polycrystalline or amorphous substrates. Hence, the Au films on the [100] and [110] substrates may be twinning as they slowly evolve into [111]-oriented films. As shown in the Supporting Information (Supporting Information, Figure S5), a thick (~5 μm) film of Au electrodeposited onto [110]-oriented Si does eventually develop a [111] orientation, consistent with this hypothesis.

The Cu_2O/Au/Si system is an interesting example of epitaxy. In this epitaxial system, Cu_2O with lattice parameter 0.42696 nm and primitive space group $Pn\bar{3}m$ is deposited onto Au with lattice parameter 0.40786 nm and fcc space group $Fm\bar{3}m$, which is deposited onto Si with lattice parameter 0.54309 nm and diamond cubic space group $Fd\bar{3}m$. The lattice mismatch $((d_{film}-d_{substrate})/d_{substrate})$ between Cu_2O and Au is +4.7% and the lattice mismatch between Au and Si is -24.9%. Because all of the materials have cubic structures and the Au and Cu_2O on a given Si substrate both have the same out-of-plane orientation as the substrate, the lattice mismatch is independent of the Si orientation. The +4.7% mismatch in the Cu_2O/Au system is reasonable, and would be expected to produce a Cu_2O layer with moderate compressive in-plane strain and tensile out-of-plane strain. Interface models for the Cu_2O/Au interfaces for the three orientations

are shown in Figure S6 of Supporting Information. The -24.9% mismatch in the Au/Si system is too excessive, however, to produce a simple 1x1 epitaxial system. The epitaxy in the Au/Si system can be explained by the formation of coincident site lattices (CSLs) in which 4 unit meshes of Au coincide with 3 unit meshes of Si. These CSLs are shown in Figure 9, in which the surface Si atoms are blue and the Au atoms are gold. The out-of-plane and in-plane directions in these CSLs were directly measured from the pole figures in Figure 8. The CSLs produce Moiré patterns on each of the Si surfaces. The lattice mismatch (i.e., $(4d_{Au(hkl)} - 3d_{Si(hkl)})/3d_{Si(hkl)}$) in the CSLs on all three Si orientations is reduced from -24.9% for the $1d_{Au(hkl)}x1d_{Si(hkl)}$ lattice to +0.13% for the $4d_{Au(hkl)}x3d_{Si(hkl)}$ CSL. In these CSLs the Au film would have very small compressive in-plane and tensile out-of-plane strains. Note that this same CSL was observed by Sayed *et al.* for epitaxial

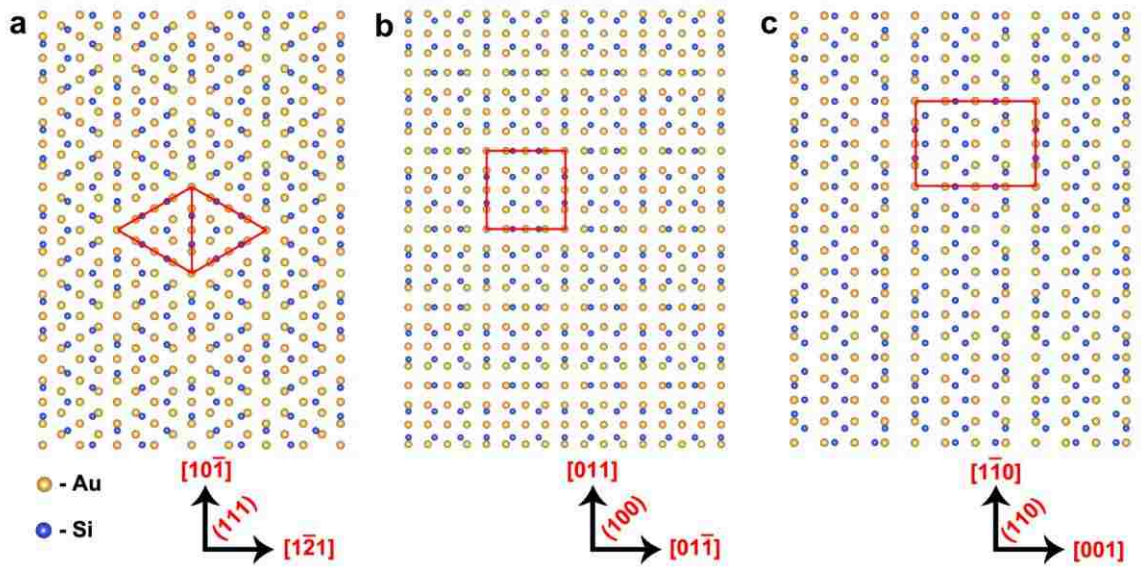

Figure 9. Interface models of Au on Si. (a) Au(111) on Si(111), (b) Au(100) on Si(100) and (c) Au(110) on Si(110) Moiré patterns result from 4 unit meshes of Au coinciding with 3 unit mesh of Si with a coincidence site lattice mismatch of +0.13%.

Au on Si produced by galvanic displacement[37] and by Li and Zuo for epitaxial Ag on Si produced by electron beam evaporation.[47]

In agreement with the CSL discussed above for Au on Si, the out-of-plane d-spacing as measured by XRD for very thin layers of Au on Si is greater than the bulk value of Au. Figure 10 shows the measured d_{111} for Au as a function of Au deposition time. The blue horizontal dashed line in Figure 10 corresponds to the d_{111} for bulk Au.

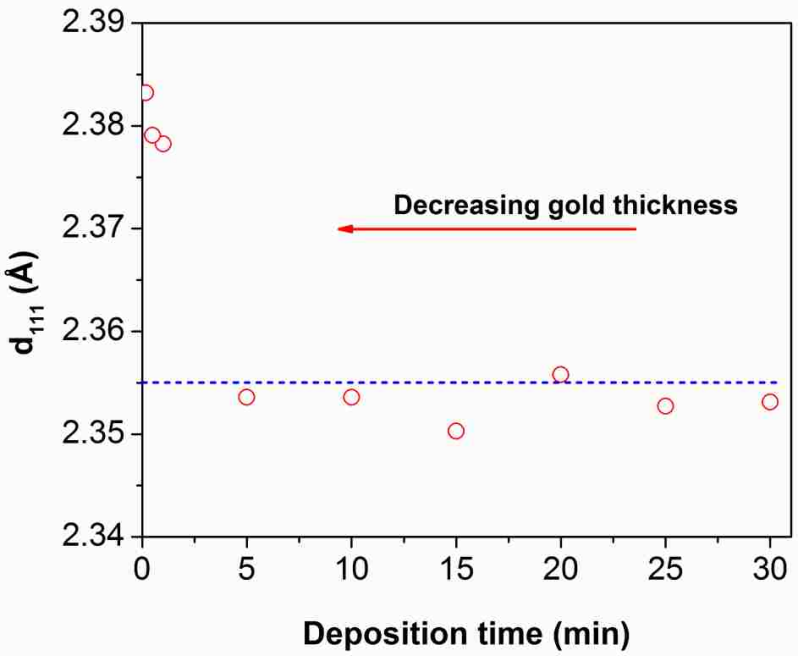

Figure 10. Evidence for out-of-plane tensile strain in ultra-thin Au(111) films on Si(111). Out-of-plane d_{111} spacing measured for Au(111) on Si(111) deposit as a function of deposition time showing out-of-plane tensile strain for short deposition times. The blue horizontal dashed line corresponds to d_{111} for bulk Au.

For deposition times from 5 minutes to 30 minutes, the measured out-of-plane d-spacing agrees well with the bulk value. The thickness of Au varies from 7.7 to 28.6 nm in this

range (see Figure 2). For deposition times shorter than 5 minutes we were not able to measure the film thickness, because the Au had not coalesced into a smooth film. At these shorter times the d_{111} is larger than the bulk value, consistent with compressive in-plane and tensile out-of-plane strains. This is also consistent with the CSL. If the mismatch were -24.9% as for a $1d_{Au(111)}x1d_{Si(111)}$, the in-plane strain would be tensile and the out-of-plane strain would be compressive.

CONCLUSIONS

We show that nanometer-thick electrodeposited epitaxial layers of Au on Si(111), Si(100), and Si(110) can serve as a platform for the electrodeposition of epitaxial thin films of Cu_2O. We exploit the fact that Si wafers with a high degree of perfection and well-defined orientation are both readily available and inexpensive. The highly-ordered Au/Si substrates cost a small fraction of the cost of bulk Au single crystals because of the low mass of Au that is used, they can conceivably be made as large as a Si wafer, and they may allow for the integration of electrodeposited functional ceramics with traditional semiconductor devices. A 28.3 nm thick film of Au on a 1 cm^2 substrate contains only 54 μg of Au. Films of Au deposited onto degenerate Si produce ohmic contacts, whereas films deposited onto moderately-doped n-type Si(111) produce a rectifying contact with a barrier height of 0.85 eV.

We use the method that Allongue and coworkers developed to deposit ultrathin Au films onto miscut Si(111).[38,39] The deposition is done at room temperature in a solution containing 0.1 mM $HAuCl_4$, 1 mM KCl, 1 mM H_2SO_4 and 0.1 M K_2SO_4 using a Si electrode that is pre-polarized at -1.9 V vs. Ag/AgCl before inserting it in the

deposition solution. The pre-polarization of the Si prevents the formation of an amorphous layer of SiO_x on the Si surface, as shown by cross-sectional TEM. The highest quality Au films are deposited onto Si(111). They are smooth enough to allow for thickness measurement by low-angle X-ray reflectivity and Laue oscillations, they are free of reflection twins, and they have an out-of-plane mosaic spread as low as 0.15^o.

The Au/Si interface is an interesting example of epitaxy, because high-quality, smooth Au epitaxial films are produced even though there is a -24.9% lattice mismatch between the Au film and Si substrate. The epitaxy in the Au/Si system can be explained by the formation of coincident site lattices (CSLs) in which 4 unit meshes of Au coincide with 3 unit meshes of Si. The lattice mismatch in the CSLs on all three Si orientations is reduced from -24.9% for the $1d_{Au(hkl)}x1d_{Si(hkl)}$ lattice to +0.13% for the $4d_{Au(hkl)}x3d_{Si(hkl)}$ CSL.

Epitaxial Cu_2O is deposited onto the Au/Si substrates by cathodic electrodeposition from an alkaline tartrate bath. The Cu_2O follows the out-of-plane and in-plane orientations of the Si substrates and Au buffer layers, as determined by X-ray pole figures. The Au and Cu_2O films deposited on Si(100) and Si(110) are both twinned. The films grown on Si(100) have reflection twins with a [221] orientation, and the films grown on Si(110) have reflection twins with a [411] orientation.

The method we have outlined for the deposition of epitaxial Cu_2O on Au/Si should be applicable to a very wide range of semiconductor and ceramic materials. It is especially well suited for applications that require a conducting back contact (e.g., solar cells) or require integration with single-crystal Si (e.g., solid-state memory).

MATERIALS AND METHODS

Si wafers and etching procedures. Si wafers with [111], [100] and [110] orientations were used to study epitaxial Au and Cu_2O electrodeposition. Phosphorous doped single-side polished n-Si(111) was miscut 0.2 degrees towards $[11\bar{2}]$ with resistivity of 1.15 ohm-cm. Phosphorus doped n^{++}-Si(100) with a resistivity of 0.001 ohm-cm and boron doped p^{++}-Si(110) with a resistivity less than 0.005 ohm-cm was used for the study of epitaxy. All wafers were obtained from Virginia Semiconductor Inc. Aluminum was sputtered on the back of Si wafers to form an ohmic contact, and silver wire with silver paste (GC electronics, silver print II) was used to make the back contact for all orientations. Either silicone paste or nail polish was used as an insulating and inert layer on the back of Si to prevent contact in the electrolyte during electrodeposition. All wafers prior to use were etched in 5% hydrofluoric acid solution for 30 seconds to dissolve the native oxide, then soaked in hot DI water (ca. 80-90 ^oC) for 15 minutes to passivate the surface with SiO_x layer and then etched again with 5% hydrofluoric acid for 30 seconds and buffered hydrofluoric acid for 30 seconds to produce a hydrogen-terminated surface. Ethanol was used to clean any organic residue and rinsed with DI water prior to deposition. All depositions were performed immediately after the etching process to avoid any surface passivation.

Electrodeposition of Au and Cu_2O films. Au was electrodeposited from a plating solution containing 0.1 mM $HAuCl_4$, 1 mM KCl, 1 mM H_2SO_4, and 100 mM K_2SO_4 in deionized (DI) water. The solution was prepared by adding 10 mL of a stock solution containing 1 mM $HAuCl_4$, 10 mM KCl, and 10 mM H_2SO_4 to 90 mL of DI water. Lastly, 100 mM K_2SO_4 was added as a supporting electrolyte to produce a final

solution with a pH of about 3. A -1.9 V vs. Ag/AgCl pre-polarized bias was applied at ambient temperatures with 200 rpm stirring. All depositions used an Ag/AgCl reference electrode and an Au coil as a high surface area counter electrode. The requisite step during deposition was the pre-polarization of the Si electrode prior to immersion in the electrolyte to avoid native oxide formation and also to prevent deposition of Au on Si by galvanic displacement. After the deposition, films were rinsed with DI water and dried in air. Cu_2O was electrodeposited from a plating solution containing 0.2 M $CuSO_4$, 0.2 M $C_4H_6O_6$ (tartaric acid), and 3.0 M NaOH. A cathodic current density of 1.0 mA cm^{-2} was passed for 100 seconds at a temperature of 30°C and a stir rate of 200 rpm. Cu_2O films on all orientations were deposited to a charge density of 0.1 C cm^{-2}. Electrodeposition of Au and Cu_2O films was done using either an EG&G Model 273A or an Autolab 30 potentiostat/galvanostat.

X-ray diffraction measurements and interface models. All XRD measurements were made with a Philips X'Pert Materials Research Diffractometer with Cu $K\alpha_1$ radiation source (λ=1.54056 Å). All 2theta-omega (out-of-plane orientation) scans were done using a 2-bounce hybrid monochromator with a Ge 220 monochromator and Ni 0.125 mm automatic beam attenuator and a 0.18^o parallel plate collimator diffracted optics. Pole figures were measured using a crossed slit collimator with 2 mm divergence slit and 2 mm mask with a Ni filter and a 0.27^o parallel plate collimator. Rocking curves (omega scans) were measured using the hybrid monochromator incident optics and a triple axis diffracted optics. X-ray reflectivity scans were measured using X-ray mirror Cu module with Ni 0.125 mm beam attenuator and a 0.18^o parallel plate collimator. Lattice constants for interface models and X-Ray measurements were obtained from

JCPDS card no. 027-1402 for Si, no. 004-0784 for Au, and no. 005-0667 for Cu_2O. All the interface models for Au on Si and Cu_2O on Au were made in VESTA (visualization for electronic and structural analysis) software ver. 3.3.2.

SEM measurements. Plan-view SEM images were obtained at 5 kV using a Helios NanoLab DualBeam instrument for the Au(111) film, and at 15 kV on an Hitachi S4700 instrument for the Au(100) and Au(110) films.

TEM measurements. Focused ion-beam milling for TEM sample preparation was done using the Helios NanoLab DualBeam. Prior to focused ion-beam milling, the films were sputtered with a thin AuPd layer to protect the Au and Cu_2O films during the milling process, and to provide a contrast difference to determine the thickness of films accurately. High-resolution TEM images and electron diffraction patterns for individual layers were measured using the Tecnai F20 transmission electron microscope.

Measurement of interfacial energetics. All J-V and Mott-Schottky curves were measured using a PARSTAT 2273 potentiostat/galvanostat with Au coil as top contact (schematic shown in the inset of Figure 3a) and Mott-Schottky scans were collected at a 50 mV/s scan rate and 1 MHz modulation frequency.

ASSOCIATED CONTENT

Supporting information. The Supporting information is available free of charge on the ACS Publications website at DOI: 10.1021/acsami.6b04552.

Schematic showing θ, ω, χ, and φ angles for X-ray diffraction measurements, electron diffraction patterns of Au(111) and Si(111), stereographic projections used to assign peaks in X-ray pole figures, azimuthal and tilt scans of Cu_2O and Au on Si(111),

X-ray diffraction pattern of a thick Au film on Si(110), interface model of Cu_2O on Au, and transformation matrices for twinning in face-centered-cubic systems (PDF).

AUTHOR INFORMATION

Corresponding Author

*Email: jswitzer@mst.edu.

Present Addresses

[§]Bioanalytical Systems, Inc., 2701 Kent Avenue, West Lafayette, IN 47906, United States.

Notes

The authors declare no competing financial interest.

ACKNOWLEDGMENTS

This material is based upon work supported by the U.S. Department of Energy, Office of Basic Energy Sciences, Division of Materials Sciences and Engineering, under Grant No. DE-FG02-08ER46518.

REFERENCES

1. Kolb, D. M.; Przasnyski, M.; Gerischer, H. Underpotential Deposition of Metals and Work Function Differences. *J. Electroanal. Chem. Interfacial Electrochem.* **1974**, *54*, 25-38.

2. Herrero, E.; Buller, L. J.; Abruna, H. D. Underpotential Deposition at Single Crystal Surfaces of Au, Pt, Ag and Other Materials. *Chem. Rev.* **2001**, *101*, 1897-1930.

3. Brankovic, S. R.; Wang, J. X.; Adzic, R. R. Metal Monolayer Deposition by Replacement of Metal Adlayers on Electrode Surfaces. *Surf. Sci.* **2001**, *474*, L173-L179.

4. Stickney, J. L. Electrochemical Atomic Layer Epitaxy. *Electroanal. Chem.* **1999**, *21*, 75-209.

5. Gregory, B. W.; Stickney, J. L. Electrochemical Atomic Layer Epitaxy (ECALE). *J. Electroanal. Chem. Interfacial Electrochem.* **1991**, *300*, 543-561.

6. Vaidyanathan, R.; Cox, S. M.; Happek, U.; Banga, D.; Mathe, M. K.; Stickney, J. L. Preliminary Studies in the Electrodeposition of PbSe/PbTe Superlattice Thin Films via Electrochemical Atomic Layer Deposition (ALD). *Langmuir* **2006**, *22*, 10590-10595.

7. Villegas, I.; Stickney, J. L. Preliminary Studies of Gallium Arsenide Deposition on Gold (100), (110), and (111) Surfaces by Electrochemical Atomic Layer Epitaxy. *J. Electrochem. Soc.* **1992**, *139*, 686-694.

8. Huang, B. M.; Colletti, L. P.; Gregory, B. W.; Anderson, J. L.; Stickney, J. L. Preliminary Studies of the Use of an Automated Flow-cell Electrodeposition System for the Formation of CdTe Thin Films by Electrochemical Atomic Layer Epitaxy. *J. Electrochem. Soc.* **1995**, *142*, 3007-3016.

9. Switzer, J. A.; Liu, R.; Bohannan, E. W.; Ernst, F. Epitaxial Electrodeposition of a Crystalline Metal Oxide onto Single-Crystalline Silicon. *J. Phys. Chem. B* **2002**, *106*, 12369-12372.

10. Liu, R.; Bohannan, E. W.; Switzer, J. A.; Oba, F.; Ernst, F. Epitaxial Electrodeposition of Cu_2O Films onto InP(001). *Appl. Phys. Lett.* **2003**, *83*, 1944-1946.

11. Liu, R.; Oba, F.; Bohannan, E. W.; Ernst, F.; Switzer, J. A. Shape Control in Epitaxial Electrodeposition: Cu_2O Nanocubes on InP(001). *Chem. Mater.* **2003**, *15*, 4882-4885.

12. Liu, R.; Kulp, E. A.; Oba, F.; Bohannan, E. W.; Ernst, F.; Switzer, J. A. Epitaxial Electrodeposition of High-Aspect-Ratio $Cu_2O(110)$ Nanostructures on InP(111). *Chem. Mater.* **2005**, *17*, 725-729.

13. Switzer, J. A.; Shumsky, M. G.; Bohannan, E. W. Electrodeposited Ceramic Single Crystals. *Science* **1999**, *284*, 293-296.

14. Bohannan, E. W.; Jaynes, C. C.; Shumsky, M. G.; Barton, J. K.; Switzer, J. A. Low-temperature Electrodeposition of the High-temperature Cubic Polymorph of Bismuth(III) Oxide. *Solid State Ionics* **2000**, *131*, 97-107.

15. Bohannan, E. W.; Shumsky, M. G.; Switzer, J. A. Epitaxial Electrodeposition of Copper(I) Oxide on Single-Crystal Gold(100). *Chem. Mater.* **1999**, *11*, 2289-2291.

16. Switzer, J. A.; Kothari, H. M.; Bohannan, E. W. Thermodynamic to Kinetic Transition in Epitaxial Electrodeposition. *J. Phys. Chem. B* **2002**, *106*, 4027-4031.

17. Oba, F.; Ernst, F.; Yu, Y.; Liu, R.; Kothari, H. M.; Switzer, J. A. Epitaxial Growth of Cuprous Oxide Electrodeposited onto Semiconductor and Metal Substrates. *J. Am. Ceram. Soc.* **2005**, *88*, 253-270.

18. Liu, R.; Vertegel, A. A.; Bohannan, E. W.; Sorenson, T. A.; Switzer, J. A. Epitaxial Electrodeposition of Zinc Oxide Nanopillars on Single-crystal Gold. *Chem. Mater.* **2001**, *13*, 508-512.

19. Limmer, S. J.; Kulp, E. A.; Switzer, J. A. Epitaxial Electrodeposition of ZnO on Au(111) from Alkaline Solution: Exploiting Amphoterism in Zn(II). *Langmuir* **2006**, *22*, 10535-10539.

20. Nikiforov, M. P.; Vertegel, A. A.; Shumsky, M. G.; Switzer, J. A. Epitaxial Electrodeposition of Fe_3O_4 on Single-crystal Au(111). *Adv. Mater. (Weinheim, Ger.)* **2000**, *12*, 1351-1353.

21. Sorenson, T. A.; Morton, S. A.; Waddill, G. D.; Switzer, J. A. Epitaxial Electrodeposition of Fe_3O_4 Thin Films on the Low-Index Planes of Gold. *J. Am. Chem. Soc.* **2002**, *124*, 7604-7609.

22. Kulp, E. A.; Kothari, H. M.; Limmer, S. J.; Yang, J.; Gudavarthy, R. V.; Bohannan, E. W.; Switzer, J. A. Electrodeposition of Epitaxial Magnetite Films and Ferrihydrite Nanoribbons on Single-Crystal Gold. *Chem. Mater.* **2009**, *21*, 5022-5031.

23. Switzer, J. A.; Gudavarthy, R. V.; Kulp, E. A.; Mu, G.; He, Z.; Wessel, A. J. Resistance Switching in Electrodeposited Magnetite Superlattices. *J. Am. Chem. Soc.* **2010**, *132*, 1258-1260.

24. He, Z.; Gudavarthy, R. V.; Koza, J. A.; Switzer, J. A. Room-temperature Electrochemical Reduction of Epitaxial Magnetite Films to Epitaxial Iron Films. *J. Am. Chem. Soc.* **2011**, *133*, 12358-12361.

25. Switzer, J. A.; Kothari, H. M.; Poizot, P.; Nakanishi, S.; Bohannan, E. W. Enantiospecific Electrodeposition of a Chiral Catalyst. *Nature* **2003**, *425*, 490-493.

26. Kothari, H. M.; Kulp, E. A.; Boonsalee, S.; Nikiforov, M. P.; Bohannan, E. W.; Poizot, P.; Nakanishi, S.; Switzer, J. A. Enantiospecific Electrodeposition of Chiral CuO Films from Copper(II) Complexes of Tartaric and Amino Acids on Single-Crystal Au(001). *Chem. Mater.* **2004**, *16*, 4232-4244.

27. Boonsalee, S.; Gudavarthy, R. V.; Bohannan, E. W.; Switzer, J. A. Epitaxial Electrodeposition of Tin(II) Sulfide Nanodisks on Single-Crystal Au(100). *Chem. Mater.* **2008**, *20*, 5737-5742.

28. He, Z.; Koza, J. A.; Mu, G.; Miller, A. S.; Bohannan, E. W.; Switzer, J. A. Electrodeposition of $Co_xFe_{3-x}O_4$ Epitaxial Films and Superlattices. *Chem. Mater.* **2013**, *25*, 223-232.

29. Koza, J. A.; Schroen, I. P.; Willmering, M. M.; Switzer, J. A. Electrochemical Synthesis and Nonvolatile Resistance Switching of Mn_3O_4 Thin Films. *Chem. Mater.* **2014**, *26*, 4425-4432.

30. Koza, J. A.; He, Z.; Miller, A. S.; Switzer, J. A. Electrodeposition of Crystalline Co_3O_4-A Catalyst for the Oxygen Evolution Reaction. *Chem. Mater.* **2012**, *24*, 3567-3573.

31. Koza, J. A.; Hill, J. C.; Demster, A. C.; Switzer, J. A. Epitaxial Electrodeposition of Methylammonium Lead Iodide Perovskites. *Chem. Mater.* **2016**, *28*, 399-405.

32. Switzer, J. A.; Shane, M. J.; Phillips, R. J. Electrodeposited Ceramic Superlattices. *Science* **1990**, *247*, 444-446.

33. Switzer, J. A.; Raffaelle, R. P.; Phillips, R. J.; Hung, C. J.; Golden, T. D. Scanning Tunneling Microscopy of Electrodeposited Ceramic Superlattices. *Science* **1992**, *258*, 1918-1921.

34. Switzer, J. A.; Hung, C. J.; Breyfogle, B. E.; Shumsky, M. G.; Van Leeuwen, R.; Golden, T. D. Electrodeposited Defect Chemistry Superlattices. *Science* **1994**, *264*, 1573-1576.

35. Kothari, H. M.; Vertegel, A. A.; Bohannan, E. W.; Switzer, J. A. Epitaxial Electrodeposition of Pb-Tl-O Superlattices on Single-Crystal Au(100). *Chem. Mater.* **2002**, *14*, 2750-2756.

36. Love, J. C.; Estroff, L. A.; Kriebel, J. K.; Nuzzo, R. G.; Whitesides, G. M. Self-assembled Monolayers of Thiolates on Metals as a Form of Nanotechnology. *Chem. Rev.* **2005**, *105*, 1103-1169.

37. Sayed, S. Y.; Wang, F.; Malac, M.; Meldrum, A.; Egerton, R. F.; Buriak, J. M. Heteroepitaxial Growth of Gold Nanostructures on Silicon by Galvanic Displacement. *ACS Nano* **2009**, *3*, 2809-2817.

38. Prod'homme, P.; Maroun, F.; Cortes, R.; Allongue, P. Electrochemical Growth of Ultraflat Au(111) Epitaxial Buffer Layers on H-Si(111). *Appl. Phys. Lett.* **2008**, *93*, 171901.

39. Warren, S.; Prod'homme, P.; Maroun, F.; Allongue, P.; Cortes, R.; Ferrero, C.; Lee, T.-L.; Cowie, B. C. C.; Walker, C. J.; Ferrer, S.; Zegenhagen, J. Electrochemical Au Deposition on Stepped Si(111)-H surfaces: 3D versus 2D Growth Studied by AFM and X-ray Diffraction. *Surf. Sci.* **2009**, *603*, 1212-1220.

40. Allongue, P.; Maroun, F. Electrodeposited Magnetic Layers in the Ultrathin Limit. *MRS Bull.* **2010**, *35*, 761-770.

41. Tournerie, N.; Engelhardt, A. P.; Maroun, F.; Allongue, P. Influence of the Surface Chemistry on the Electric-field Control of the Magnetization of Ultrathin Films. *Phys. Rev. B* **2012**, *86*, 104434.

42. Kulp, E. A.; Limmer, S. J.; Bohannan, E. W.; Switzer, J. A. Electrodeposition of Nanometer-thick Ceria Films by Oxidation of Cerium(III)-acetate. *Solid State Ionics* **2007**, *178*, 749-757.

43. Phung, T. M.; Johnson, D. C.; Antonelli, G. A. A Detailed Experimental and Analytical Study of the Thermal Expansion of Dielectric Thin Films on Si by X-ray Reflectivity. *J. Appl. Phys.* **2006**, *100*, 064317.

44. Hill, J. C.; Landers, A. T.; Switzer, J. A. An Electrodeposited Inhomogeneous Metal-insulator-semiconductor Junction for Efficient Photoelectrochemical Water Oxidation. *Nat. Mater.* **2015**, *14*, 1150-1155.

45. Poizot, P.; Hung, C.-J.; Nikiforov, M. P.; Bohannan, E. W.; Switzer, J. A. An Electrochemical Method for CuO Thin Film Deposition from Aqueous Solution. *Electrochem. Solid-State Lett.* **2003**, *6*, C21-C25.

46. Thomas, G.; Goringe, M. J.: *Transmission Electron Microscopy of Materials*; John Wiley & Sons: New York, 1979. pp. 94-100.

47. Li, B. Q.; Zuo, J. M. The Development of Epitaxy of Nanoclusters on Lattice-Mismatched Substrates: Ag on H-Si(111) Surfaces. *Surf. Sci.* **2002**, *520*, 7-17.

SUPPORTING INFORMATION

NANOMETER-THICK GOLD ON SILICON AS A PROXY FOR SINGLE-CRYSTAL GOLD FOR THE ELECTRODEPOSITION OF EPITAXIAL CUPROUS OXIDE THIN FILMS

Jay A. Switzer,[†,*] *James C. Hill,*[†] *Naveen K. Mahenderkar,*[‡] *and Ying-Chau Liu*[†]

[†]Department of Chemistry and Graduate Center for Materials Research, Missouri University of Science and Technology, Rolla, Missouri 65409-1170, United States, and

[‡]Department of Materials Science and Engineering and Graduate Center for Materials Research, Missouri University of Science and Technology, Rolla, Missouri 65409-1170, United States.

Corresponding author – jswitzer@mst.edu

X-ray measurement geometry showing θ, ω, φ, χ angles

X-ray rocking curves, azimuthal scans and pole figures are texture analysis tools for highly ordered crystalline materials. All of these scans require 2θ angle fixed at the peak of interest. For example, 2θ = 47.304° for probing the Si(220) plane(s). The sample stage is tilted or rotated in different directions and angles in order to determine the in-plane and out-of-plane order of the sample. As shown in Figure S1, rocking the sample along the axis perpendicular to the source-sample-detector plane is known as the ω scan or rocking curve. Rocking curves determine the mosaic spread of the out-of-plane orientation. Rotation of the sample around the sample normal is the φ scan, or the azimuthal scan. Tilting the sample along the axis orthogonal to both the ω and the φ axes is the χ scan (or sometimes referred to as the ψ scan). Diffraction signals collected from the azimuthal scans (φ = 0° to 360°) at each tilt angle (χ = 0° to 90°) can be used to construct a pole figure.

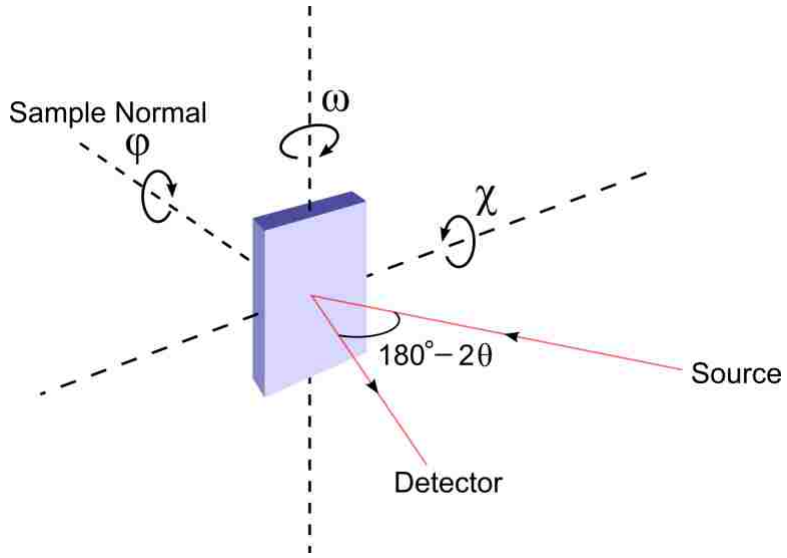

Figure S1. X-ray diffraction geometry showing θ, ω, φ, χ angles

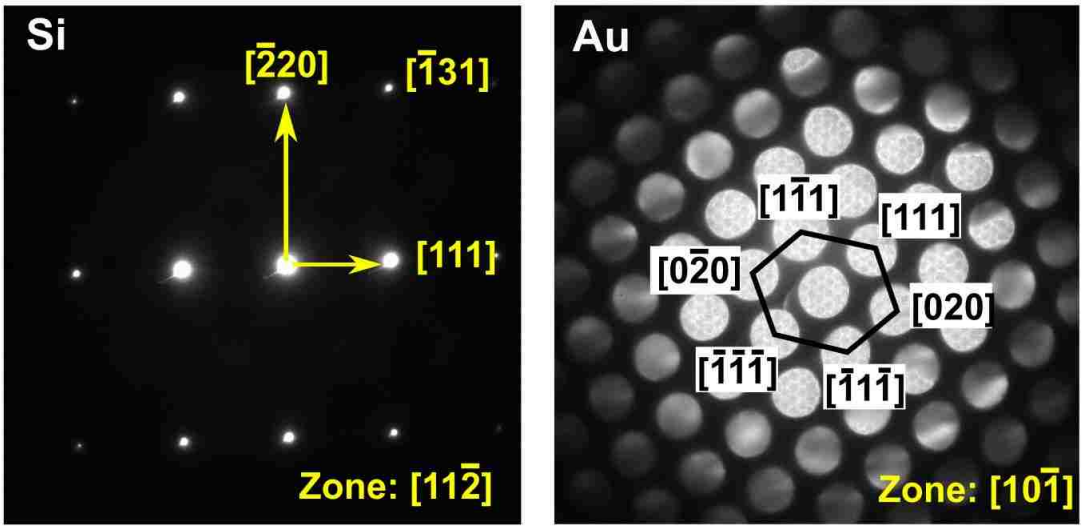

Figure S2. Electron diffraction patterns of Si and Au. Electron diffraction patterns of Si along zone axis [11$\bar{2}$] and Au along zone axis [10$\bar{1}$] showing spot pattern. Convergent beam diffraction was performed for Au because of lower thickness of the film (~30 nm).

Stereographic projections of Si, Au and Cu_2O

The out-of-plane and in-plane orientations of films relative to substrates can be determined from X-ray pole figures. Stereographic projections display the expected peak positions in each X-ray pole figure pattern. The stereographic projections shown in Figure S3 were simulated using CaRine software. Figure S3-a is the stereographic projection of Si(220) poles on the Cu_2O/Au/Si(111) sample. Because of the three-fold symmetry around the [111] direction, three spots (φ = 120° apart) are expected and shown as the closed circles in Figure S3-a. The tilt angle of these three spots is χ = 35.26°, which is the angle between [111] and [110]. Due to the narrow diffraction peaks of the Si substrates, the peaks at χ = 90° are usually not observed. Figure S3-b represents the stereographic projection for the domain that is antiparallel to the domain in Figure S3-a. The antiparallel domain is only seen in the electrodeposited Au and Cu_2O layers.

Notice that the pattern of the antiparallel domain (shown as open circles) is rotated 180° with respect to the pattern of the parallel domain. When both domains are present in a sample, the resulting stereographic projection becomes the combination of both, as shown in Figure S3-c. The closed circles enclosed by the open circles represent the overlapping pattern between parallel and antiparallel domains.

Figure S3-d shows the simulated Si(111) poles on the Cu_2O/Au/Si(100) sample. The 4-fold symmetry along the [100] out-of-plane direction results in 4 spots separated at $\varphi = 90°$. The tilt angle of $\chi = 54.74°$ originates from the angle between [100] and [111]. The (111) poles of Au and Cu_2O are at identical positions as the Si(111) poles of the same sample. The red triangles in Figure S3-e are also the Au(111) or Cu_2O(111) poles, but their out-of-plane direction is [221], which is the twin of [300]. The triangles at different tilt angles are attributed to different angles between different directions. The tilt angle from [221] to [111] is 15.79°, to $[11\bar{1}]$ is 54.74°, and to $[\bar{1}11]$ and $[1\bar{1}1]$ is 78.90°. Rotating the pattern of this twin 4-fold around the [221] direction results in the pattern (open triangles) shown in Figure S3-f.

Figure S3-g represents the simulated Si(111) poles on the Cu_2O/Au/Si(110) sample. Two spots at $\chi = 35.26°$ are due to the angle between [110] and [111], and the 2-fold symmetry around the [110] pole results in $\varphi = 180°$ separation of the spots. The same pattern is observed in Au(111) and Cu_2O(111) stereographic projections of the same sample. The [330] has a twin of [411]. The stars in Figure S3-h represent a set of the (111) poles from the twin. The tilt angle from [411] to [111] is 35.26°, to $[11\bar{1}]$ and $[1\bar{1}1]$ is 57.02° and to $[1\bar{1}\bar{1}]$ is 74.21°. The 2-fold rotation symmetry around the [411] direction results in the other set of (111) poles, indicated as the open stars in Figure S3-i.

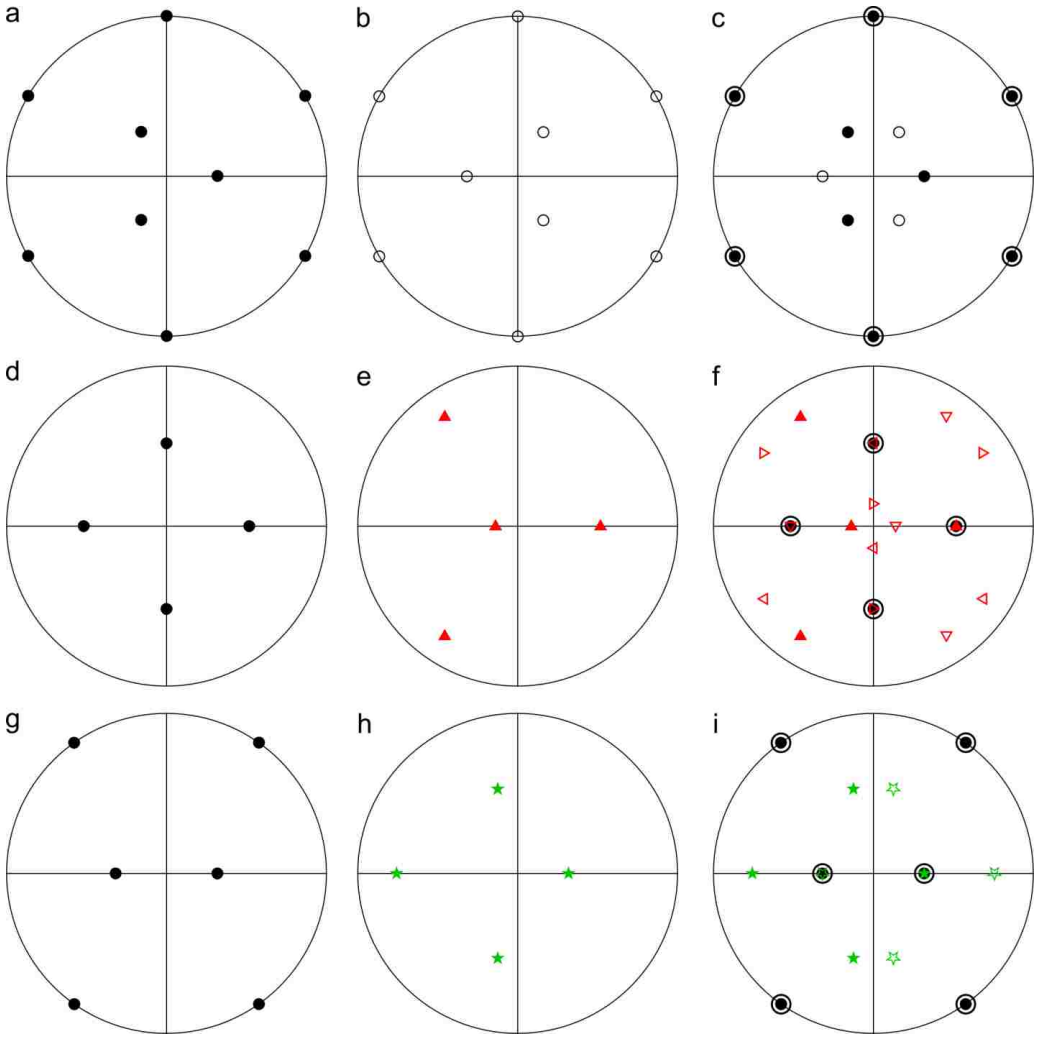

Figure S3. Stereographic projections of (a-c) (220) poles on the Cu_2O/Au/Si(111) sample, (d-f) (111) poles on the Cu_2O/Au/Si(100) sample, and (g-i) (111) poles on the Cu_2O/Au/Si(110) sample. The patterns from the parallel domains are shown as closed circles whereas the patterns from the antiparallel domains are shown as open circles. For the [111] out-of-plane sample, the (220) poles of Cu_2O, Au and Si all exhibit the same pattern as in (a). However, the deposited Cu_2O and Au have antiparallel domains whose pattern is shown in (b). The resulting pattern is the combination of both (a) and (b), which is shown in (c). For the [100] out-of-plane sample, the (111) poles of Cu_2O, Au and Si all have the same pattern as in (d). Cu_2O and Au films on the Si(100) substrate have twins whose out-of-plane is [221]. One set of the (111) poles of the twin is shown in (e). Rotating the pattern in (e) 4-fold around the out-of-plane direction results in the pattern in (f), where the circles are from the parallel and antiparallel (100) domains, and the triangles are from the twin (221) domains. For the [110] out-of-plane sample, the (111) poles of Cu_2O, Au and Si all have the same pattern as in (g). The twins in Cu_2O and Au layers are [411] out-of-plane, and one set of their (111) poles are shown as stars in (h). Because of the 2-fold symmetry around the out-of-plane direction, the overall patterns for Cu_2O and Au layers are presented in (i), where the circles are from the parallel and antiparallel (110) domains, and the stars are from the twin (411) domains.

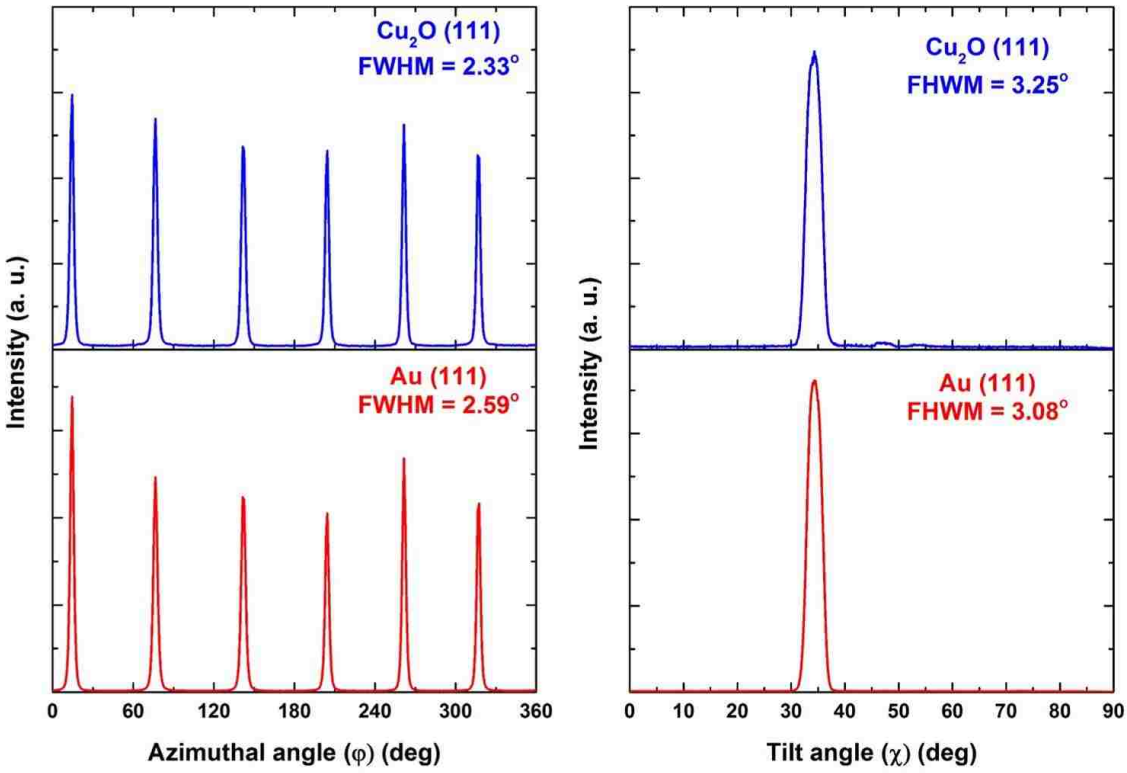

Figure S4. Azimuthal and tilt scans of Cu_2O and Au on Si(111). (a) Azimuthal scan (φ-scans) of Au on Si(111) (red) and Cu_2O on Au/Si(111) (blue) was performed for 0 to 360° φ at a tilt angle of 35.3°. FWHM of Au on Si(111) is 2.59° and Cu_2O on Au/Si(111) is 2.33°. (b) Tilt scans (χ-scans) of Au on Si(111) (red) with a FWHM of 3.08° and Cu_2O on Au/Si(111) (blue) with a FWHM of 3.25° was performed for 0 to 90° χ.

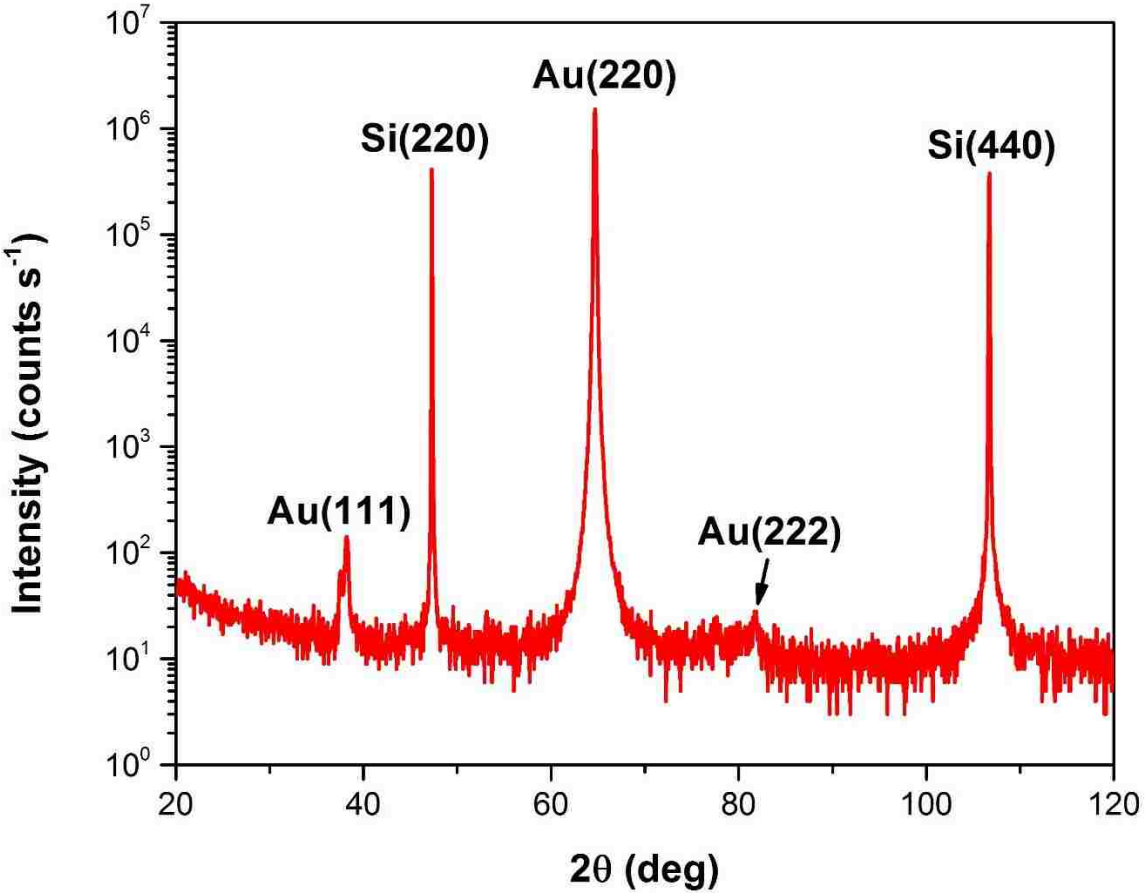

Figure S5. X-ray diffraction pattern of thick Au on Si. Out-of-plane orientation of thick (*ca.* 5 μm) Au on Si(110). A strong epitaxial Au[110] orientation is observed with minor Au[111] orientation.

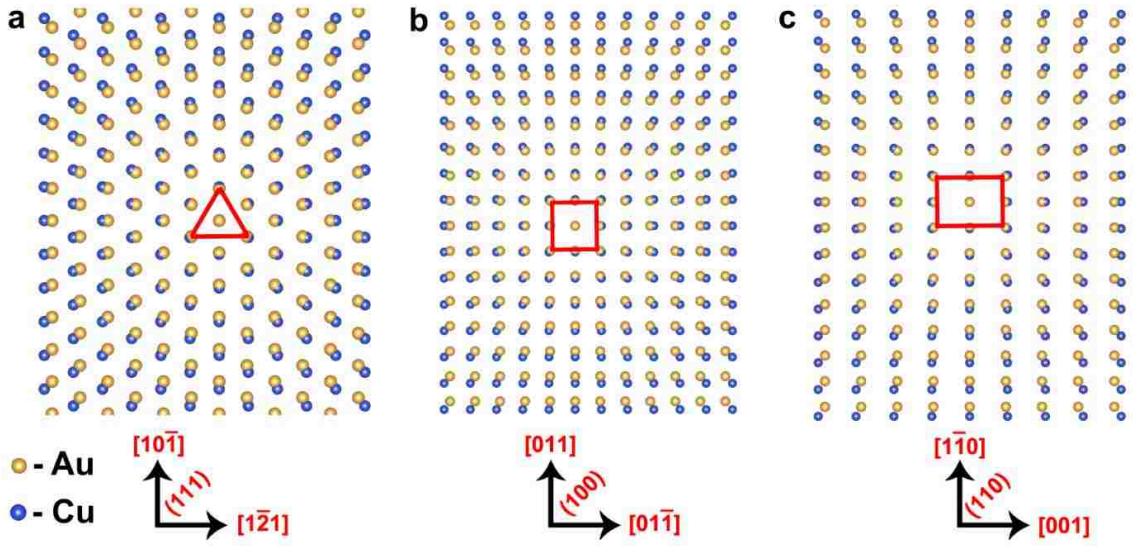

Figure S6. Interface models of Cu_2O on Au. Interface models of Cu atoms of Cu_2O (blue colored) overlay on Au atoms (gold colored) for (a) $Cu_2O(111)/Au(111)$, (b) $Cu_2O(100)/Au(100)$ and (c) $Cu_2O(110)/Au(110)$ orientations. A lattice mismatch of +4.7% is observed for 1 x 1 unit mesh of Cu_2O on Au for all orientations.

Transformation matrices for twinning in face-centered cubic systems

Twinning can be described by the matrix, $T_{(hkl)}$, by the relationship

$$(PQR) = T_{(hkl)}(pqr) \tag{1}$$

where (PQR) is a column matrix for the lattice plane in a twinned crystallite that corresponds to the lattice plane, (pqr), of the original crystallite after twinning on (hkl). The indices of reciprocal lattice point (PQR) for the twinned crystal will be related to the point (pqr) in the reciprocal lattice of original crystal after twinning on (hkl) plane by the following general expression:

$$P = \frac{p(h^2 - k^2 - l^2) + q(2hk) + r(2hl)}{(h^2 + k^2 + l^2)}$$

$$Q = \frac{p(2hk) + q(-h^2 + k^2 - l^2) + r(2kl)}{(h^2 + k^2 + l^2)}$$

$$R = \frac{p(2hl) + q(2kl) + r(-h^2 - k^2 + l^2)}{(h^2 + k^2 + l^2)}$$

In the matrix form $(PQR) = T_{(hkl)}(pqr)$ can be represented as a general twin matrix

$$T_{(hkl)} = \left(\frac{1}{h^2 + k^2 + l^2}\right)\begin{pmatrix} h^2 - k^2 - l^2 & 2hk & 2hl \\ 2hk & -h^2 + k^2 - l^2 & 2kl \\ 2hl & 2kl & -h^2 - k^2 + l^2 \end{pmatrix} \tag{2}$$

In face-centered cubic crystal structures, twinning occurs on {111} slip planes, and the twinning matrix becomes,

$$T_{(111)} = \left(\frac{1}{3}\right)\begin{pmatrix} -1 & 2 & 2 \\ 2 & -1 & 2 \\ 2 & 2 & -1 \end{pmatrix} \tag{3}$$

Twin plane for Au on Si(100):

$(pqr) = (300)$ and $(hkl) = (111)$

$$\begin{pmatrix} P \\ Q \\ R \end{pmatrix} = \left(\frac{1}{3}\right)\begin{pmatrix} -1 & 2 & 2 \\ 2 & -1 & 2 \\ 2 & 2 & -1 \end{pmatrix}\begin{pmatrix} 3 \\ 0 \\ 0 \end{pmatrix}$$

$$\begin{pmatrix} P \\ Q \\ R \end{pmatrix} = \left(\frac{1}{3}\right)\begin{pmatrix} \bar{3} \\ 6 \\ 6 \end{pmatrix} = \begin{pmatrix} \bar{1} \\ 2 \\ 2 \end{pmatrix}$$

Twin plane for Au on Si(110):

$(pqr) = (330)$ and $(hkl) = (111)$

$$\begin{pmatrix} P \\ Q \\ R \end{pmatrix} = \left(\frac{1}{3}\right)\begin{pmatrix} -1 & 2 & 2 \\ 2 & -1 & 2 \\ 2 & 2 & -1 \end{pmatrix}\begin{pmatrix} 3 \\ 3 \\ 0 \end{pmatrix}$$

$$\begin{pmatrix} P \\ Q \\ R \end{pmatrix} = \left(\frac{1}{3}\right)\begin{pmatrix} 3 \\ 3 \\ 12 \end{pmatrix} = \begin{pmatrix} 1 \\ 1 \\ 4 \end{pmatrix}$$

Twin plane for Au on Si(111):

$(pqr) = (\bar{3}30)$ and $(hkl) = (111)$

$$\begin{pmatrix} P \\ Q \\ R \end{pmatrix} = \left(\frac{1}{3}\right)\begin{pmatrix} -1 & 2 & 2 \\ 2 & -1 & 2 \\ 2 & 2 & -1 \end{pmatrix}\begin{pmatrix} \bar{3} \\ 3 \\ 3 \end{pmatrix}$$

$$\begin{pmatrix} P \\ Q \\ R \end{pmatrix} = \left(\frac{1}{3}\right)\begin{pmatrix} 15 \\ \bar{3} \\ \bar{3} \end{pmatrix} = \begin{pmatrix} 5 \\ \bar{1} \\ \bar{1} \end{pmatrix}$$

Thus, using the general matrix and applying the twin plane matrix transformation, the following twinning planes result.

$$(pqr) = (300); (PQR) = (\bar{1}22)$$

$$(pqr) = (330); (PQR) = (114)$$

$$(pqr) = (\bar{3}33); (PQR) = (5\bar{1}\bar{1})$$

SECTION

2. CONCLUSIONS

To reduce the CO_2 emission while meeting the global energy demand, there must be invention, development, and deployment of schemes for large scale carbon-neutral energy production. Solar energy is an abundant resource, and one promising scheme is to convert solar energy into chemical potential. The work presented in this dissertation provides useful information for the development of solar energy conversion and storage. Paper I introduces the electrodeposition of β-$Co(OH)_2$ by reducing tris(ethylenediamine)-cobalt(III) in alkaline solution. The kinetically inert Co(III) complex, $[Co(en)_3]^{3+}$, is 35 orders of magnitude more stable than the kinetically labile Co(II) complex, $[Co(en)_3]^{2+}$. When $[Co(en)_3]^{3+}$ is electrochemically reduced to $[Co(en)_3]^{2+}$ in alkaline solution, Co(II) reacts with excess hydroxide ion to produce β-$Co(OH)_2$. The surface of β-$Co(OH)_2$ is converted to CoOOH at potentials where oxygen evolution occurs.

The full conversion of $Co(OH)_2$ to CoOOH and Co_3O_4 is described in Paper II. $Co(OH)_2$ can be fully converted to CoOOH by electrochemical oxidation at 95°C in 1 M KOH and to Co_3O_4 by thermal decomposition at 300°C in air. The overall morphology is retained upon conversion, but micro- cracks and pores develop due to the volume shrinkage (24.5% from $Co(OH)_2$ to CoOOH and 28.6% from CoOOH to Co_3O_4). Tafel analysis compares the catalytic activity towards OER between CoOOH and Co_3O_4, and Co_3O_4 appears to be the superior catalyst. However, when the observed current densities were corrected for the measured electrochemically active areas, the linear regions of the

two Tafel plots fell on the same line—suggesting that the active species, likely Co(IV), for the OER is the same on both materials.

Paper III describes the electrodeposition of ultrathin Au films on Si substrates. The smooth Au films can be deposited from 7 nm to 28 nm (determined by low-angle X-ray reflectivity and X-ray Laue oscillations) and are epitaxial to the Si. The Au/Si system can serve as an inexpensive and convenient alternative to single crystal gold substrates. Moreover, high-resolution TEM indicates no SiO_x layer between the Si and Au. The Au/n-Si junction exhibits Schottky behavior which may be useful in the applications of photoelectrochemical devices.

REFERENCES

1. Holdren, J. P.: Energy and sustainability. *Science (Washington, DC, U. S.)* **2007**, *315*, 737.

2. Lewis, N. S.; Nocera, D. G.: Powering the planet: Chemical challenges in solar energy utilization. *Proc. Natl. Acad. Sci. U. S. A.* **2006**, *103*, 15729-15735.

3. Yang, Y.; Gu, J.; Young, J. L.; Miller, E. M.; Turner, J. A.; Neale, N. R.; Beard, M. C.: Semiconductor interfacial carrier dynamics via photoinduced electric fields. *Science (Washington, DC, U. S.)* **2015**, *350*, 1061-1065.

4. Koza, J. A.; Hill, J. C.; Demster, A. C.; Switzer, J. A.: Epitaxial electrodeposition of methylammonium lead iodide perovskites. *Chem. Mater.* **2016**, *28*, 399-405.

5. Bahlawane, N.; Kohse-Hoeinghaus, K.; Weimann, T.; Hinze, P.; Roehe, S.; Baeumer, M.: Rational design of functional oxide thin films with embedded magnetic or plasmonic metallic nanoparticles. *Angew. Chem., Int. Ed.* **2011**, *50*, 9957-9960, S9957/9951-S9957/9956.

6. Suh, S.; Hoffman, D. M.; Atagi, L. M.; Smith, D. C.; Liu, J.-R.; Chu, W.-K.: Precursor oxidation state control of film stoichiometry in the metal-organic chemical vapor deposition of tin oxide thin films. *Chem. Mater.* **1997**, *9*, 730-735.

7. Thomann, A.-L.; Vahlas, C.; Aloui, L.; Samelor, D.; Caillard, A.; Shaharil, N.; Blanc, R.; Millon, E.: Conformity of aluminum thin films deposited onto micro-patterned silicon wafers by pulsed laser deposition, magnetron sputtering, and CVD. *Chem. Vap. Deposition* **2011**, *17*, 366-374.

8. Habermeier, H.-U.: Thin films of perovskite-type complex oxides. *Mater. Today (Oxford, U. K.)* **2007**, *10*, 34-43.

9. Xie, L.; Leester-Schaedel, M.; Ziegmann, G.; Buettgenbach, S.: Effect of physical vapor deposition metallic thin films on micro injection molded weld line mechanical properties. *Microsyst. Technol.* **2010**, *16*, 1009-1013.

10. Kawae, T.; Hu, J.; Naganuma, H.; Nakajima, T.; Terauchi, Y.; Okamura, S.; Morimoto, A.: Hysteresis loops of polarization and magnetization in $(BiNd_{0.05})(Fe_{0.97}Mn_{0.03})O_3/Pt/CoFe_2O_4$ layered epitaxial thin film grown by pulsed laser deposition. *Thin Solid Films* **2011**, *519*, 7727-7730.

11. Chambers, S. A.: Epitaxial growth and properties of doped transition metal and complex oxide films. *Adv. Mater. (Weinheim, Ger.)* **2010**, *22*, 219-248.

12. Herman, M. A.; Sitter, H. *Springer Series in Materials Science, Vol. 7: Molecular Beam Epitaxy: Fundamentals and Current Status*, 1989.

13. Huang, H.; Miao, H.; Luo, H.; Yao, X.: Thin films derived from hydrothermal technique. *Guisuanyan Tongbao* **2002**, *21*, 58-62.

14. Prod'homme, P.; Maroun, F.; Cortes, R.; Allongue, P.: Electrochemical growth of ultraflat Au(111) epitaxial buffer layers on H-Si(111). *Appl. Phys. Lett.* **2008**, *93*, 171901/171901-171901/171903.

15. Hill, J. C.; Landers, A. T.; Switzer, J. A.: An electrodeposited inhomogeneous metal-insulator-semiconductor junction for efficient photoelectrochemical water oxidation. *Nat. Mater.* **2015**, *14*, 1150-1155.

16. Svedberg, E. B.; Mallett, J. J.; Sayan, S.; Shapiro, A. J.; Egelhoff, W. F., Jr.; Moffat, T.: Recrystallization texture, epitaxy, and magnetic properties of electrodeposited FePt on Cu(001). *Appl. Phys. Lett.* **2004**, *85*, 1353-1355.

17. Lay, M. D.; Stickney, J. L.: Electrodeposition of Au-Cd alloy nanostructures on Au(111). *J. Am. Chem. Soc.* **2003**, *125*, 1352-1355.

18. Switzer, J. A.; Liu, R.; Bohannan, E. W.; Ernst, F.: Epitaxial electrodeposition of a crystalline metal oxide onto single-crystalline silicon. *J. Phys. Chem. B* **2002**, *106*, 12369-12372.

19. Switzer, J. A.; Shumsky, M. G.; Bohannan, E. W.: Electrodeposited ceramic single crystals. *Science (Washington, D. C.)* **1999**, *284*, 293-296.

20. Mahenderkar, N. K.; Liu, Y.-C.; Koza, J. A.; Switzer, J. A.: Electrodeposited germanium nanowires. *ACS Nano* **2014**, *8*, 9524-9530.

21. Switzer, J. A.; Kothari, H. M.; Poizot, P.; Nakanishi, S.; Bohannan, E. W.: Enantiospecific electrodeposition of a chiral catalyst. *Nature (London, U. K.)* **2003**, *425*, 490-493.

22. Guendel, A.; Devolder, T.; Chappert, C.; Schmidt, J. E.; Cortes, R.; Allongue, P.: Electrodeposition of Fe/Au(111) ultrathin layers with perpendicular magnetic anisotropy. *Physica B (Amsterdam, Neth.)* **2004**, *354*, 282-285.

23. Goux, A.; Pauporte, T.; Yoshida, T.; Lincot, D.: Mechanistic study of the electrodeposition of nanoporous self-assembled ZnO/Eosin Y hybrid thin films: Effect of Eosin concentration. *Langmuir* **2006**, *22*, 10545-10553.

24. Kulp, E. A.; Switzer, J. A.: Electrochemical biomineralization: The deposition of calcite with chiral morphologies. *J. Am. Chem. Soc.* **2007**, *129*, 15120-15121.

25. Zhou, Y.; Switzer, J. A.: Electrochemical deposition and microstructure of copper (I) oxide films. *Scr. Mater.* **1998**, *38*, 1731-1738.

26. Poizot, P.; Hung, C.-J.; Nikiforov, M. P.; Bohannan, E. W.; Switzer, J. A.: An electrochemical method for CuO thin film deposition from aqueous solution. *Electrochem. Solid-State Lett.* **2003**, *6*, C21-C25.

27. Liu, R.; Vertegel, A. A.; Bohannan, E. W.; Sorenson, T. A.; Switzer, J. A.: Epitaxial electrodeposition of zinc oxide nanopillars on single-crystal gold. *Chem. Mater.* **2001**, *13*, 508-512.

28. Limmer, S. J.; Kulp, E. A.; Switzer, J. A.: Epitaxial electrodeposition of ZnO on Au(111) from alkaline solution: Exploiting amphoterism in Zn(II). *Langmuir* **2006**, *22*, 10535-10539.

29. Switzer, J. A.: Electrochemical architecture of ceramic nanocomposites. *Nanostruct. Mater.* **1992**, *1*, 43-46.

30. Switzer, J. A.; Kothari, H. M.; Bohannan, E. W.: Thermodynamic to kinetic transition in epitaxial electrodeposition. *J. Phys. Chem. B* **2002**, *106*, 4027-4031.

31. Liu, R.; Bohannan, E. W.; Switzer, J. A.; Oba, F.; Ernst, F.: Epitaxial electrodeposition of Cu_2O films onto InP(001). *Appl. Phys. Lett.* **2003**, *83*, 1944-1946.

32. Zhou, Y.; Switzer, J.: Effect of bath temperature on the phase compn. and microstructure of galvanostatic electrodeposited cuprous oxide films. *Cailiao Yanjiu Xuebao* **1996**, *10*, 512-516.

33. Liu, R.; Oba, F.; Bohannan, E. W.; Ernst, F.; Switzer, J. A.: Shape control in epitaxial electrodeposition: Cu_2O nanocubes on InP(001). *Chem. Mater.* **2003**, *15*, 4882-4885.

34. Switzer, J. A.: Atomic layer electrodeposition. *Science (Washington, DC, U. S.)* **2012**, *338*, 1300-1301.

35. Switzer, J. A.; Hodes, G.: Electrodeposition and chemical bath deposition of functional nanomaterials. *MRS Bull.* **2010**, *35*, 743-750.

36. Switzer, J. A.: Electrodeposition of superlattices and multilayers. *Electrochem. Nanomater.* **2001**, 67-101.

37. Switzer, J. A.; Shane, M. J.; Phillips, R. J.: Electrodeposited ceramic superlattices. *Science (Washington, D. C., 1883-)* **1990**, *247*, 444-446.

38. Allongue, P.; Henry de Villeneuve, C.; Morin, S.; Boukherroub, R.; Wayner, D. D. M.: The preparation of flat H-Si(111) surfaces in 40% NH_4F revisited. *Electrochim. Acta* **2000**, *45*, 4591-4598.

39. Munford, M. L.; Cortes, R.; Allongue, P.: The preparation of ideally ordered flat H-Si(111) surfaces. *Sens. Mater.* **2001**, *13*, 259-269.

40. Sze, S. M. *Physics of Semiconductor Devices*; 2nd ed.; John Wiley & Sons, Inc.: New York, 1981.

41. Takano, N.; Niwa, D.; Yamada, T.; Osaka, T.: Nickel deposition behavior on n-type silicon wafer for fabrication of minute nickel dots. *Electrochim. Acta* **2000**, *45*, 3263-3268.

42. Switzer, J. A.; Hill, J. C.; Mahenderkar, N. K.; Liu, Y.-C.: Nanometer-thick gold on silicon as a proxy for single-crystal gold for the electrodeposition of epitaxial cuprous oxide thin films. *ACS Appl. Mater. Interfaces* **2016**, *8*, 15828-15837.

43. Coyle, R. T.; Switzer, J. A.; "Electrochemical synthesis of ceramic films and powders," U.S. Patent 4,882,014, issued November 21, 1989.

44. Switzer, J. A.: Electrodeposition of nanoscale architectures. *Handb. Nanophase Mater.* **1997**, 63-81.

45. Koza, J. A.; Hull, C. M.; Liu, Y.-C.; Switzer, J. A.: Deposition of β-$Co(OH)_2$ films by electrochemical reduction of tris(ethylenediamine)cobalt(III) in alkaline solution. *Chem. Mater.* **2013**, *25*, 1922-1926.

46. Koza, J. A.; He, Z.; Miller, A. S.; Switzer, J. A.: Electrodeposition of crystalline Co_3O_4-A catalyst for the oxygen evolution reaction. *Chem. Mater.* **2012**, *24*, 3567-3573.

47. Switzer, J. A.: Electrochemical synthesis of ceramic films and powders. *Am. Ceram. Soc. Bull.* **1987**, *66*, 1521-1524.

48. Lagowski, J. J. S., C. H. *Introduction to Semimicro Qualitative Analysis*; 8th ed.; Pearson Prentice Hall: Upper Saddle River, NJ, 2005.

49. Mu, G.; Gudavarthy, R. V.; Kulp, E. A.; Switzer, J. A.: Tilted epitaxial ZnO nanospears on Si(001) by chemical bath deposition. *Chem. Mater.* **2009**, *21*, 3960-3964.

50. Bard, A. J.; Faulkner, L. R. *Electrochemical Methods: Fundamentals and Applications*; 2nd ed.; Wiley: New York, 2000.

51. Sayed, S. Y.; Wang, F.; Malac, M.; Meldrum, A.; Egerton, R. F.; Buriak, J. M.: Heteroepitaxial growth of gold nanostructures on silicon by galvanic displacement. *ACS Nano* **2009**, *3*, 2809-2817.

52. Cho, A. Y.; Arthur, J. R.: Molecular beam epitaxy. *Prog. Solid State Chem.* **1975**, *10, Pt. 3*, 157-191.

53. Nakanishi, S.; Lu, G.; Kothari, H. M.; Bohannan, E. W.; Switzer, J. A.: Epitaxial electrodeposition of prussian blue thin films on single-crystal Au(110). *J. Am. Chem. Soc.* **2003**, *125*, 14998-14999.

54. Liu, R.; Kulp, E. A.; Oba, F.; Bohannan, E. W.; Ernst, F.; Switzer, J. A.: Epitaxial electrodeposition of high-aspect-ratio Cu_2O(110) nanostructures on InP(111). *Chem. Mater.* **2005**, *17*, 725-729.

55. Breyfogle, B. E.; Hung, C.-J.; Shumsky, M. G.; Switzer, J. A.: Electrodeposition of silver(II) oxide films. *J. Electrochem. Soc.* **1996**, *143*, 2741-2746.

56. Sorenson, T. A.; Morton, S. A.; Waddill, G. D.; Switzer, J. A.: Epitaxial electrodeposition of Fe_3O_4 thin films on the low-index planes of gold. *J. Am. Chem. Soc.* **2002**, *124*, 7604-7609.

57. Kothari, H. M.; Kulp, E. A.; Limmer, S. J.; Poizot, P.; Bohannan, E. W.; Switzer, J. A.: Electrochemical deposition and characterization of Fe_3O_4 films produced by the reduction of Fe(III)-triethanolamine. *J. Mater. Res.* **2006**, *21*, 293-301.

58. Kulp, E. A.; Kothari, H. M.; Limmer, S. J.; Yang, J.; Gudavarthy, R. V.; Bohannan, E. W.; Switzer, J. A.: Electrodeposition of epitaxial magnetite films and ferrihydrite nanoribbons on single-crystal gold. *Chem. Mater.* **2009**, *21*, 5022-5031.

59. Bohannan, E. W.; Jaynes, C. C.; Shumsky, M. G.; Barton, J. K.; Switzer, J. A.: Low-temperature electrodeposition of the high-temperature cubic polymorph of bismuth(III) oxide. *Solid State Ionics* **2000**, *131*, 97-107.

60. Vertegel, A. A.; Bohannan, E. W.; Shumsky, M. G.; Switzer, J. A.: Epitaxial electrodeposition of orthorhombic α-PbO_2 on (100)-oriented single crystal Au. *J. Electrochem. Soc.* **2001**, *148*, C253-C256.

61. Switzer, J. A.: The n-silicon/thallium(III) oxide heterojunction photoelectrochemical solar cell. *J. Electrochem. Soc.* **1986**, *133*, 722-728.

62. Boonsalee, S.; Gudavarthy, R. V.; Bohannan, E. W.; Switzer, J. A.: Epitaxial electrodeposition of Tin(II) sulfide nanodisks on single-crystal Au(100). *Chem. Mater.* **2008**, *20*, 5737-5742.

63. Vertegel, A. A.; Shumsky, M. G.; Switzer, J. A.: Epitaxial electrodeposition of lead sulfide on (100)-oriented single-crystal gold. *Angew. Chem., Int. Ed.* **1999**, *38*, 3169-3171.

64. Choi, K.-S.: Shape control of inorganic materials via electrodeposition. *Dalton Trans.* **2008**, 5432-5438.

65. Ager, J. W.; Shaner, M. R.; Walczak, K. A.; Sharp, I. D.; Ardo, S.: Experimental demonstrations of spontaneous, solar-driven photoelectrochemical water splitting. *Energy Environ. Sci.* **2015**, *8*, 2811-2824.

66. Walter, M. G.; Warren, E. L.; McKone, J. R.; Boettcher, S. W.; Mi, Q.; Santori, E. A.; Lewis, N. S.: Solar water splitting cells. *Chem. Rev. (Washington, DC, U. S.)* **2010**, *110*, 6446-6473.

67. Pugh, J. R.; Mao, D.; Zhang, J. G.; Heben, M. J.; Nelson, A. J.; Frank, A. J.: A metal:p-n-cadmium telluride Schottky-barrier solar cell: photoelectrochemical generation of a shallow p-type region in n-CdTe. *J. Appl. Phys.* **1993**, *74*, 2619-2625.

68. Lewis, N. S.: Chemical control of charge transfer and recombination at semiconductor photoelectrode surfaces. *Inorg. Chem.* **2005**, *44*, 6900-6911.

69. Hamann, T. W.; Gstrein, F.; Brunschwig, B. S.; Lewis, N. S.: Measurement of the driving force dependence of interfacial charge-transfer rate constants in response to pH changes at n-ZnO/H_2O interfaces. *Chem. Phys.* **2006**, *326*, 15-23.

70. Gerischer, H.: The role of semiconductor structure and surface properties in photoelectrochemical processes. *J. Electroanal. Chem. Interfacial Electrochem.* **1983**, *150*, 553-569.

71. Hilal, H. S.; Turner, J. A.: Controlling charge-transfer processes at semiconductor/liquid junctions. *Electrochim. Acta* **2006**, *51*, 6487-6497.

72. Hu, Y.-S.; Kleiman-Shwarsctein, A.; Stucky, G. D.; McFarland, E. W.: Improved photoelectrochemical performance of Ti-doped α-Fe_2O_3 thin films by surface modification with fluoride. *Chem. Commun. (Cambridge, U. K.)* **2009**, 2652-2654.

73. Turner, J. A.; Parkinson, B. A.: The application of chronocoulometry to the study of adsorption at the semiconductor/electrolyte interface. *J. Electroanal. Chem. Interfacial Electrochem.* **1983**, *150*, 611-617.

74. Lyon, L. A.; Hupp, J. T.: Energetics of semiconductor electrode/solution interfaces: EQCM evidence for charge-compensating cation adsorption and intercalation during accumulation layer formation in the titanium dioxide/acetonitrile system. *J. Phys. Chem.* **1995**, *99*, 15718-15720.

75. Wang, C. M.; Mallouk, T. E.: Wide-range tuning of the titanium dioxide flat-band potential by adsorption of fluoride and hydrofluoric acid. *J. Phys. Chem.* **1990**, *94*, 4276-4280.

76. McCrory, C. C. L.; Jung, S.; Ferrer, I. M.; Chatman, S. M.; Peters, J. C.; Jaramillo, T. F.: Benchmarking hydrogen evolving reaction and oxygen evolving reaction electrocatalysts for solar water splitting devices. *J. Am. Chem. Soc.* **2015**, *137*, 4347-4357.

77. McCrory, C. C. L.; Jung, S.; Peters, J. C.; Jaramillo, T. F.: Benchmarking heterogeneous electrocatalysts for the oygen evolution reaction. *J. Am. Chem. Soc.* **2013**, *135*, 16977-16987.

78. Weber, M. F.; Dignam, M. J.: Efficiency of splitting water with semiconducting photoelectrodes. *J. Electrochem. Soc.* **1984**, *131*, 1258-1265.

79. Gorlin, Y.; Jaramillo, T. F.: A Bifunctional nonprecious metal catalyst for oxygen reduction and water oxidation. *J. Am. Chem. Soc.* **2010**, *132*, 13612-13614.

80. Weber, M. F.; Dignam, M. J.: Splitting water with semiconducting photoelectrodes−efficiency considerations. *Int. J. Hydrogen Energy* **1986**, *11*, 225-232.

81. Tsuji, E.; Imanishi, A.; Fukui, K.-i.; Nakato, Y.: Electrocatalytic activity of amorphous RuO_2 electrode for oxygen evolution in an aqueous solution. *Electrochimica Acta* **2011**, *56*, 2009-2016.

82. Swesi, A. T.; Masud, J.; Nath, M.: Nickel selenide as a high-efficiency catalyst for oxygen evolution reaction. *Energy Environ. Sci.* **2016**, *9*, 1771-1782.

83. Doyle, R. L.; Godwin, I. J.; Brandon, M. P.; Lyons, M. E. G.: Redox and electrochemical water splitting catalytic properties of hydrated metal oxide modified electrodes. *Phys. Chem. Chem. Phys.* **2013**, *15*, 13737-13783.

84. Hoare, J. P. *The Electrochemistry of Oxygen*; Interscience: New York, 1968.

85. Damjanovic, A.; Dey, A.; Bockris, J. O. M.: Kinetics of oxygen evolution and dissolution on platinum electrodes. *Electrochim. Acta* **1966**, *11*, 791-814.

86. Damjanovic, A.; Genshaw, M. A.; Bockris, J. O. M.: Hydrogen peroxide in oxygen reduction at platinum in sulfuric acid solution. *J. Electrochem. Soc.* **1967**, *114*, 466-472.

87. Subbaraman, R.; Tripkovic, D.; Chang, K.-C.; Strmcnik, D.; Paulikas, A. P.; Hirunsit, P.; Chan, M.; Greeley, J.; Stamenkovic, V.; Markovic, N. M.: Trends in activity for the water electrolyzer reactions on 3d M(Ni,Co,Fe,Mn) hydro(oxy)oxide catalysts. *Nat. Mater.* **2012**, *11*, 550-557.

88. Garcia-Mota, M.; Bajdich, M.; Viswanathan, V.; Vojvodic, A.; Bell, A. T.; Noerskov, J. K.: Importance of correlation in determining electrocatalytic oxygen evolution activity on cobalt oxides. *J. Phys. Chem. C* **2012**, *116*, 21077-21082.

89. Hamelin, A.: Lead adsorption on gold single crystal stepped surfaces. *J. Electroanal. Chem. Interfacial Electrochem.* **1979**, *101*, 285-290.

90. Hamelin, A.; Lipkowski, J.: Underpotential deposition of lead on gold single crystal faces. Part II. General discussion. *J. Electroanal. Chem. Interfacial Electrochem.* **1984**, *171*, 317-330.

91. Hamelin, A.: Underpotential deposition of lead on single crystal faces of gold. Part I. The influence of crystallographic orientation of the substrate. *J. Electroanal. Chem. Interfacial Electrochem.* **1984**, *165*, 167-180.

92. Marsh, D. A.; Yan, W.; Liu, Y.; Hemminger, J. C.; Penner, R. M.; Borovik, A. S.: Water oxidation using a cobalt monolayer prepared by underpotential deposition. *Langmuir* **2013**, *29*, 14728-14732.

93. Trasatti, S.; Petrii, O. A.: Real surface area measurements in electrochemistry. *Pure Appl. Chem.* **1991**, *63*, 711-734.

94. Boggio, R.; Carugati, A.; Trasatti, S.: Electrochemical surface properties of cobalt oxide (Co_3O_4) electrodes. *J. Appl. Electrochem.* **1987**, *17*, 828-840.

95. Minguzzi, A.; Fan, F.-R. F.; Vertova, A.; Rondinini, S.; Bard, A. J.: Dynamic potential-pH diagrams application to electrocatalysts for water oxidation. *Chem. Sci.* **2012**, *3*, 217-229.

96. Liu, Y.-C.; Koza, J. A.; Switzer, J. A.: Conversion of electrodeposited $Co(OH)_2$ to CoOOH and Co_3O_4, and comparison of their catalytic activity for the oxygen evolution reaction. *Electrochim. Acta* **2014**, *140*, 359-365.

97. Kiessig, H.: Interference of Röntgen rays on thin layers. *Ann. Physik [5]* **1931**, *10*, 769-788.

98. Phung, T. M.; Johnson, D. C.; Antonelli, G. A.: A detailed experimental and analytical study of the thermal expansion of dielectric thin films on Si by x-ray reflectivity. *J. Appl. Phys.* **2006**, *100*, 064317/064311-064317/064316.

99. Kulp, E. A.; Limmer, S. J.; Bohannan, E. W.; Switzer, J. A.: Electrodeposition of nanometer-thick ceria films by oxidation of cerium(III)-acetate. *Solid State Ionics* **2007**, *178*, 749-757.

100. Nakajima, K.; Aoki, S.; Sudo, S.; Mondo, M.; Kudo, H.; Fujiwara, S.; Arai, T.: Correlation between x-ray reflectivity and Rutherford backscattering spectroscopy for density measurement of thin films. *Jpn. J. Appl. Phys., Part 1* **1993**, *32*, 164-165.

VITA

Ying-Chau (Allen) Liu was born on July 18, 1985, in Taipei, Republic of China (Taiwan), to Debbie and Joseph Liu. He finished high school in Taiwan with a biology emphasis in June 2003. He then went to college at Indiana State University where he obtained his B.S. in Chemistry in May 2008. During his undergraduate studies, he worked as a computer lab supervisor, as well as a general chemistry lab teaching assistant and a math tutor. He also conducted physical chemistry research under Prof. Arthur M. Halpern and organic synthesis research under Prof. Richard W. Fitch. He continued his education towards graduate degrees at Missouri University of Science and Technology where he obtained a M.S. in Chemical Engineering in May 2010 and a Ph.D. in Chemistry in December 2016. Under the guidance of his Ph.D. advisor, Prof. Jay A. Switzer, Allen Liu conducted exciting research in the field of electrochemistry and solar energy conversion and storage. In summer 2014, he worked as a research associate intern at Brewer Science Inc. in Rolla, MO. He also attended the Gordon Research Conference: Electrodeposition, in Biddeford, ME, and presented his research findings. His publications during his Ph.D. career include:

1. Switzer, J.A., Hill, J.C., Mahenderkar, N.K., and **Liu, Y.-C.** Nanometer-thick gold on silicon as a proxy for single-crystal gold for the electrodeposition of epitaxial cuprous oxide thin films. *ACS Appl. Mater. Interfaces* **2016**, *8*, 15828-15837.

2. **Liu, Y.-C.**, Koza, J.A., and Switzer, J.A. Conversion of electrodeposited $Co(OH)_2$ to CoOOH and Co_3O_4, and comparison of their catalytic activity for the oxygen evolution reaction. *Electrochim. Acta* **2014**, *140*, 359–365.

3. Mahenderkar, N.K., **Liu, Y.-C.**, Koza, J.A., and Switzer, J.A. Electrodeposited germanium nanowires. *ACS Nano* **2014**, *8*(9), 9524–9530.

4. Koza, J.A., Hull, C.M., **Liu, Y.-C.**, and Switzer, J.A. Deposition of β-$Co(OH)_2$ films by electrochemical reduction of tris(ethylenediamine)cobalt(III) in alkaline solution. *Chem. Mater.* **2013**, *25*, 1922–1926.